Delft University of Technology

Parameter Identification, Simulation, Linearization and Validation of a Ship Propulsion System

by

Yueming Sang

A thesis submitted in partial fulfillment for the
degree of Master of Science

in the

Faculty of Mechanical, Maritime and Materials Engineering (3mE)
Maritime and Transport Technology

May 2018

Declaration of Authorship

I, YUEMING SANG, declare that this thesis titled, 'Parameter Identification, Simulation, Linearization and Validation of a Ship Propulsion System' and the work presented in it are my own. I confirm that:

- This work was done wholly or mainly while in candidature for a research degree at this University.
- Where any part of this thesis has previously been submitted for a degree or any other qualification at this University or any other institution, this has been clearly stated.
- Where I have consulted the published work of others, this is always clearly attributed.
- Where I have quoted from the work of others, the source is always given. With the exception of such quotations, this thesis is entirely my own work.
- I have acknowledged all main sources of help.
- Where the thesis is based on work done by myself jointly with others, I have made clear exactly what was done by others and what I have contributed myself.

Signed: _____

Date: _____

"A journey of one thousand miles begins with a single step."

Lao-Tzu

Delft University of Technology

Abstract

Faculty of Mechanical, Maritime and Materials Engineering (3mE)
Maritime and Transport Technology

Master of Science

by Yueming Sang

This Thesis is written to obtain the Master of Science degree of Maritime Technology at Delft University of Technology. It describes a research regarding with the calibration(parameter identification), validation and linearization of a ship propulsion system model. In the meantime, the Thesis is also one sub-project under the research program "Potential of Hardware-In-the-Loop Simulation in the Towing Tank" held by Dr.Ir.A.Vrijdag.

HIL (Hardware-In-the-Loop) Simulation is widely used in Engineering Technology Field, and has been proved to be a very effective, highly-efficient, economical and environmental friendly strategy in the test and development of engineering control systems. The model scale ship tests nowadays, on the other hand, need to be improved and HIL Simulation provides an innovative & creative way, therefore it is reasonable to start the program and explore more in this field.

Acknowledgements

I would like to thank Mr.A.Vrijdag for his role as my mentor during the whole research project. Furthermore I would like to thank my Italian friends, Michele Martelli, Vittorio Garofano and Giacomo Penco for their support during the toughest times of my Thesis work. Besides, I would like to thank Xiaozhe Wang, Shimeng Zhao, Xiaoming Ma and Ziyuan Zeng, who supported me during my two-year MSc academic career. Last but not least, I would like to give special thanks to my dear parents for their moral and financial support, which made my study become possible.

February, 2018

Yueming Sang

Contents

List of Figures

List of Tables

Symbols

D	propeller diameter	m
F	force	N
i_a	armature current	A
i_{gb}	gearbox reduction ratio	[-]
I_p	moment of inertia	$kg \cdot m^2$
J	advanced ratio	[-]
K_T	thrust coefficient	[-]
K_Q	torque coefficient	[-]
K_b	back EMF coefficient	$V/rad/s$
K_m	motor torque constant	$N \cdot m/A$
L	electric inductance	H
m	mass	kg
M_f	friction torque	$N \cdot m$
M_L	load torque	$N \cdot m$
n	rotation speed	rps
Q	propeller open-water torque	$N \cdot m$
R	electric resistance	Ω
T	thrust force	N
t	time	s
t	thrust deduction	[-]
v_a	armature voltage	V
v_s	ship speed	m/s
w	wake factor	[-]
ρ	density	kg/m^3
ω	angular frequency	rad/s

To my family, especially my dear grandfather.

Background Information

HIL Simulation has been applied in many industry fields for decades, for instance it is already the standard approach for development, customization and production tests of ECU [4]. Nowadays, for the need of design, implementation and testing of more complicated control systems, HIL Simulation is increasingly being required [5].

The following example will give a clear explanation about how HIL Simulation works: an industrial company designed and built a feedback control system (which is used to control the rising speed, direction and monitor the workload) for the operation work of a crane, but before it could be put into use in reality, the capability of this control system needs to be tested. The most straightforward way to do the test, with no doubt, is connecting the feedback control system with a real crane and creating a closed-loop-control system. The result of this test will be convincing since it represents the reality with 100%. However, such a testing way could be expensive, time-consuming and even dangerous. To eliminate these negative factors without damaging the quality of testing result, instead of using a real crane, a simulation model which is able to accurately mimic the dynamic behavior of the crane could be involved (as shown in Fig 1).

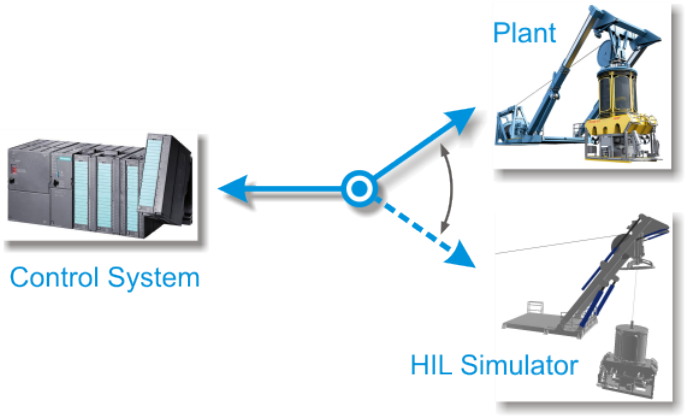

FIGURE 1: Example of HIL Simulation System

This way of testing will be economical, highly-efficient and safer compared to the former one. Here, if the feedback control system is named as controller, the real crane as plant

and the simulation model of crane as simulator, this typical example could be extended to describe the characteristics (as well as the main components) of HIL Simulation. Therefore, the definition is given as follows:

Hardware-In-the-Loop Simulation is a type of real-time simulation which contains hardware components in a closed-loop control system. It could be used in the development and test of the controller since this type of simulation shows how the controller responds, in real time, to realistic virtual stimuli. On the other hand, it could also be used to determine whether the simulator (simulation model of the plant) is valid or not.

With all the advantages mentioned above, maritime industries has also embraced HIL techniques, especially in naval projects. The development and testing of the propulsion control system of the Dutch M-class frigates could be given as an early example while the testing for Italian Navy gives other examples [6] [7].

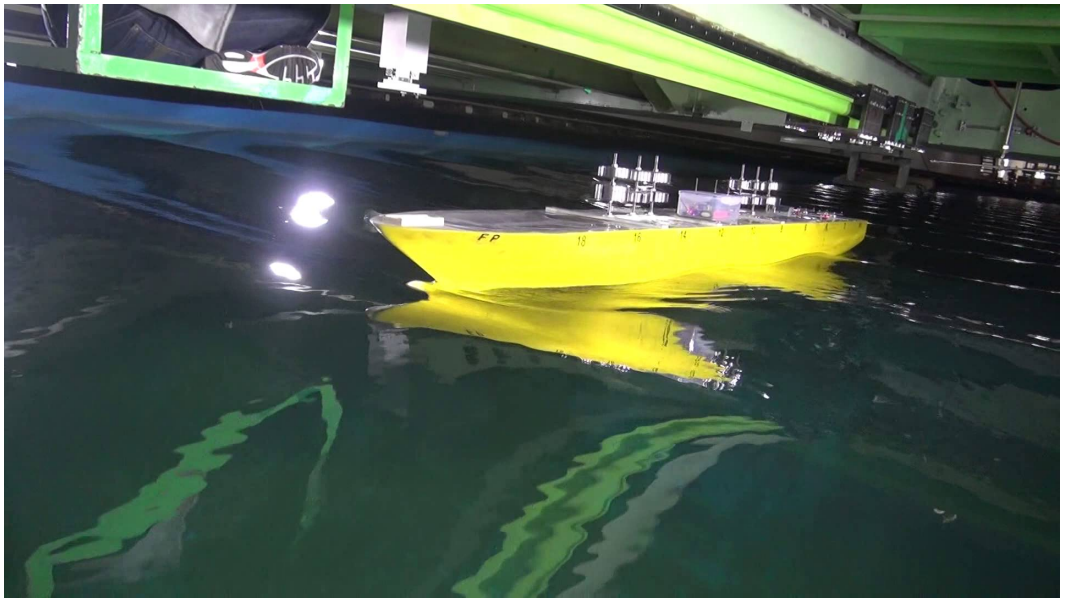

FIGURE 2: A ship model during the free sailing test

Introducing HIL techniques into model-scale ship test, however, is a novel application and the main reason to do so is: modify the traditional way of doing model-scale test (e.g. free sailing test shown in Fig 2) so as to acquire a more complete and realistic result. Currently, model-scale ship tests still fail to take the dynamics of involved shipboard systems into account. For example, when the model-scale free sailing tests in waves are carried out, the testing condition of propulsion system (including electric motor, shaft and propeller) of the ship model will either be under constant propeller speed, constant shaft torque or under constant motor power. Since in waves all the three are actually variables whose dynamic behavior is governed by the drive train characteristics, it is obvious that neither of these options reflects the realistic behavior of propulsion system. Therefore, a natural question can be arisen: *to what extent, and in which cases, the*

dynamics of shipboard systems affect the behavior of overall system [1]. By exploring the application of HIL Simulation in towing tank, the research program Potential of Hardware-In-the-Loop Simulation in the Towing Tank will provide a mean to answer this question.

The ambition is to develop an instrumented model scale ship of which the components of the drive train and its control are included by means of a correctly scaled time domain computer simulation model of the propulsion system [1]. In other words, a new type of experimental setup which integrates model scale ship tests with real-time dynamic simulation of the shipboard systems including their controls will be created.

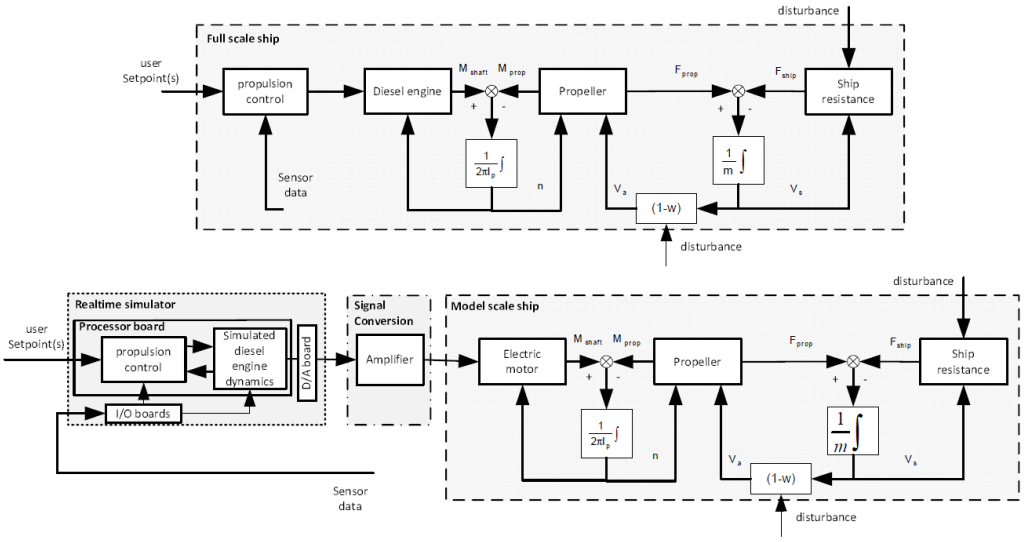

FIGURE 3: Schematic visualization of full scale and model scale system [1]

The schematic visualization of the whole system is shown in Fig 3, from the bottom figure it could be acknowledged that the simulation model will be running on a real-time processor which, via I/O boards, provides electric power to an electric motor of the instrumented model scale ship, then the motor will drive in turn the shaft and propeller. The drive train partially consists of the hardware (amplifier, motor, shaft as well as propeller) and partially consists of the real-time simulation model of the prime mover (for instance a Diesel Engine or an electric motor). If this new integrated test setup could become reality, the traditionally separate disciplines of ship hydromechanics, marine engineering and controls could be considered simultaneously including interactions with each other and with the dynamic environment [1]. Furthermore, the new setup is also able to quantify the expected behavior of the full-scale system thus the safety, environmental friendliness and the workability of ship will be increased as well.

To develop this setup, there are two main challenges that need to be overcome. First one is the hydrodynamic scale effect due to the model scale of the hull and propeller

compared with full scale. Although scaling laws have been made and developed by many scientists during the past centuries, to what extent these detrimental scale effects could influence our foreseen system and how to deal with it remains to be a question. The other challenge is to ensure equivalent propulsion plant dynamics on model scale compared to full scale [1], in other words, is to ensure the dynamic behavior of the drive train reflects reality.

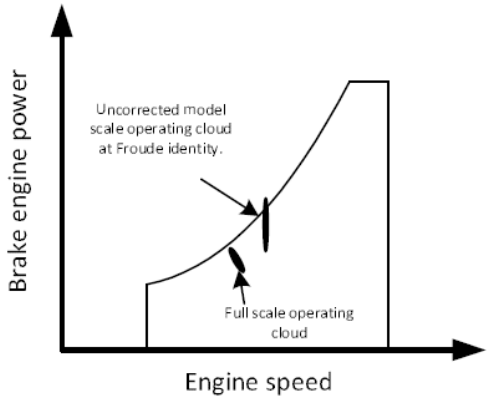

FIGURE 4: Visualization of effect of unrepresentative model scale dynamics on the operating cloud [1]

The example given in [1] visualizes the importance: as shown in Fig 4, unrepresentative dynamics of the model scale setup results in a totally different operating cloud (shape & orientation) compared with full scale, which in this particular case would lead to activating the protective features of the engine control system too often, again leading to erroneous impression of system behavior in waves or during maneuvers.

All in all, to build this test-setup, researches should focus on three domains: the full-scale domain, the model-scale domain and the scaling laws between full-scale & model-scale. **As a sub-project, this Thesis deals with the model-scale domain research.**

In the model-scale domain, effort should be made on exploring the hydromechanical characteristics of model hull, the thrust characteristics of propulsor, the mechanical characteristics of the drivetrain and the electrical characteristics of the prime-mover (in this particular case the prime-mover is an electric motor).

Although many researches regarding model-scale ships have been elaborated in the literature, most of them focus on investigating maneuvering behavior of the model ship. For instance, from the year 1998 to 2016, NTNU constructed two 1:70 model scale supply ships (Cybership I and Cybership II), works about determining maneuvering coefficients and the corresponding control techniques have been reported in several papers [8] [9] [10] [11] [12] [13] [14], yet only two of them ([9] and [10]) have mentioned the identification of propulsor thrust characteristics and none of them gave information about identification

of the characteristics of drivetrain or prime-mover (electric motor). Therefore, in this Thesis, a complete research about identifying the propulsion system's characteristics of a model-scale ship (Tito Neri) is elaborated.

Besides, as shown in Fig 3, propulsion control has been involved in the test-setup. Although modeling of the control system will not be presented in this Thesis, some discussions about linearization of the propulsion system will be given as a preparation of future work.

Chapter 1

Research Objectives

Based on the foregoing, there are two main topics in this Thesis. The first topic is identifying the characteristics (or parameter identification, to be specific) of a model-scale ship propulsion system and the second topic is linearizing the propulsion system. In this Chapter, the structure of this Thesis will be introduced, including the scope, research questions and the outline.

1.1 Scope

First of all, as shown in Fig 5, the Thesis only focuses on model-scale research therefore all the issues related to full-scale ship are out of boundary. Meanwhile, challenges regarding scale effects have not been explored in the graduation project as well.

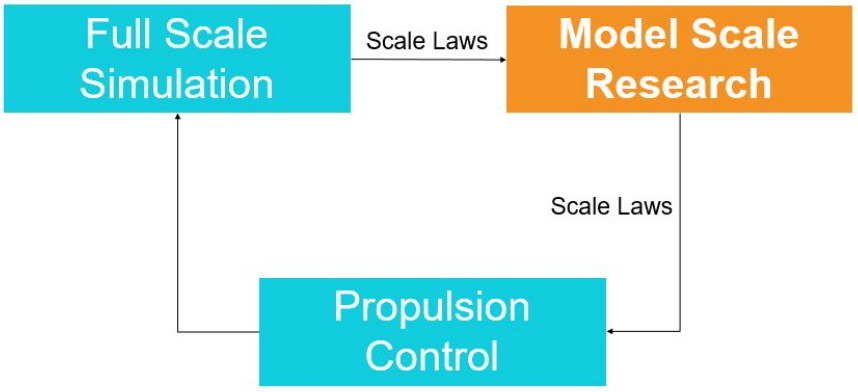

FIGURE 5: Scope of the graduation project

Additionally, although the ultimate goal of the research program Potential of Hardware-In-the-Loop Simulation in the Towing Tank is developing a test setup which could be used to predict the behavior of ship-board systems under free-sailing condition, works need to be done one step after another. In this Thesis, instead of free-sailing, the relatively simple operating conditions, including dry-run, bollard-pull and straight line sailing condition will be adapted to analyze the behavior of the propulsion system.

The model-scale ship which has been chosen as the research object of this Thesis is Tito Neri (shown in Fig 6). During the past few years, a fleet of this model boat with same instruments on board has been used for educational purposes in course MT218 Mechatronics for all MSc students of Maritime Technology in TU Delft. During the course, an online and a offline Dynamic Positioning Model are required to be built based on thrust allocation and PID control, while the characteristics of the propulsion chain, are again out of consideration, just like the researches that have been done by NTNU mentioned in last Chapter.

In order to identify the parameters of Tito Neri's propulsion system, some tests (or experiments) need to be designed, conducted and the values of those parameters could be determined through test result analysis. After the parameters are identified, corresponding simulation model of this propulsion system is able to be built and values of the identified parameters could be validated by means of result comparison between the simulation model and the test.

Besides the parameter identification, simulation and validation, this particular propulsion system will be linearized which aims at, as mentioned in the last Chapter, providing a basis of propulsion control that will be introduced in the future.

FIGURE 6: Picture of Model Boat "Tito Neri"

1.2 Research Questions

Based on the analysis of the aim of this graduation project, research questions are given as follows:

- **Which parameters of this propulsion system should be identified?**
- **How to determine the value of those parameters?**
- **After being determined, how to validate the values of those parameters?**
- **How to linearize this non-linear propulsion system?**

Basically, the Thesis is written to answer these four questions, and the outline is given in next section.

1.3 Outline

The Thesis is structured in 7 Chapters. Chapter 2 is used to give information about propulsion system of Tito Neri and based on the provided information, mathematical model to describe the behavior of the propulsion system could be built. During this procedure, the parameters which need to be identified will become clear and the method to identify them will also be presented in Chapter 2. Chapter 3, 4 & 5 deals with introducing and analyzing the tests which are required to identify those parameters together with the simulation and validation works. In Chapter 3 the effort made on acquiring parameters of DC motor and friction model is given, and Chapter 4 provides readers one way to identify the hull resistance curve. Some information related with propeller open-water diagram is shown and discussed in Chapter 5. After all the works mentioned above, it comes to linearization of the propulsion system, which will be discussed in Chapter 6. Chapter 7 ends the Thesis with summarized results, conclusions and further recommendations.

Chapter 2

The Mathematical Model of Tito Neri's Propulsion System & Related Discussions

In this Chapter the propulsion system of Tito Neri is looked through. In section 2.1, firstly some basic information, such as the components of the propulsion chain is given. And based on that, the mathematical model of this propulsion system could be built. Meanwhile, by examining the model, parameters that require to be identified in order to analyze the system behavior also become clear and are summarized in section 2.2. Therefore, in section 2.3 and 2.4, ways to determine the values of those required parameters are elaborated and discussed.

2.1 Derivation of the Mathematical Model

Before starting the derivation, basic information regarding with Tito Neris propulsion system (Fig 10 is the block diagram) should be given. This model boat has two shaft lines, and each shaft line consists of one ducted azimuth thruster, which is driven by a permanent magnet DC motor through a Z-shape driven train. Within the drive train, there are two horizontal shafts, one vertical shaft and two bevel gears (with a total gear ratio of 1/3).

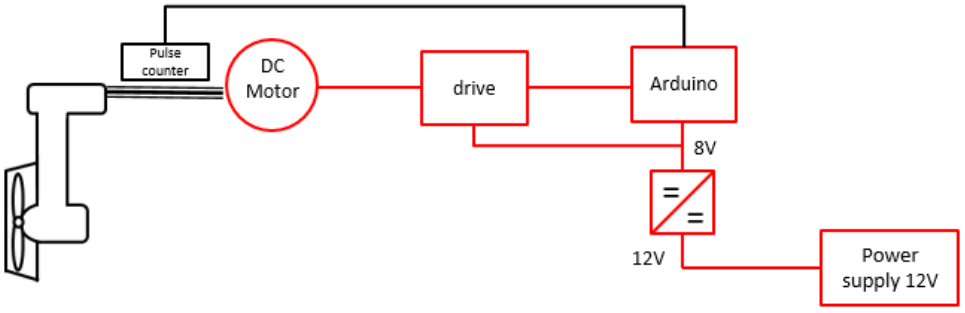

FIGURE 7: Block diagram of propulsion system of model boat Tito Neri

Since this model boat is used for course MT218 to test some DP models, in order to achieve a PI feedback control, one RPM sensor (which works as a pulse counter) is mounted on each horizontal shaft while the Arduino Board is responsible for counting the RPM voltage pulses and transferring the value to laptop, as shown in Fig 7. Additionally, the Arduino Board also generates PWM signals for motor controllers after communicating with the virtual control system in laptop.

In the foregoing it is acknowledged that the prime mover (among each shaft-line) of this propulsion system is a DC motor, therefore some fundamental characteristics and equations of a DC motor actuated system must be given before going into details.

Fig 8 shows the model of a permanent magnet DC motor: left part indicates the simplified electrical circuit and right part gives the mechanical model of the rotor. The dynamic behavior of the DC motor could be described by using the following two differential equations:

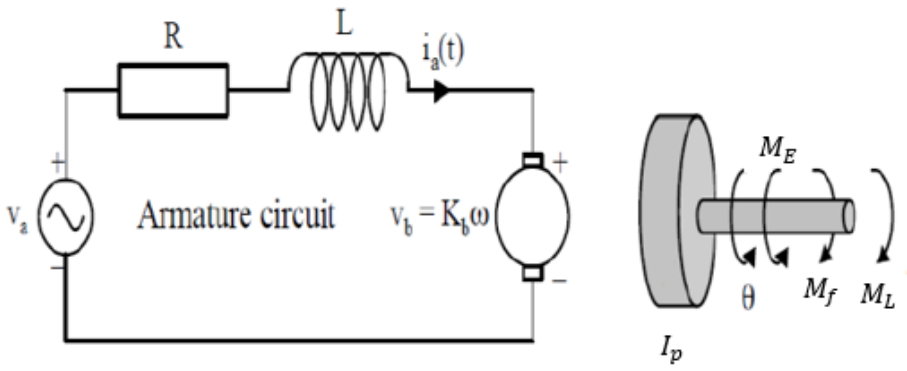

FIGURE 8: Model of a permanent magnet DC motor

The first equation describes the electrical behavior which follows Kirchhoff's voltage law:

$$L \cdot \frac{di_a}{dt} = v_a - R \cdot i_a - K_b \cdot \omega \tag{2.1}$$

The second equation describes the mechanical behavior which follows Newton's second law:

$$I_P \cdot \frac{d\omega}{dt} = K_m \cdot i_a - M_f - M_L \tag{2.2}$$

In Eq 2.1 and 2.2, v_a is the armature terminal voltage, i_a is the armature current and ω is the angular speed of rotor. R is armature resistance, L is armature inductance and I_P is moment of inertia. K_b is back EMF constant, which, after derivation, is equal to K_m [15][16], the motor torque constant. $M_E = K_m \cdot i_a$ stands for the torque provided by motor, M_f represents the friction torque and M_L is the load torque. $v_b = K_b \cdot \omega$ in Fig 8 shows the effect of back EMF voltage.

In the system shown above, v_a is the input signal, i_a and ω are always selected as state variables. The choice of output signal will depend on needs.

Apart from Eq 2.1 and Eq 2.2, the behavior of ship propulsion system is always interacted with ship hull hydrodynamics through propeller. For instance, under straight-line sailing condition when maneuvering is no longer under consideration, as the block diagram (in

which the dynamics of prime mover is excluded) shown in Fig 9, two loops are connected by the operation of propeller.

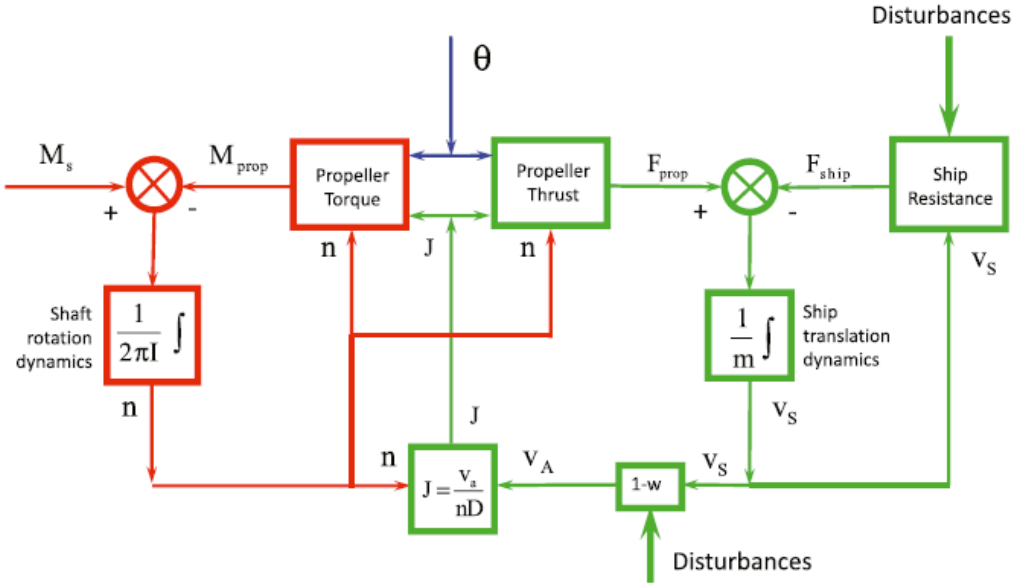

FIGURE 9: General Ship propulsion block diagram [2]

On the left side it shows the shaft rotation loop, whose behavior could be determined by Eq 2.3:

$$\boldsymbol{2\pi \cdot I_p \cdot \frac{dn}{dt} = M_S - M_{prop}} \tag{2.3}$$

In which I_p is the polar moment of inertia of the shaft, M_S stands for shaft torque, M_{prop} stands for propeller torque and n represents the rotating speed of shaft.

On the right side the ship translation loop is given, whose behavior could be determined by Eq 2.4:

$$\boldsymbol{m_{ship} \cdot \frac{dv_s}{dt} = F_{prop} - F_{ship}} \tag{2.4}$$

In which m_{ship} is the ship mass (included the added mass of water), F_{prop} stands for the thrust force provided by propeller, F_{ship} stands for ship resistance and v_s represents ship speed.

Apparently, if transmission efficiency η_{TRM} is taken into account, shaft torque M_S in Eq 2.3 could be transformed to brake torque M_b provided by the prime mover through $M_S = M_b \cdot \eta_{TRM}$. And after looking through the working principle of prime mover, expression of M_b could also be specified, as for DC motor, for instance, the brake torque

$M_b = K_m \cdot i_a$. Therefore, a combined version of Eq 2.2 and Eq 2.4 could be derived to describe the torque characteristics (or Shaft rotating dynamics) of the propulsion system.

Based on the analysis given above, the mathematical model of Tito Neri's propulsion system should contain three basic equations, which are going to describe the system behavior of electric circuit (Eq 2.1), ship speed dynamics (Eq 2.4) and shaft rotating dynamics individually. Until now, the former two equations are already clear enough to be adapted, yet the third one requires a detailed research about the propulsion chain, in which the effect of gearbox reduction ratio and friction torques must be involved, to be derived.

2.1.1 Components & Torque Analysis of Tito Neri's Propulsion Chain

To begin with, it is necessary to introduce the components of Tito Neris propulsion chain. As shown in Fig 10, the propulsion chain is consisted of 8 main components:

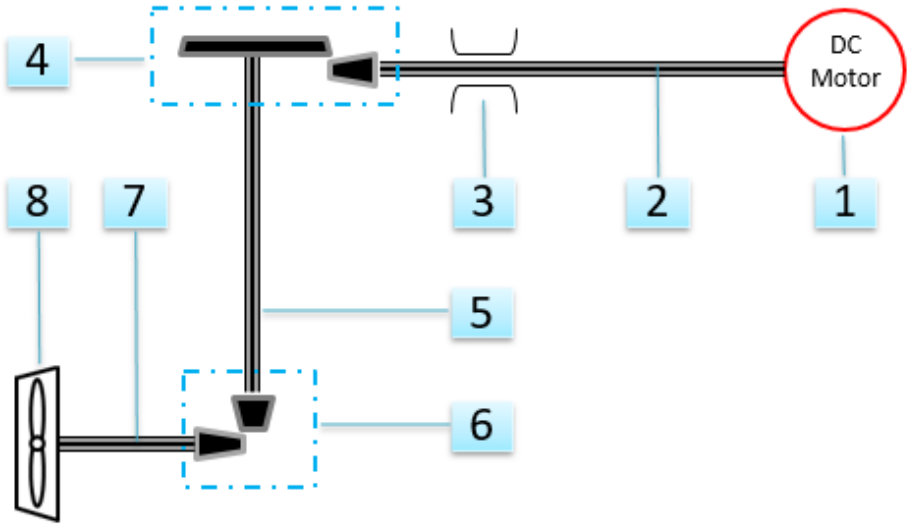

FIGURE 10: Propulsion Chain of Tito Neri

1. DC Motor
2. The first horizontal shaft which is connected to DC motor (also known as motor shaft), and its moment of inertia is I_{P1}
3. Shaft bearing
4. The first bevel gear, with a reduction ratio i_{gbt} equal to 3:1

5. The vertical shaft, whose moment of inertia (together with parts connected to the bevel gear)is I_{P2}

6. The second bevel gear with a reduction i_{gbb} equal to 1:1

7. The second horizontal shaft which is connected to propeller (also known as propeller shaft), and its moment of inertia is I_{P3} (keep notice that I_{P3} also includes the inertia of propeller)

8. The azimuth propeller equipped with nozzle

With the information given above, torque analysis along the propulsion chain could now be undertaken. Since there are two bevel gears, the whole chain needs to be broken down when doing torque analysis.

As shown in Fig 11, the whole chain is separated into 3 individual parts when bevel gears are separated. If defining the angular speed of component-1 (DC motor) and component-2 as ω_E, then according to the transmission law, the angular speed of component-5, 7 and 8 is $\frac{\omega_E}{i_{gbt}}$, which is also equal to the angular speed of propeller ω_p.

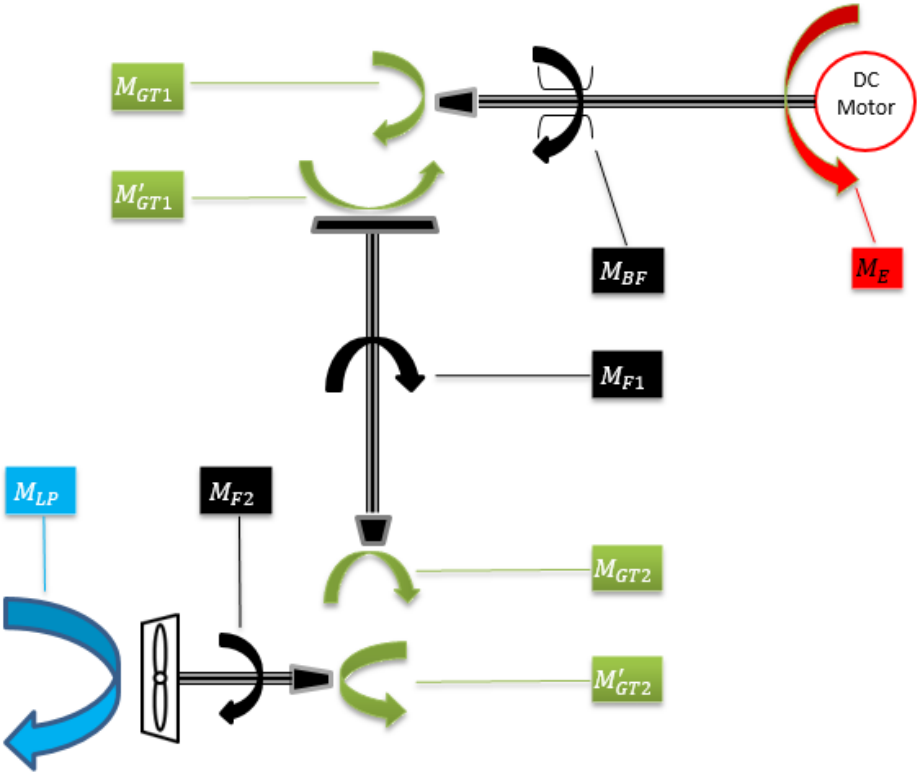

FIGURE 11: Torque Analysis of Propulsion Chain

Examine the first part (which contains DC motor, motor shaft and one gear), and if Eq 2.2 is applied, there is:

$$I_{P1} \cdot \frac{d\omega_E}{dt} = K_m \cdot i_a - M_{BF} - M_{GT1} \tag{2.5}$$

In which M_{BF} is the torque caused by friction between bearing and motor shaft (in future analysis it also contains the friction torque within the DC motor), M_{GT1} is the reacting torque from the driven gear.

Assuming there is no power loss within component-4 (actually the loss has been included by M_{F1}), the relation between M_{GT1} and M'_{GT1} is:

$$M'_{GT1} = i_{gbt} \cdot M_{GT1} \tag{2.6}$$

And examining the second part gives:

$$\frac{I_{P2}}{i_{gbt}} \cdot \frac{d\omega_E}{dt} = M'_{GT1} - M_{F1} - M_{GT2} \tag{2.7}$$

In which M_{F1} is the mixture of friction torques (which comes from component-4 and the friction between component-5 and its plastic cover), M_{GT2} is the reacting torque.

If the same assumption about power loss within bevel gear is made, there is:

$$M'_{GT2} = i_{gbb} \cdot M_{GT2} \tag{2.8}$$

By examining the third part, it gives:

$$\frac{I_{P3}}{i_{gbt} \cdot i_{gbb}} \cdot \frac{d\omega_E}{dt} = M'_{GT2} - M_{F2} - M_{LP} \tag{2.9}$$

In which M_{F2} is the mixed friction torque and M_{LP} is the propeller load torque.

After substituting step by step, from Eq 2.5 to Eq 2.9, the overall relation of torque (which determines the behavior of shaft rotation loop in the meantime) is:

$$(I_{P1} + \frac{I_{P2}}{i_{gbt}^2} + \frac{I_{P3}}{i_{gbt}^2 \cdot i_{gbb}^2}) \cdot \frac{d\omega_E}{dt} = K_m \cdot i_a - M_{BF} - \frac{M_{F1}}{i_{gbt}} - \frac{M_{F2}}{i_{gbt} \cdot i_{gbb}} - \frac{M_{LP}}{i_{gbt} \cdot i_{gbb}} \tag{2.10}$$

Eq 2.10 is the equation which describes torque characteristics of Tito Neri's propulsion system in every details.

2.1.2 Mathematical Model to describe Tito Neri's Propulsion System

After discussions given in section 2.1.1, the three basic equations of the mathematical model which describe the behavior of Tito Neris propulsion system are finally able to be determined.

As elaborated in last section, the first equation is used to describe the **electrical circuit of DC motor**. This equation is expressed as:

$$L \cdot \frac{di_a}{dt} = v_a - R \cdot i_a - K_b \cdot \omega_E \tag{2.11}$$

The second one is a transformation of Eq 2.10 in which propeller load torque M_{LP} is substituted by open-water torque Q, which represents the behavior of **shaft rotation loop**:

$$(I_{P1} + \frac{I_{P2}}{i_{gbt}^2} + \frac{I_{P3}}{i_{gbt}^2 \cdot i_{gbb}^2}) \cdot \frac{d\omega_E}{dt} = K_m \cdot i_a - M_{BF} - \frac{M_{F1}}{i_{gbt}} - \frac{M_{F2}}{i_{gbt} \cdot i_{gbb}} - \frac{Q}{i_{gbt} \cdot i_{gbb}} \tag{2.12}$$

To be specific, the open-water torque $Q = K_Q \cdot \rho \cdot D^5 \cdot (\frac{\omega_E}{i_{gbt} \cdot i_{gbb} 2\pi})^2$.

And the last one describes **ship translation loop**:

$$m_{ship} \cdot \frac{dv_s}{dt} = F_{prop} - F_{ship} \tag{2.13}$$

Now, the mathematical model of Tito Neri's propulsion system is completely built with Eq 2.11, Eq 2.12 and Eq 2.13.

2.2 Summary of Parameters that need to be identified

Obviously, before using the mathematical model to analyze the behavior of Tito Neri's propulsion system, some parameters must be identified. Below they are divided into 3 different types:

The first type is **DC motor related parameters**, including electric resistance R, electric inductance L and electromotive force constant K_b.

The second type is **mechanical parameters**, including friction torques M_{BF}, M_{F1}, M_{F2} and moment of inertia I_{P1}, I_{P2}, I_{P3}.

The last type is **hydrodynamic parameters**, including expression of the resistance curve $R = \alpha \cdot v_s^e$ and expressions of propeller open-water diagram $K_T = X(J), K_Q = Y(J)$.

2.3 Potential Ways to determine the value of DC motor related parameters & Mechanical parameters

In this section, potential ways to identify the DC motor related parameters & mechanical parameters mentioned in last section are discussed. This discussion also provides solid theoretical basis for the tests which will be elaborated and analyzed in coming chapters.

Parameter identification of DC motor is not a novel topic and quite a few literature could be found. The method given by their authors could be summarized as follows: firstly, a step voltage is added on the DC motor when the motor is isolated (which means the motor is running under no-load or free condition) and its responses, most often are the current and the rotating speed should be recorded. Then in most of the literature, such as [17], [18] and [19], the author adapted the Parameter Estimation tool in Simulink to determine the value of those parameters: the Simulink simulation model of DC motor should be built in which all the parameters need to be estimated were given their initial values, now by adding the same input voltage signal and after step by step of iterations, the Estimation toll is able to adjust the value of those parameters (within a given range) and make the running result of the simulation model be close to the recorded test data.

This method is proven to be a very convenient and highly-efficient way for parameter identification, if, the initial values have been wisely chosen (which means the initial values are already close to the final determined values of the parameter) or the adjusting range has been reasonably given (which means the operating range for adjusting the parameter value should not be infinite). However, the DC motor of Tito Neri is a grey-box and very limited information could be found. Therefore, the Parameter Estimation tool is not very applicable in this case and some other strategies should be adapted.

2.3.1 Identification of R, K_b and M_{BF}

As mentioned above, the DC motor should be isolated when input voltage is given. As for Tito Neri, although isolating DC motor completely from the propulsion chain is impossible due to the chosen construction, a similar condition could be created by removing component-4 in Fig 10. In this condition, which is called **Condition-I**, only the DC

motor (component-1), motor shaft (component-2) and the shaft bearing (component-3) are involved in, as shown in Fig 12 and the mathematical model is given as follows:

For electrical circuit, the equation is:

$$\boldsymbol{L \cdot \frac{di_a}{dt} = v_a - R \cdot i_a - K_b \cdot \omega_E} \tag{2.14}$$

For shaft rotation loop, there is:

$$\boldsymbol{I_{P1} \cdot \frac{d\omega_E}{dt} = K_m \cdot i_a - M_{BF}} \tag{2.15}$$

And ship translation loop does not even exist in this condition.

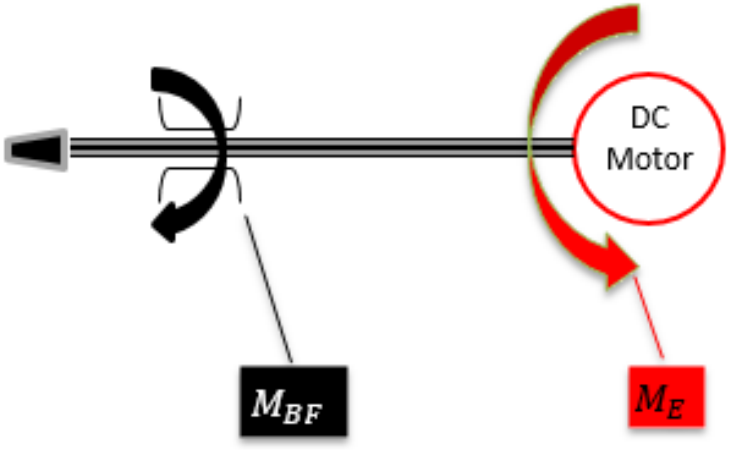

FIGURE 12: Torque Characteristic of **Condition-I**

By looking through Eq 2.14 and Eq 2.15, it is acknowledged that there are four parameters need to be identified: R, K_b, M_{BF} and I_{P1}. Among them, the value of R, K_b and I_{P1} are constant by their definition, now if the Coulomb Friction Model is adapted to describe M_{BF}, there is:

$$M_{BF} = \begin{cases} M_E & (M_E \leq M_S, \omega_E = 0) \\ M_C & (M_E > M_S, \omega_E \neq 0) \end{cases} \tag{2.16}$$

Eq 2.16 suggests that after overcoming static friction and the shaft starts to rotate, the value of M_{BF} could also be treated as constant. Although later on this assumption is found to be not very accurate when a small value of input voltage is added which results

in a low rotating speed (more details will be given in Chapter 3), in most cases it is reasonable enough to be adapted.

Based on the discussion given above, the method to identify parameters of Tito Neri's DC motor (along with I_{P1}) could now be introduced. If a step voltage with constant value $V_{a,i}$ is added on the system under **Condition-I**, when it reaches the steady state, there is:

$$\begin{cases} R \cdot I_{a,i} + K_m \cdot \Omega_{E,i} = V_{a,i} \\ K_m \cdot I_{a,i} - M_{BF} = 0 \end{cases} \tag{2.17}$$

In Eq 2.17, $I_{a,i}$ is the steady state value of current while $\Omega_{E,i}$ is the steady state value of angular speed, and both of them could be measured during test. Therefore, there are two equations containing three unknown variables (R, K_b and M_{BF}). Theoretically, by adding another step voltage whose value is $V_{a,i+1}$ and record the steady state value $I_{a,i+1}$, $\Omega_{E,i+1}$, a new equation set could be generated:

$$\begin{cases} R \cdot I_{a,i+1} + K_m \cdot \Omega_{E,i+1} = V_{a,i+1} \\ K_m \cdot I_{a,i+1} - M_{BF} = 0 \end{cases} \tag{2.18}$$

Apparently, by considering Eq 2.17 and Eq 2.18 simultaneously, the value of R, K_b and M_{BF} could be determined as follows:

$$\begin{cases} M_{BF} = \dfrac{V_{a,i+1} \cdot I_{a,i} - V_{a,i} \cdot I_{a,i+1}}{\Omega_{E,i+1} - \Omega_{E,i} \cdot \frac{I_{a,i+1}}{I_{a,i}}} \\ K_m = \dfrac{V_{a,i+1} - V_{a,i} \cdot \frac{I_{a,i+1}}{I_{a,i}}}{\Omega_{E,i+1} - \Omega_{E,i} \cdot \frac{I_{a,i+1}}{I_{a,i}}} \\ R = \dfrac{V_{a,i+1} - V_{a,i} \cdot \frac{\Omega_{E,i+1}}{\Omega_{E,i}}}{I_{a,i+1} - I_{a,i} \cdot \frac{\Omega_{E,i+1}}{\Omega_{E,i}}} \end{cases} \tag{2.19}$$

However, due to the noise of the measured data (as shown in Chapter 3), later on it is acknowledged that the values determined by just considering test results of two steady states are not qualified enough. Therefore, in order to reduce the impact of test error to an acceptable level, more test results under different steady states should be analyzed simultaneously by using the following method.

Now if n different steps of constant voltage are added on the system and the corresponding steady state values are recorded, the following equation set (in matrix form) could be formed:

$$\underbrace{\begin{bmatrix} I_{a,1} & \Omega_{E,1} & 0 \\ \vdots & \vdots & \vdots \\ I_{a,i} & \Omega_{E,i} & 0 \\ \vdots & \vdots & \vdots \\ I_{a,n} & \Omega_{E,n} & 0 \\ 0 & I_{a,1} & -1 \\ \vdots & \vdots & \vdots \\ 0 & I_{a,i} & -1 \\ \vdots & \vdots & \vdots \\ 0 & I_{a,n} & -1 \end{bmatrix}}_{A} \underbrace{\begin{bmatrix} R \\ K_m \\ M_{BF} \end{bmatrix}}_{\boldsymbol{x}} = \underbrace{\begin{bmatrix} V_{a,1} \\ \vdots \\ V_{a,i} \\ \vdots \\ V_{a,n} \\ 0 \\ \vdots \\ 0 \\ \vdots \\ 0 \end{bmatrix}}_{\boldsymbol{b}} \tag{2.20}$$

In order to solve Eq 2.20, which is over determined when $2n > 3$, the least-squares method should be applied. The mathematical theory of this method is explained below:

"Least-squares" actually means approximating the solution of this over determined system by minimizing the sum of squared residuals $S(x)$, whose funstion is defined as below:

$$S(x) = ||Ax - b||^2 \tag{2.21}$$

The minimum of $S(x)$ is found by setting the gradient to zero. And since the system shown in Eq 2.20 is linear, the linear least-squares should be adapted with the solution given below:

$$\hat{x} = (A^T A)^{-1} A^T \cdot b \tag{2.22}$$

In Matlab, if matrix A and vector $\boldsymbol{b}$ have already been created, using least-squares method to determine values inside vector $\boldsymbol{x}$ could be achieved by command $\boldsymbol{b}\backslash A$ or by using command:

$$\boldsymbol{x} = regress(\boldsymbol{b}, A)$$

Therefore, through data analysis of steady states under **Condition-I**, the value of R, K_m and M_{BF} could be determined. Now recall Eq 2.14 and Eq 2.15, it will be observed that the value of inductance L and moment of inertia I_{P1} still remain to be determined. Due to multiplying with the differential part, their values cannot be determined by

steady state analysis but could be determined by dynamic analysis, which is given in the next section.

2.3.2 Identification of L and I_{P1}

If a step voltage signal is added on a DC motor **while the motor shaft has already been blocked and forbidden to rotate**, in other words ω_E remains to be 0 so there is no back EMF effect, the equation to describe its behavior is:

$$L \cdot \frac{di_a}{dt} = V_{a,0} - R \cdot i_a \tag{2.23}$$

$V_{a,0}$ is the input nominal voltage. Since Eq 2.23 is a typical first order linear differential equation, by solving it, there is:

$$i_a(t) = \frac{V_{a,0}}{R} \cdot (1 - e^{-\frac{R}{L}t}) \tag{2.24}$$

From Eq 2.24 it is acknowledged that when time t goes to infinite, current $i_a(t)$ will approach its limit (or its ideal steady state value) $\frac{V_{a,0}}{R}$. Now if define the time τ_{ele} (in seconds) that the current takes to reach $1 - e^{-1} \approx 0.63$ of its ideal steady state value as **electrical time constant** ($i_a = \frac{V_{a,0}}{R} \cdot (1 - e^{-1}) \approx 0.63 \cdot \frac{V_{a,0}}{R}$), then:

$$\tau_{ele} = \frac{L}{R} \tag{2.25}$$

Eq 2.25 provides a convenient way to determine the value of electric inductance L: firstly determine the value of electrical time constant τ_{ele} by analyzing the test data of current, then since the value of electric resistance R has already been determined, there is:

$$\boldsymbol{L = \tau_{ele} \cdot R} \tag{2.26}$$

As for determining the value of I_{P1}, theoretically, it is always possible by measuring the dimension of the shaft then doing calculation. But again due to the chosen construction, that the motor shaft (component-2) consists of many sub-components whose dimensions are very difficult to be measured, the value determined through this way is not accurate enough. Therefore, another method, which is similar to the analysis of L given above, is raised up: if a step voltage is added on the DC motor, the behavior could be described by Eq 2.1 and 2.2. Since the effect of L could be neglected compared with back EMF effect on the change of voltage, the equations can be simplified as follows:

$$\begin{cases} 0 = v_a - R \cdot i_a - K_b \cdot \omega_E \\ I_{P1} \cdot \dfrac{d\omega_E}{dt} = K_m \cdot i_a - M_{BF} \end{cases} \tag{2.27}$$

From the upper equation it is acknowledged that $i_a = \frac{v_a - K_b \cdot \omega_E}{R}$, after substituting it into the second equation, a first-order linear equation will be generated as below:

$$I_{P1} \cdot \frac{d\omega_E}{dt} = K_m \cdot \frac{v_a - K_b \cdot \omega_E}{R} - M_{BF} \tag{2.28}$$

If there is no load and the friction torque M_{BF} could be assumed as a constant, Eq 2.28 can be solved with the result:

$$\omega_E(t) = (\frac{V_{a,0}}{K}_m - \frac{R \cdot M_{BF}}{K_m^2}) \cdot (1 - e^{-\frac{K_m^2}{R \cdot I_{P1}} \cdot t}) \tag{2.29}$$

Just like the definition of electrical time constant given ealier in this section, the time when the angular speed ω_E reaches $1 - e^{-1} \approx 63\%$ of its ideal steady state value, is defined as the **mechanical time constant** τ_{mech}:

$$\tau_{mech} = \frac{R \cdot I_{P1}}{K_m^2} \tag{2.30}$$

Therefore, since the value of K_m and R are already known, I_{P1} could be determined by:

$$\boldsymbol{I_{P1} = \frac{\tau_{mech} \cdot K_m^2}{R}} \tag{2.31}$$

2.3.3 Identification of $M_{F1} + M_{F2}$

Determining the value of M_{F1} and M_{F2} requires propulsion system running under dry condition, which is called **Condition-II**. Compared with **Condition-I**, the difference is obvious: under **Condition-II**, the bevel gear (component-4) is mounted back and the whole propulsion chain has been involved.

And if n steps of constant voltage is now added on the DC motor in **Condition-II**, the steady state of step i could be partly described by:

$$i_{gbt} \cdot i_{gbb} \cdot (K_m \cdot I'_{a,i} - M_{BF}) - i_{gbb} \cdot M_{F1} - M_{F2} = 0 \tag{2.32}$$

So the sum of M_{F1} and M_{F2} could be determined by:

$$\boldsymbol{i_{gbb} \cdot M_{F1} + M_{F2} = \frac{\sum_{i=1}^{n} i_{gbt} \cdot i_{gbb}(K_m \cdot I'_{a,i} - M_{BF})}{n}} \tag{2.33}$$

It is impossible to determine M_{F1} and M_{F2} individually, because component-6, the other bevel gear, cannot be removed without damaging the system. But this will not influence the coming work, since model simulation & validation only requires the sum value of M_{F1} and M_{F2}.

2.3.4 Identification of I_{P2} and I_{P3}

Unlike the identification of I_{P1} which requires a relatively complicated analysis, since the structure of the vertical shaft (component-5) and the propeller shaft (component-7) is very simple that could be treated as circular columns, the value of I_{P2} and I_{P3} are able to be determined just by measuring and calculating.

2.3.5 A summary of section 2.3

Based on the discussion presented in this section, it is acknowledged that identification of DC motor related parameters and mechanical parameters requires the propulsion system to operate under different dry conditions (**Condition-I and II**), therefore, corresponding dry-run tests will also be elaborated in Chapter 3.

2.4 A brief discussion about acquiring hydrodynamic parameters

The identification of hydrodynamic parameters, to be specific, the expression of resistance curve $R = \alpha \cdot v_s^e$ and expressions of propeller open-water diagram $K_T = X(J), K_Q = Y(J)$, traditionally should be acquired individually from towing tank resistance test and propeller open-water test. Yet the situation is special for Tito Neri and the tests have to be designed and conducted in special ways, which will be presented in Chapter 4 and Chapter 5.

Chapter 3

Identification of DC Motor Related Parameters & Mechanical Parameters

In this Chapter, the value of DC motor related parameters and mechanical parameters will be determined. As elaborated in last chapter, in order to acquire enough data to determine their values, dry-run tests under two different conditions should be carried out. After all the values have been determined, they will be validated together with the simulation model of the propulsion system under dry-run condition. Since the simulation model is structured on the mathematical model whose equations are transparent and valid, by comparing the result of simulation and experiment, the reliability of determined parameter values could be checked. Meanwhile, potential reasons that may lead error are also discussed in this Chapter.

3.1 Setup & Input Signal of Dry-run Tests

From section 2.3, it is acknowledged that the dry-run test should be conducted under two conditions, and the only difference between them is without or with the bevel gear (component-4). Therefore, in this Thesis, the dry-run test conducted under **Condition-I**, in which component-4 has been removed, is named as **Test-I** while the test conducted under **Condition-II** is named as **Test-II**. Obviously, the same test-setup and test procedure are applicable for both of them.

3.1.1 Setup of Dry-run Tests

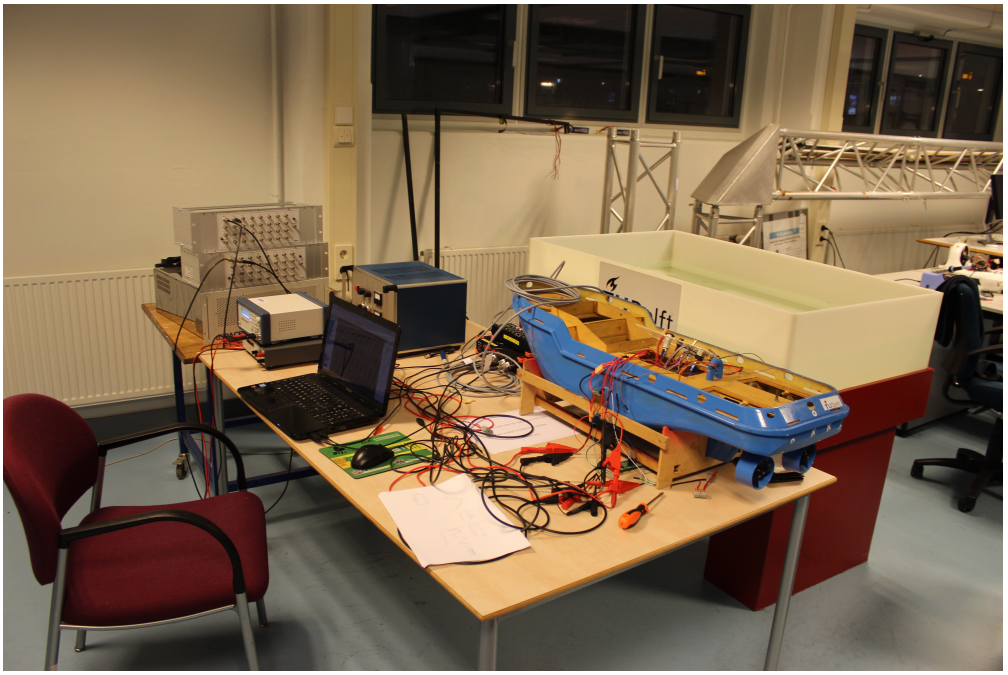

FIGURE 13: Test-setup designed by the author & teammates

Based on foregoing, the test-setup should include a signal generating system to provide the input voltage signal, a response measurement system to measure the required system response (in this case are current and rotating speed) and a recording system to record the measurement data. Fig 13 shows the setup designed by the author and his teammates.

To be specific, the list of equipment is given as follows:

- PC installed with specific dSPACE-MatLab software
- dSPACE-simulator
- Voltage Amplifier
- Allegro ACS712 Current Sensors (Portside & Starboard)
- RPM Sensors (Portside & Starboard)
- DEWE-43A Board and SIRIUS Board
- Laptop

The schematic block diagram is given in Fig 14 to make a clear view of the connections between equipments:

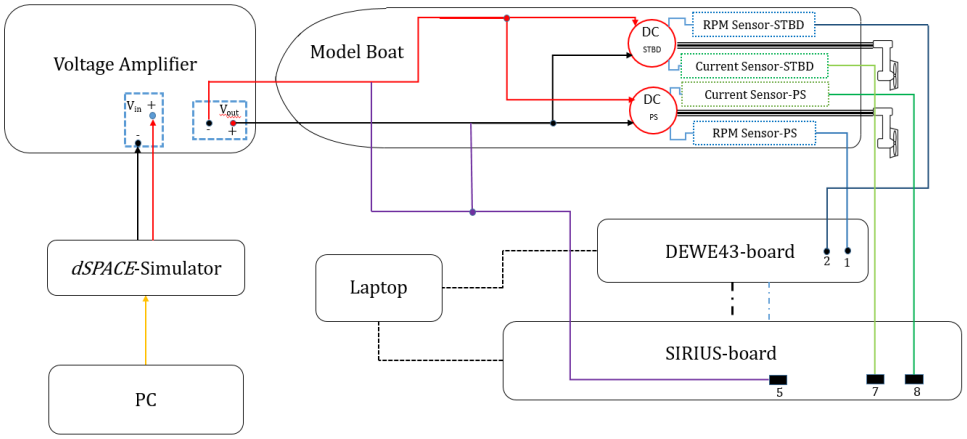

FIGURE 14: Schematic block diagram of dry-run test setup

As shown in Fig 14, there is a special PC installed with specific dSPACE-MatLab software (which is unable to shown in Fig 13), through which virtual waveform signals (for instance step signal) could be generated. The dSPACE-simulator is responsible for transforming these virtual signals to PWM voltage signals. Then, the voltage signal generated by dSPACE-simulator is added on DC motors after being amplified by the

Voltage Amplifier. To measure the responses of the propulsion system, one RPM sensor and one current sensor are amounted on each shaft-line. The values that they measured, together with the voltage signals will then be transferred to different channels of DEWE-43A Board and SIRIUS Board (RPM signal is treated as digital input while current signal is analog input). These dSPACE boards are connected to users laptop through USB cables and the data will be recorded by DEWE Software installed on the laptop.

The brand of DC motor is GRAUPNER 900BB TORQUE (Nr 6373), the datasheet of current sensor is given in Appendix A, and the introduction of boards is presented in Appendix B.

3.1.2 Choice of the Input Signal

According to section 2.3, the required input signal is "n different steps of constant voltage", and $2n$ must be greater than 3 for applying least-squares method later on. After considering the maximum supply voltage of the current sensor, which is 8 volts, the following signal was designed:

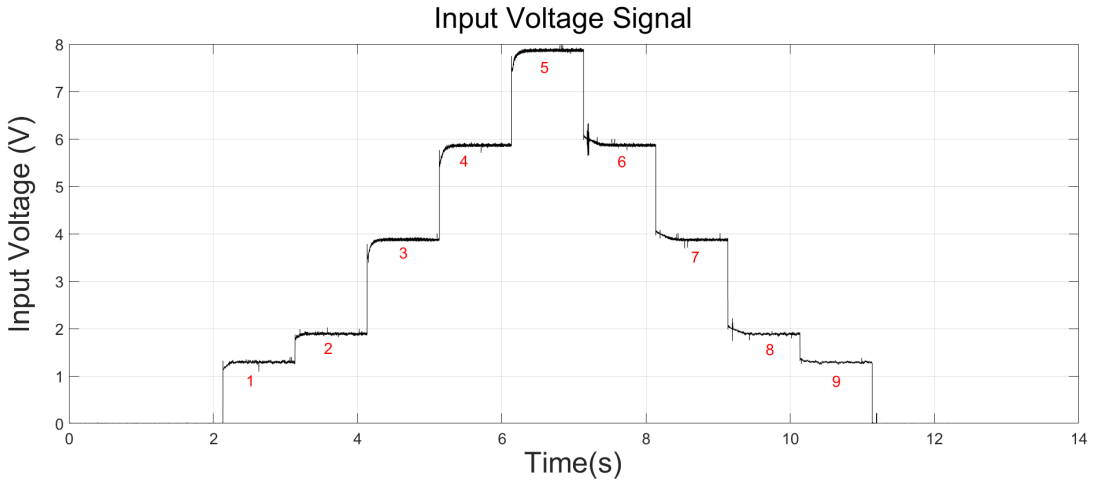

FIGURE 15: The Input Voltage Signal of Test-I and Test-II

As shown in Fig 15, there are 9 steps of constant voltage, ranging from 1.3 volts to 7.8 volts.

3.2 Analysis of Measured Data

After conducting the dry-run tests by using the setup introduced in last section, the data of motor speed and armature current was recorded. By using DEWE Sofware,

the recorded data is able to be transformed to a Matlab data file for analysis and the analyzed result will be used to determine the values of required parameters.

As mentioned before, the propulsion system has two individual shaft-lines, a portside one and a starboard one, therefore the data analysis is done individually.

The measurement data of Portside shaft-line in **Test-I** is shown in Fig 16:

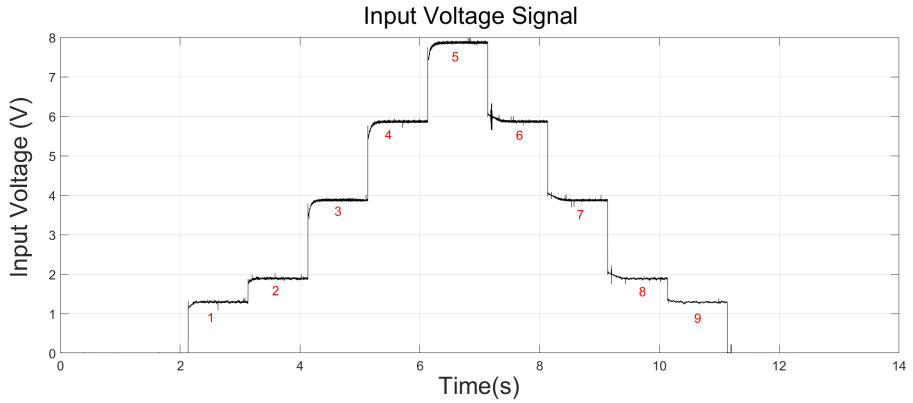

(a) The Input Voltage Signal

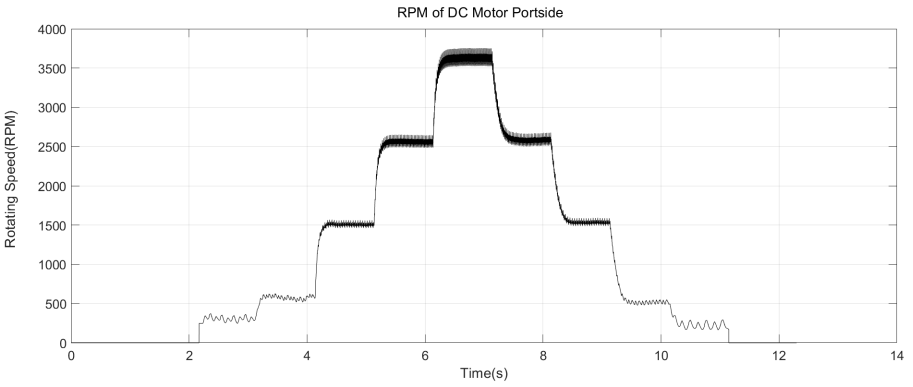

(b) Rotating Speed of Portside DC Motor

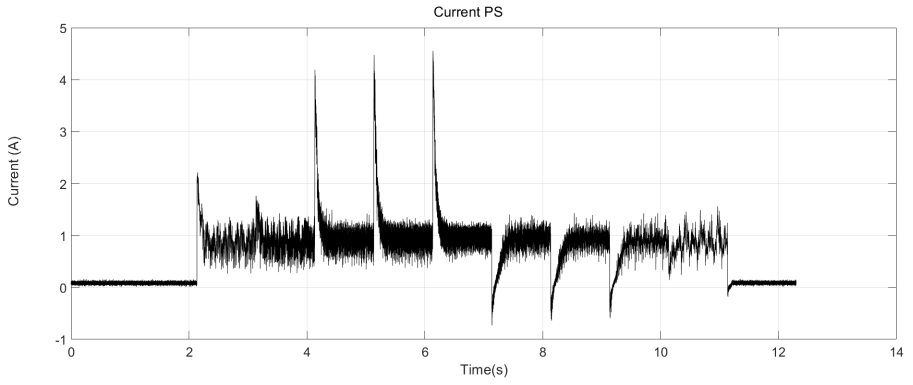

(c) Current of Portside

FIGURE 16: Test-I Portside Result

Fig 3.16(b) and Fig 3.16(c) indicate that although there is some noise, especially in Fig 3.16(c), when step voltages are given, the system is able to reach corresponding steady states.

Although there are 9 steps in total, the first 2 steps and the last 2 steps cannot be used for data analysis because the fluctuation is too obvious, and the trend is not very stable. Therefore, only the data from step 3 to step 7 should be analyzed.

To mitigate the effect of noise, at each step, the average value of measured data after it becomes relatively stable, is considered to be the steady state value. Table 3.1 shows the result of data analysis of Portside data in Test-I.

TABLE 3.1: **Average Value of input voltage, angular speed and current at Portside (Test-I)**

	Step 3	**Step 4**	**Step 5**	**Step 6**	**Step 7**
Voltage (V)	3.8715	5.8633	7.8667	5.8649	3.8707
Current (A)	0.9694	0.9807	1.0014	0.9881	0.9604
Ω_E (rad/s)	157.4619	266.6455	378.0969	269.1617	160.2212

The numbers shown in Table 3.1 will be applied for determining the value of Portside R, K_m and M_{BF} by using the method elaborated in section 2.3.1.

As for Starboard (Test-I) and Test-II, the same way to analyze the measured data (picking up the data of step 3 to step 7 and taking average) is still applicable. Based on the result, the steady state values to identify Starboard R, K_m, M_{BF} and $M_{F1} + M_{F2}$ for both sides could be provided.

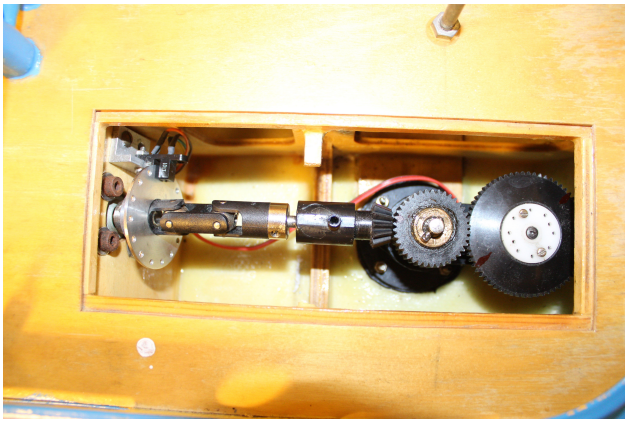

FIGURE 17: The structure of motor shaft

From section 2.3.2 it is acknowledged that the identification of L and I_{P1} requires analysis of dynamic state to determine electrical time constant τ_{ele} and mechanical time constant τ_{mech}. However, due to the chosen construction of shaft-line, the motor-shaft (shown in Fig 17) cannot be blocked, therefore a few more discussion is needed and will be presented in next section.

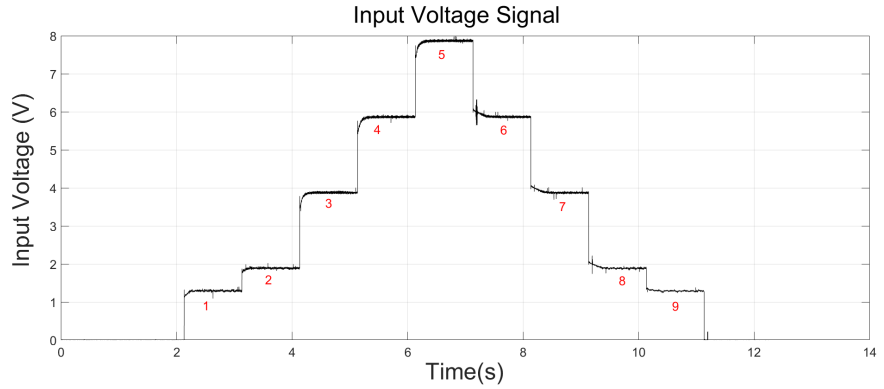

(a) The Input Voltage Signal

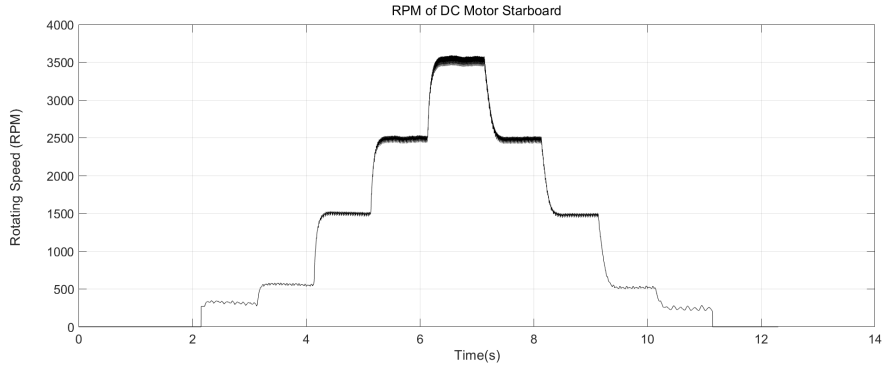

(b) Rotating Speed of Starboard DC Motor

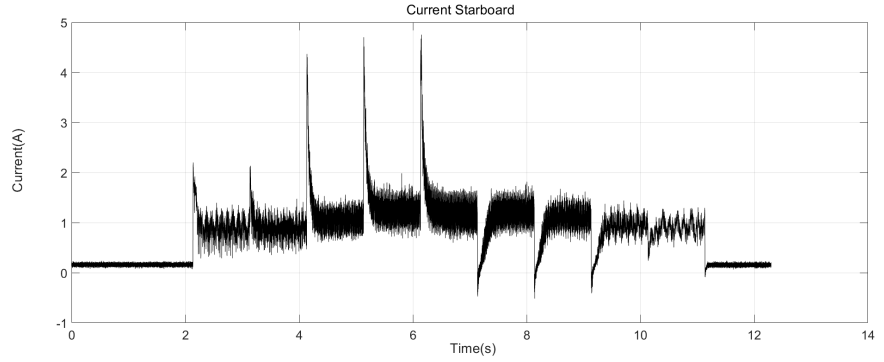

(c) Current of Starboard

FIGURE 18: Test-I Starboard Result

TABLE 3.2: **Average Value of input voltage, angular speed and current at Starboard (Test-I)**

	Step 3	**Step 4**	**Step 5**	**Step 6**	**Step 7**
Voltage (V)	3.8715	5.8633	7.8667	5.8649	3.8707
Current (A)	1.1029	1.2561	1.1982	1.2199	1.1283
Ω_E (rad/s)	157.1673	260.9594	369.7664	260.0559	155.0502

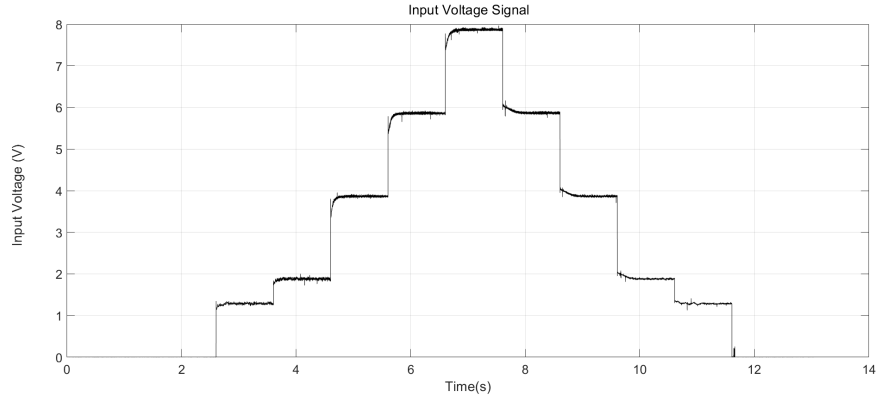

(a) The Input Voltage Signal

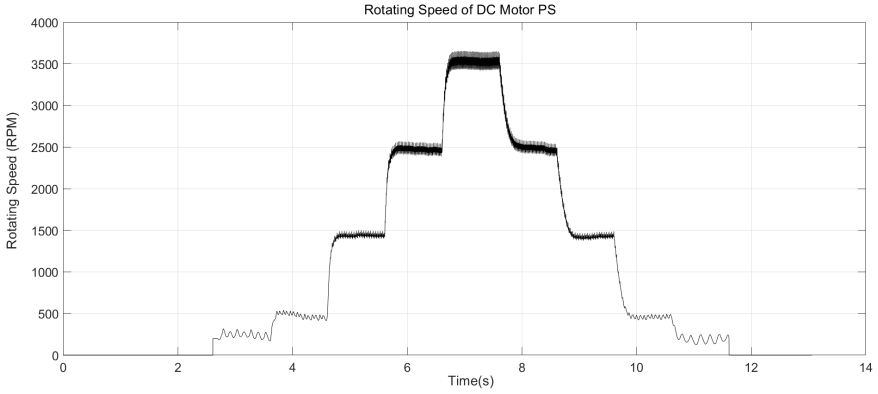

(b) Rotating Speed of Portside DC Motor

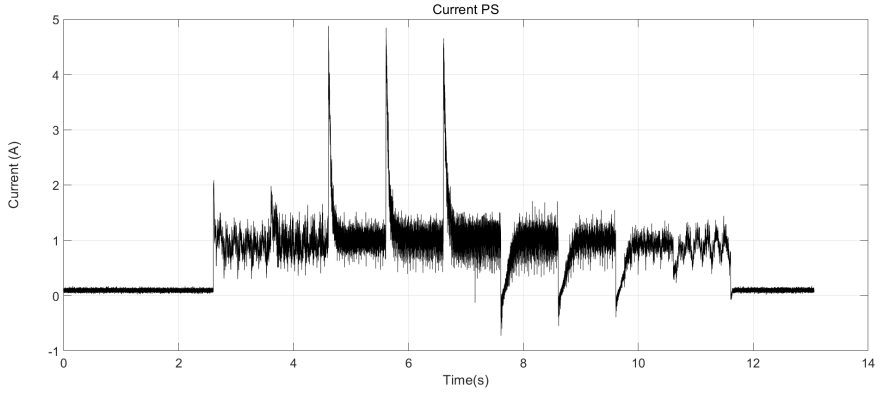

(c) Current of Portside

FIGURE 19: Test-2 Portside Result

TABLE 3.3: **Average Values of input voltage, angular speed and current at Portside (Test-2)**

	Step 3	**Step 4**	**Step 5**	**Step 6**	**Step 7**
Voltage (V)	3.8625	5.8586	7.8669	5.8657	3.8657
Current (A)	1.0289	1.0571	1.0756	1.0433	1.0165
Ω_E (rad/s)	150.5462	257.6103	367.4970	258.7384	148.7701

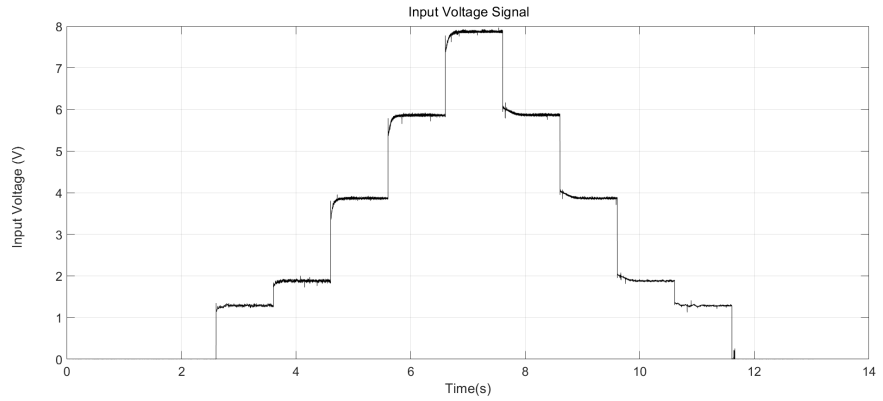

(a) The Input Voltage Signal

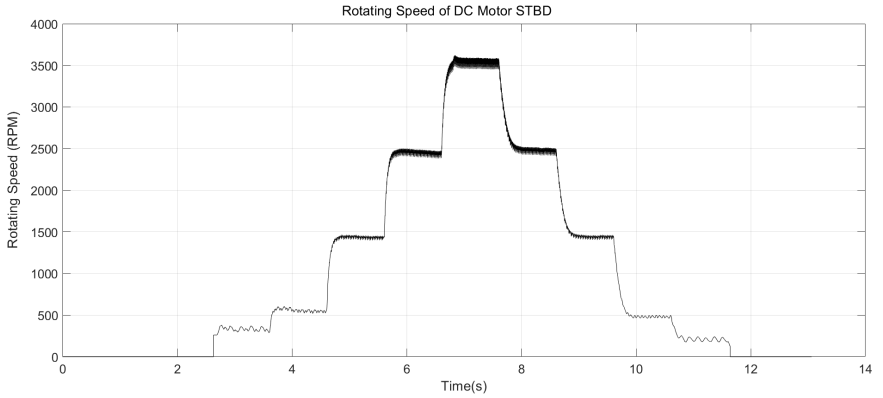

(b) Rotating Speed of Starboard DC Motor

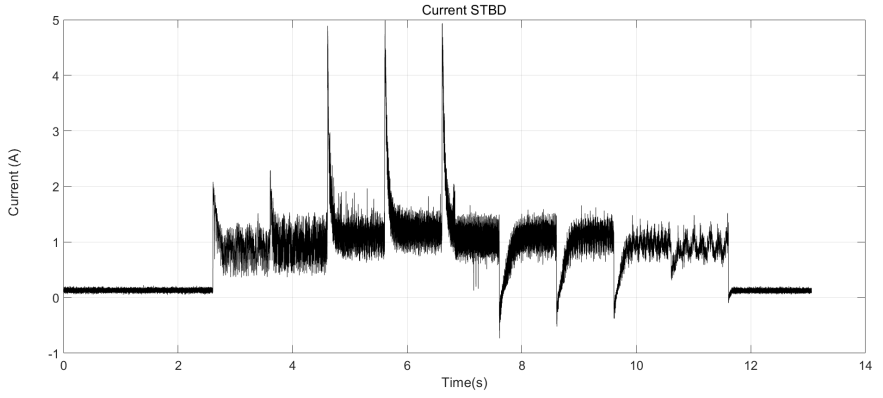

(c) Current of Starboard

FIGURE 20: Test-2 Starboard Result

TABLE 3.4: **Average Values of input voltage, angular speed and current at Starboard (Test-2)**

	Step 3	**Step 4**	**Step 5**	**Step 6**	**Step 7**
Voltage (V)	3.8625	5.8586	7.8669	5.8657	3.8657
Current (A)	1.1592	1.2259	1.1088	1.1430	1.1280
Ω_E (rad/s)	150.3995	257.0141	370.6636	259.7126	150.7998

3.3 Value Determination of Required Parameters

3.3.1 Value Determination of R, K_b and M_{BF}

So now, if the method demonstrated in section 2.3.1 is applied, there is:

$$\underbrace{\begin{bmatrix} I_{a,3} & \Omega_{E,3} & 0 \\ \vdots & \vdots & \vdots \\ I_{a,n} & \Omega_{E,n} & 0 \\ \vdots & \vdots & \vdots \\ I_{a,7} & \Omega_{E,7} & 0 \\ 0 & I_{a,3} & -1 \\ \vdots & \vdots & \vdots \\ 0 & I_{a,n} & -1 \\ \vdots & \vdots & \vdots \\ 0 & I_{a,7} & -1 \end{bmatrix}}_{A} \underbrace{\begin{bmatrix} R \\ K_m \\ M_{BF} \end{bmatrix}}_{\boldsymbol{x}} = \underbrace{\begin{bmatrix} V_{a,3} \\ \vdots \\ V_{a,n} \\ \vdots \\ V_{a,7} \\ 0 \\ \vdots \\ 0 \\ \vdots \\ 0 \end{bmatrix}}_{\boldsymbol{b}} \tag{3.1}$$

After substituting the data given in Table 3.1 into Eq 3.1, by using the Matlab command, vector x could now be calculated. And the result is:

$$\begin{bmatrix} R \\ K_m \\ M_{BF} \end{bmatrix} = \begin{bmatrix} 1.0418 \\ 0.0181 \\ 0.0177 \end{bmatrix}$$

Which indicates that for **Portside** shaft-line, $R = 1.0418\Omega$, $K_m = 0.0181N/m \cdot A$, $M_{BF} = 0.0177N \cdot m$.

For Starboard shaft-line, by using the same calculation method, there is:

$$\begin{bmatrix} R \\ K_m \\ M_{BF} \end{bmatrix} = \begin{bmatrix} 0.8923 \\ 0.0183 \\ 0.0217 \end{bmatrix}$$

Which indicates that for **Starboard** shaft-line, $R = 0.8923\Omega$, $K_m = 0.0183N/m \cdot A$, $M_{BF} = 0.0217N \cdot m$.

Like other parameters whose value will be determined in this section, the value of R, K_b and M_{BF} is going to be validated in next section together with the simulation model.

3.3.2 Value Determination of $M_{F1} + M_{F2}$

Now if the method elaborated in section 2.3.3 is recalled, for Portside, the value of $M_{F1} + M_{F2}$ could be determined by:

$$M_{F1} + M_{F2} = \frac{\sum_{n=3}^{7} 3 \cdot (K_m \cdot I'_{a,n} - M_{BF})}{5} \tag{3.2}$$

After calculation, the sum of M_{F1} and M_{F2} is $0.00352N \cdot m$, which indicates that at **Portside**:

$$M_{F1} + M_{F2} = 0.00352N \cdot m$$

As for **Starboard**, the sum of M_{F1} and M_{F2} is:

$$M_{F1} + M_{F2} = 0.00351N \cdot m$$

3.3.3 Value Determination of L & I_{P1}

As mentioned before, if the method given in section 2.3.2 would be applied to determine the value of L, the key point when carrying out the measurement is "forbid the motor shaft rotating" in order to eliminate the back EMF effect. This is very difficult to conduct on Tito Neri because it is highly possible to damage the motor shaft.

However, after examining Fig 16 and Fig 18, it is observed that current changes much faster than the shaft rotating speed: when a new step voltage is added, the current only takes 0.005 to 0.006 seconds to reach its peak while the shaft rotating speed takes 0.3 to 0.4 seconds to reach its next steady state. Therefore, a rough assumption could be made: since shaft rotating speed changes too slowly compared with current, the back EMF effect could be ignored among the process in which current increases to its peak. With this assumption, the electrical time constant of this DC motor driven system could also be calculated based on the recorded data of Test-I, which is shown in Fig 21.

In Fig 21, among each peak there are three indicating points: at the lowest one the current started to increase and at the highest one the current reaches the peak. The electrical time constant could be roughly determined by the difference of abscissa between the lowest point and the middle point. A detailed procedure is given below:

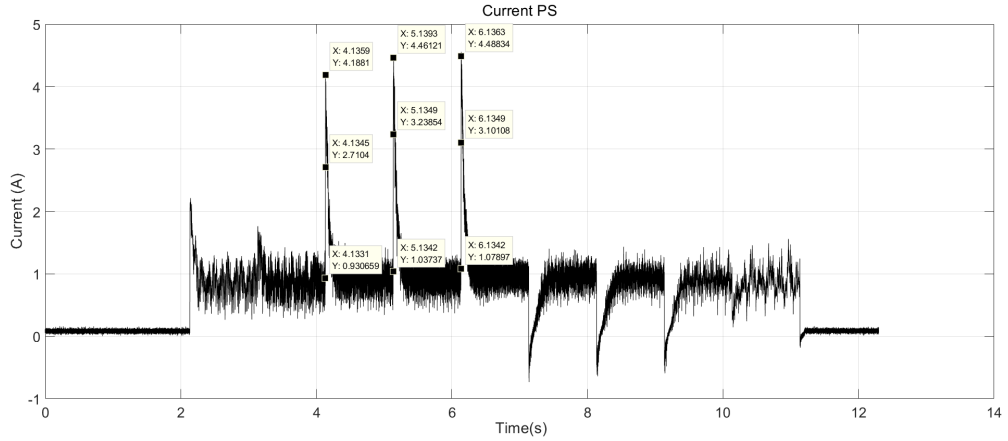

(a) Current Portside with Related Data

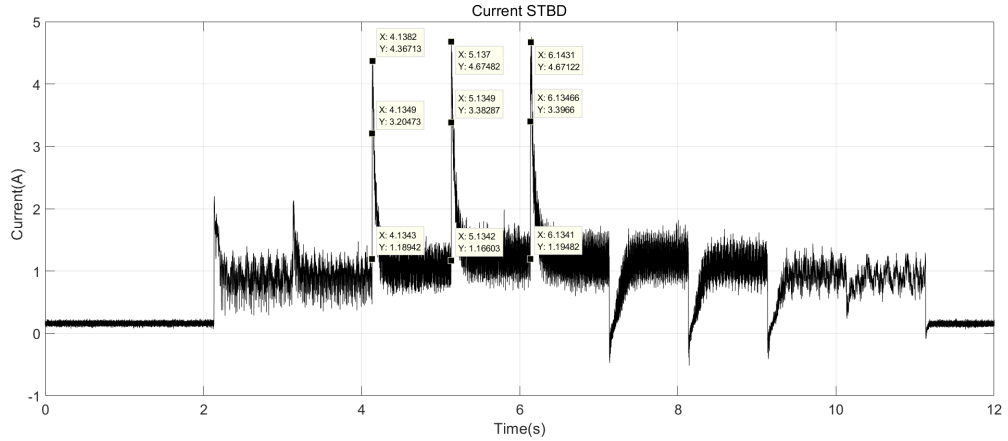

(b) Current Starboard with Related Data

FIGURE 21: Portside and Starboard Current with Related Data

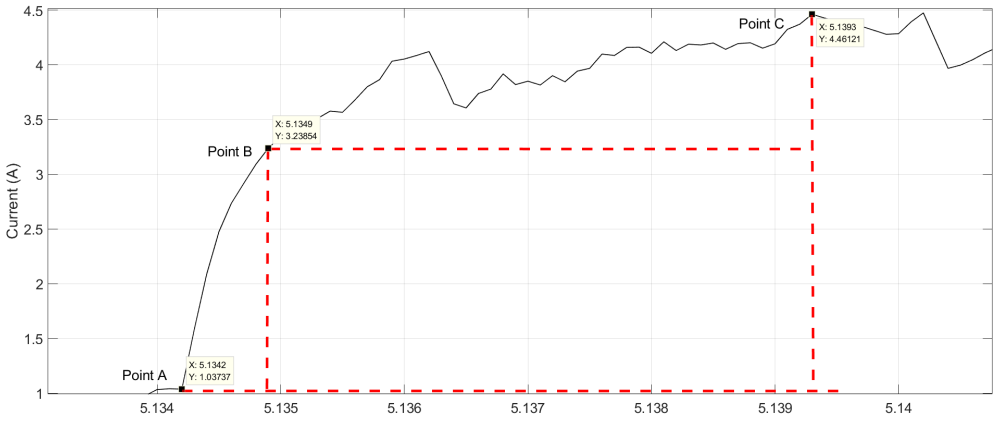

FIGURE 22: Analysis of the second peak

The second peak in Fig 3.21(a) is chosen to elaborate the calculation procedure. As shown in Fig 22, at Point A current starts to increase from 1.03737, and at Point C

it reaches the peak 4.46121. Therefore, by calculation, $(4.46121 - 1.03737) \cdot (1 - \frac{1}{e}) + 1.03737 \approx 3.238A$, another indicating point (Point B) should have a vertical ordinate of 3.238. After Point B has been defined, according to the definition of electrical time constant, $\tau_{ele} = x_B - x_A = 0.0007$. Therefore, based on Eq 2.26, $L = \tau_{ele} \cdot R = 0.00073H$.

After analyzing all peaks shown in Fig 21 and applying the value of R which has been determined in section 3.3.1, the electric inductance of **Portside** shaft-line is:

$$L = 0.000739H$$

For **Starboard** shaft-line, the value is:

$$L = 0.000557H$$

3.3.4 Discussion about the value of Moment of Inertia

As mentioned in section 2.3.2 and section 2.3.4, the value of I_{p1},I_{p2} and I_{p3} has to be determined through different ways due to the chosen construction of shaft-line.

As is all known, the moment of inertia of a circular column could be calculated as follows:

$$I_p = \frac{mr^2}{2} \tag{3.3}$$

In which m stands for the mass, which is also equal to $\rho \cdot V$, and r stands for the radius of the column. Based on Eq 3.3, the calculation result of I_{p2} is given below:

$$\begin{aligned} I_{p2} &= \frac{m_G r_G^2}{2} + \frac{m_s r_s^2}{2} \\ &= 2.06293 \times 10^{-6} (kg \cdot m^2) \end{aligned}$$

Since component-5 contains two parts, a plastic gear and a steel shaft, the result of I_{p2} shown above is a combination. The detailed procedure in which ρ and V are involved is omitted here.

Likewise, the calculation result of I_{p3} is:

$$\begin{aligned} I_{p3} &= \frac{m_p r_p^2}{2} + \frac{m_s r_s^2}{2} \\ &= 1.9635 \times 10^{-8} (kg \cdot m^2) \end{aligned}$$

While measuring the dimension of component-5 and 7, the dimensions of component-1 was also measured roughly. Based on the measurement result, I_{p1} is calculated below:

$$\begin{aligned} I_{p1} &= \sum_{i=1}^{N} \frac{m_i r_i^2}{2} \\ &= 1.11052 \times 10^{-5} (kg \cdot m^2) \end{aligned}$$

Although the result shown above is not accurate enough and cannot be used in reality, it provides the lower limit of I_{p1} since some parts of component-1 are unable to be measured. In other words, the actual value of I_{p1} should definitely be larger than $1.11052 \times 10^{-5} (kg \cdot m^2)$.

And since Eq 2.31 indicates that I_p of motor torque could be determined by mechanical time constant τ_{mech}. Therefore, by examining the result of Test-I, which is shown in Fig 23:

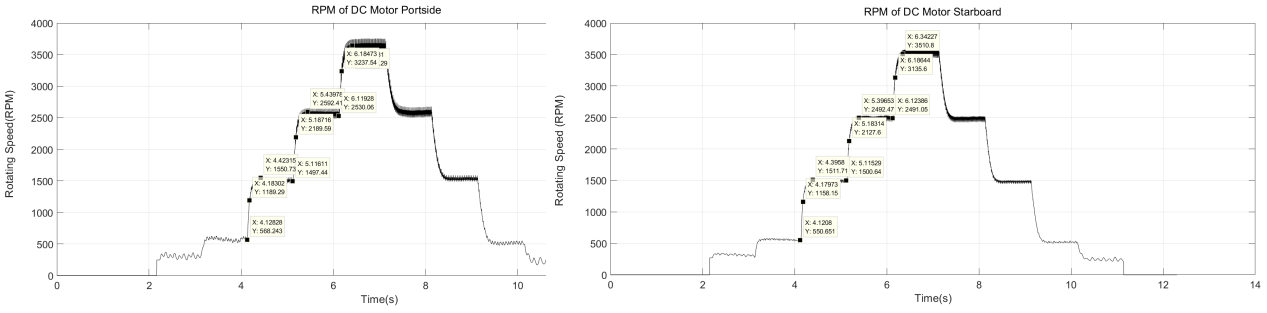

(a) n_E Portside with Related Data (b) n_E Starboard with Related Data

FIGURE 23: Portside and Starboard n_E with Related Data

The second peak in Fig 23 is zoomed in and shown in Fig 24. The calculation procedures are omitted here because they are exactly the same as the ones of L. After calculation, the I_p of **Portside** motor shaft is:

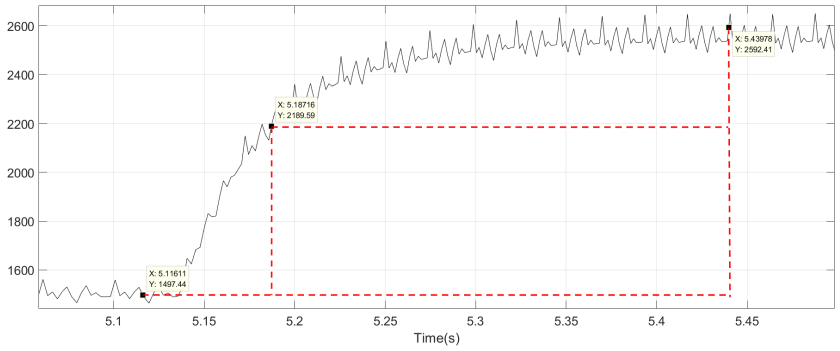

FIGURE 24: Analysis of the second peak (RPM)

$$I_{p1} = 1.994 \times 10^{-5}(kg \cdot m^2)$$

As for the **Starboard** motor shaft, the result is:

$$I_{p1} = 1.974 \times 10^{-5}(kg \cdot m^2)$$

Since both values given above are larger than $1.11052 \times 10^{-5}(kg \cdot m^2)$, so far they could be thought as reasonable.

*Summary of the values acquired so far

Until now, all the DC motor related parameters as well as mechanical parameters have been determined, their values are summarized in Table 3.5:

TABLE 3.5: **DC motor related & Mechanical Parameters**

	Portside	**Starboard**
$R\ (\Omega)$	1.0418	0.8923
$L\ (H)$	0.000739	0.000557
$K_m\ (N \cdot m/A)$	0.0181	0.0183
$M_{BF}\ (N \cdot m)$	0.0177	0.0217
$M_{F1} + M_{F2}\ (N \cdot m)$	0.00352	0.00351
$I_{p1}\ (kg \cdot m^2)$	1.994×10^{-5}	1.974×10^{-5}
$I_{p2}\ (kg \cdot m^2)$	2.06293×10^{-6}	2.06293×10^{-6}
$I_{p3}\ (kg \cdot m^2)$	1.9635×10^{-8}	1.9635×10^{-8}

3.4 Model Validation of Dry-run Tests

Before applying the parameters shown in Table 3.5 for future use, their values need to be validated. In order to do this, the best way is: building the simulation model of Tito Neri's propulsion system (under dry-run condition) with the parameters determined so far, and compare the model output (angular speed & current) with the measured data when same input voltage signal is added. Therefore, validation of parameters has been combined with model validation.

From section 3.1 it is acknowledged that there are two dry-run tests undertaken: Test-I and Test-II. Since they reflect two different circumstances of the propulsion system (with and without the bevel gear), and their conceptual models are also different, the simulation models should be built and validated individually as well. Therefore, in

section 3.4.1 the simulation model of Test-I will be presented, together with the output comparison between the simulation model and the test results. Once they do not match perfectly with each other, the leading reasons will also be discussed. And in section 3.4.2 the information of Test-II will be given.

3.4.1 The Simulation Model & related Discussions of Test-I

The conceptual model of a single shaft-line under Test-1 could be summarized into two basic equations: Eq 2.14 and 2.15, which are given below:

$$\begin{cases} L \cdot \dfrac{di_a}{dt} = v_a - R \cdot i_a - K_b \cdot \omega_E \\ I_{P1} \cdot \dfrac{d\omega_E}{dt} = K_m \cdot i_a - M_{BF} \end{cases}$$

Based on these two equations, by using relative blocks in Simulink, the simulation model of a single shaft-line is shown in Fig 25:

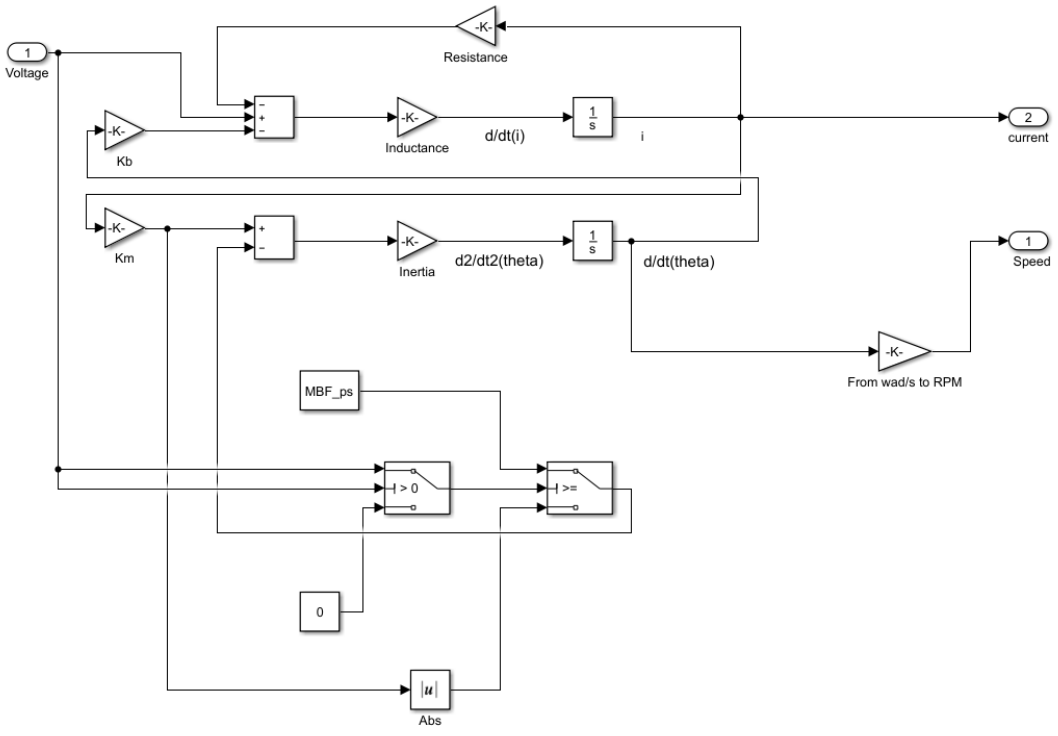

FIGURE 25: Simulation model of a single shaft-line under Test-I

Clearly, the input of this model is the voltage signal and the outputs, or the state variables, are current and rotating speed. The two cycles in the simulation model indicate the two basic equations, and the interaction between those two equations is reflected by the block K_b and K_m.

Another point of this model that needs to be addressed is the friction part, whose expression is summarized in Fig 3.4. Unlike the traditional expression of Coulomb Friction Model, in which the static friction and the kinetic friction is switched based on the maximum static friction and rotating speed, the switch function in Fig 3.4 is based on input voltage. The reason behind this will be given in later paragraphs in this section, together with more discussions about the choice of this friction model.

$$M_{BF} = \begin{cases} 0 & (v_a = 0V) \\ |K_m \cdot i_a| & (v_a < 1.2V) \\ 0.0177N \cdot m & (v_a \geq 1.2V) \end{cases} \tag{3.4}$$

So now if both shaft-lines, the input voltage signal and test results (fro comparison) are all included, the final version of the simulation model looks like the picture given below:

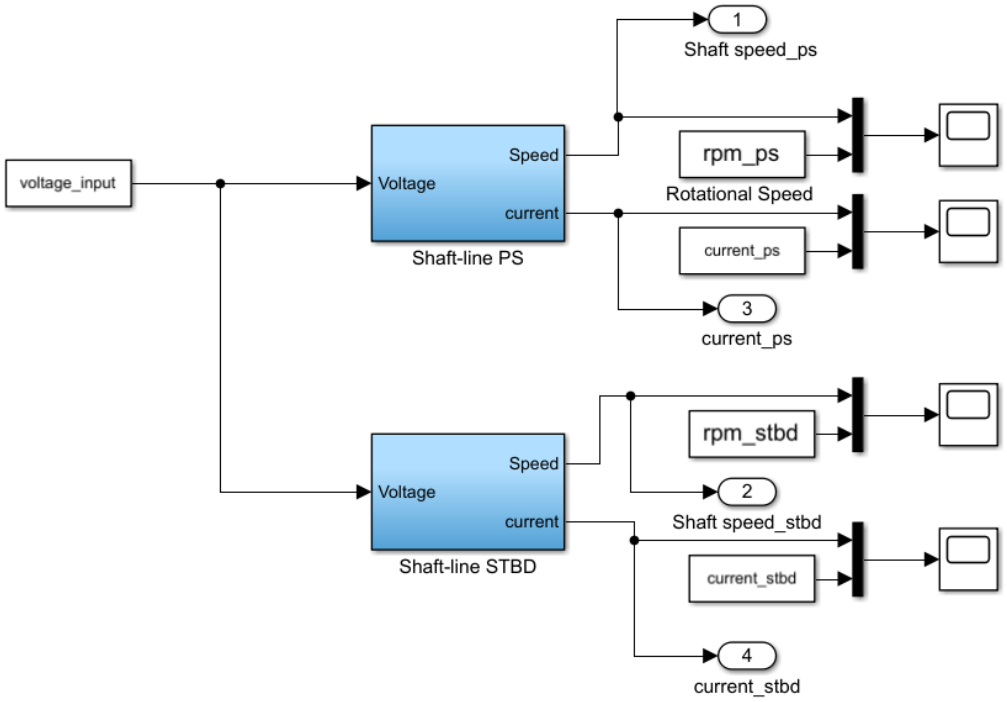

FIGURE 26: Simulation model of whole Propulsion System

In Fig 26, the models of single shaft-line shown in Fig 25 are included as subsystems in the blue blocks, and the input voltage signal as well as the recorded test results are imported from related Matlab data files. In the "scope" blocks, the simulation results will be graphed and compared to the test results. And Fig 27, 28, 29, 30 shows the result comparison.

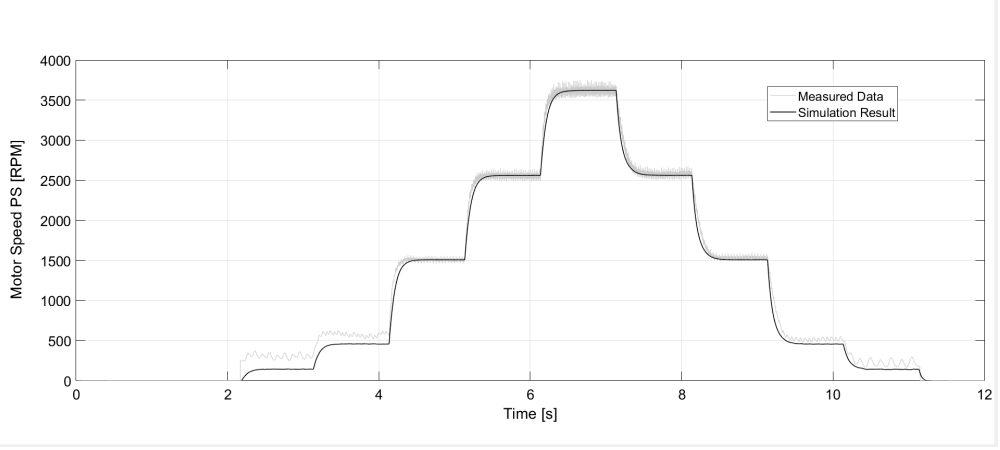

FIGURE 27: Result Comparison of Test-I: Rotating Speed Portside

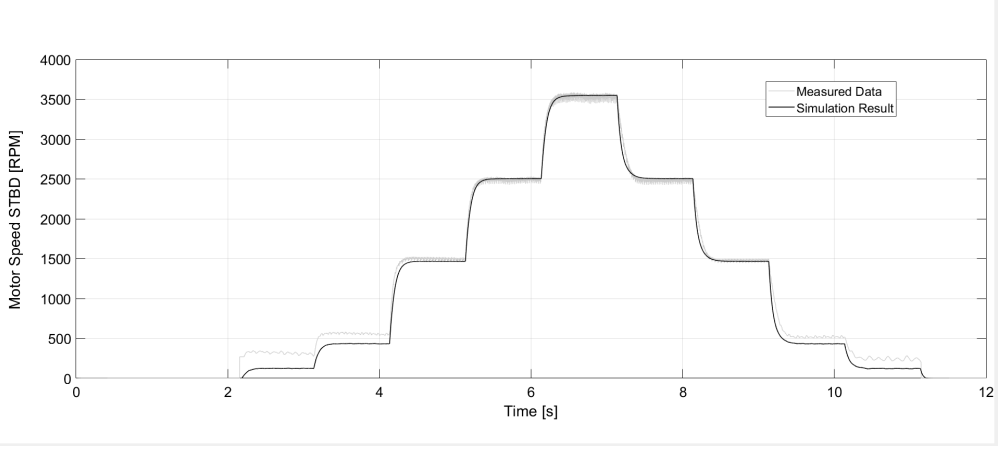

FIGURE 28: Result Comparison of Test-I: Rotating Speed Starboard

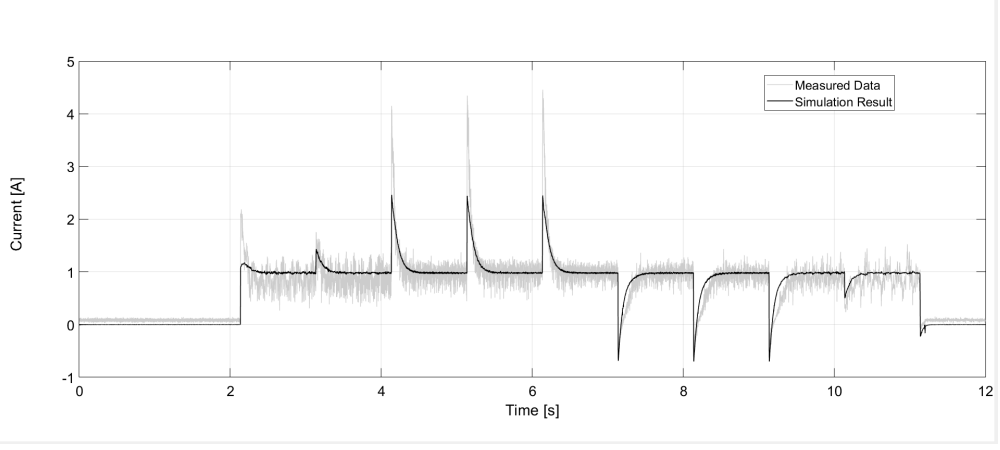

FIGURE 29: Result Comparison of Test-I: Current Portside

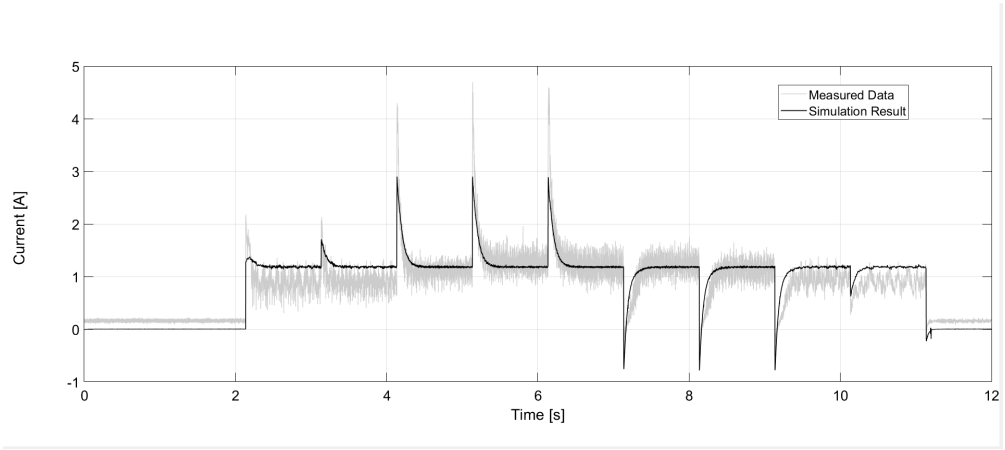

FIGURE 30: Result Comparison of Test-I: Current Starboard

From the four figures shown above, it is acknowledged that the running results of the simulation model are well matched with the recorded test data, especially at step 3 to step 7 (the five steps that were chosen to undertake the data analysis in section 3.2). However, at the other four steps when low nominal voltages were supplied, the simulation result of current is higher than the recorded data while the simulation result of rotating speed is lower compared to the recorded data. Below will discuss the reason.

The perfect match of step 3 to step 7 indicates that the parameter values determined in section 3.3.1 and 3.3.3 are precise enough if the supplied nominal voltage ranges from $3.8V$ to $8V$. Among those parameters, considering R, L, K_m and I_{p1} as constants is very logical and convincing. In other words, their values are not influenced by supplied voltage (and of course not by shaft speed or other factors). Therefore, the most suspectable parameter is M_{BF}.

Now if assuming in the simulation model, at step 2 (when supplied voltage is $1.5V$) the real value of friction torque is $M'_{BF,2}$, which is **smaller** than the value determined before, while the other parameters keep their value which has been determined before, based on Eq 2.14 and 2.15, in steady state, there is:

$$\begin{cases} V_{a,2} - R \cdot I_{a,2} - K_b \cdot \Omega_{E,2} & = 0 \\ K_m \cdot I_{a,2} - M'_{BF,2} & = 0 \end{cases}$$

Which indicates that the simulation result of current and angular speed in steady state is:

$$\Omega_{E,2} = \frac{V_{a,2}}{K_m} - R \cdot \frac{M'_{BF,2}}{K_m^2}$$

$$I_{a,2} = \frac{M'_{BF,2}}{K_m}$$

Apparently, after applying the new value $M'_{BF,2}$, the simulation result of current ($I_{a,2}$) will decrease and meantime, the simulation result of angular speed ($\Omega_{E,2}$) will increase, and both of them will be closer to the recorded data compared with the result shown in Fig 27 to Fig 30.

The analysis given above makes a clear statement that the key factor leading to the deviation between simulation result and recorded data is: the expression of friction torque which is given in Eq 3.4 is not accurate, or to be specific, not complete enough. Some information,especially the condition under low supplied voltage is missing.

In section 2.3.1 and one former graph of this section, there is a short discussion about the choice of friction model of M_{BF}, and here a more detailed research will be elaborated. There are many friction models to describe the friction phenomenon in a rotating system, and the one chosen in this thesis is **Coulomb Friction Model**. A Coulomb friction model does not depend on the velocity magnitude and its expression is a switching function similar to Eq 2.16.

Due to its conciseness, Coulomb Friction Model has been widely used and in most cases it could give a good description of the friction phenomenon. However, in the paper written by Tegoeh Tjahjowidodo, Farid Al-Bender, and Hendrik Van Brussel [3], the authors suggested that more complete (also more complicated) friction models, such as Stribeck Friction Model, LuGre Friction Model or GMS Friction Model should be adapted in order to get a more precise simulation result under some particular circumstances, for instance when the rotating motion starts, stops or inverses. According to the example given in the paper (which is shown in Fig 31), the more complete the friction model is, the closer the simulation result compares to reality.

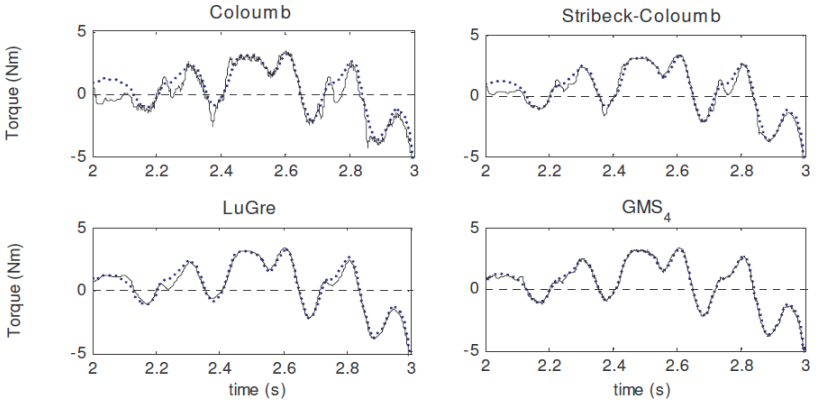

FIGURE 31: Examples given in the Paper [3]

Yet there remains an issue when adapting these friction models: the expressions of them are hard to derive therefore some special experiments need to be designed, and high-accuracy measurement is required when those experiments are undertaken. With this limitation, it is almost impossible to determine those expressions in the case of Tito Neri because of the instability of the voltage-amplifier and current sensors.

For our case, Coulomb Friction Model may not be the precisest one, but it is indeed the optimal one: this type of model is very simple to determine and to build. Besides, it is already suitable enough for a large range of input voltage. Another discussion should be made on Eq 3.4, as mentioned before, is about the switch function, which is unlike the traditional form (given in Eq 2.16) and is based on input voltage. This is because the value of maximum static friction cannot be precisely determined by our test-setup, and the motor shaft started to rotate when the input voltage increased to $1.2V$. Therefore, in Eq 3.4, when input voltage is lower than $1.2V$, M_{BF} is assumed to be equal to the external torque (torque provided by DC motor), and when input voltage is higher than $1.2V$, M_{BF} will switch to the determined value.

To summarize, all the parameter values determined so far are valid enough to be applied in future work.

3.4.2 The Simulation Model & related Discussions of Test-II

The simulation model of Test-II is almost the same as Test-I so the related figures will not be presented here, the difference is: based on Eq 2.12 and 2.15, M_{F1}, M_{F2}, I_{P2}, I_{P3} are now included in the shaft-line model and some coefficients are changed due to gear reduction ratio.

Result comparison between the simulation model and recorded test data is shown below:

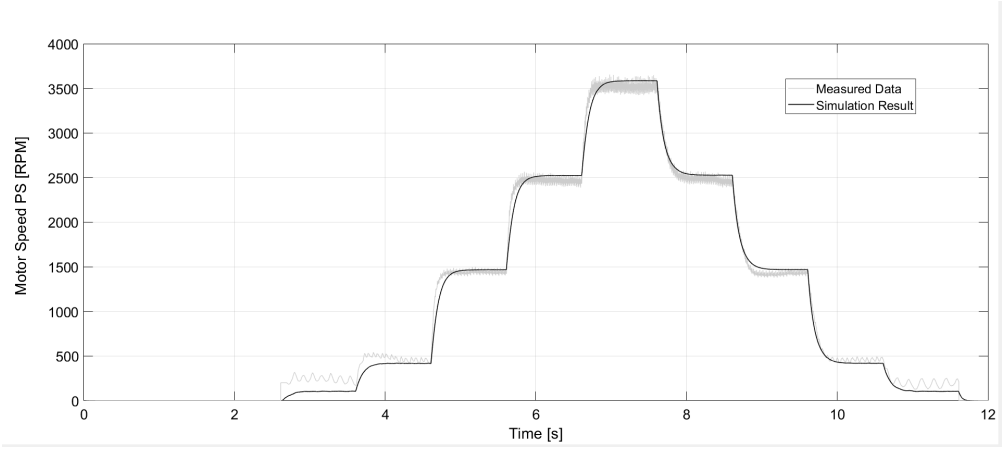

FIGURE 32: Result Comparison of Test-II: Rotating Speed Portside

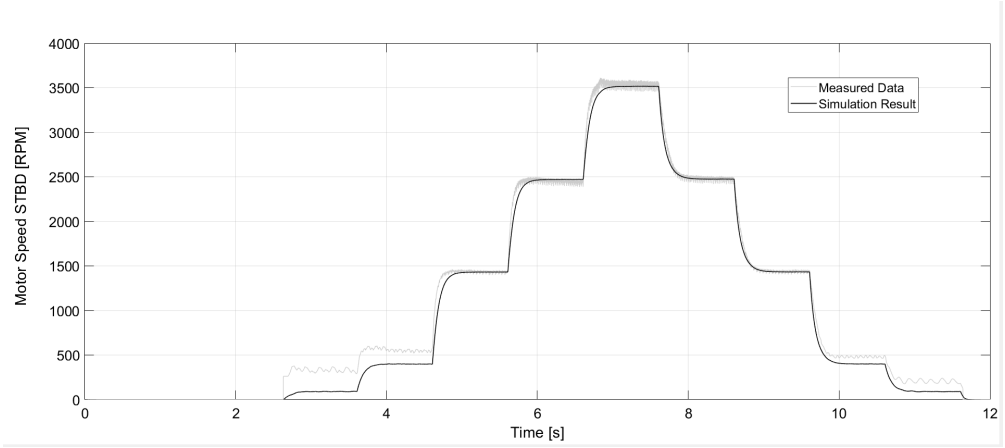

FIGURE 33: Result Comparison of Test-II: Rotating Speed Starboard

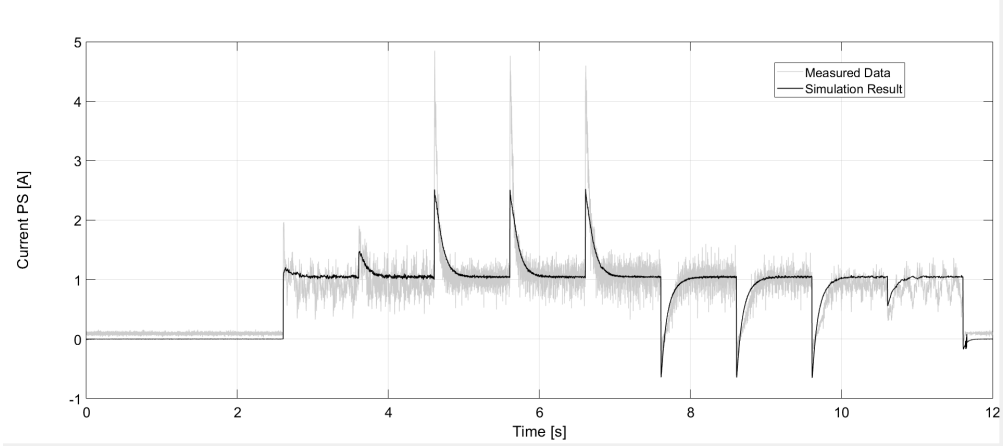

FIGURE 34: Result Comparison of Test-II: Current Portside

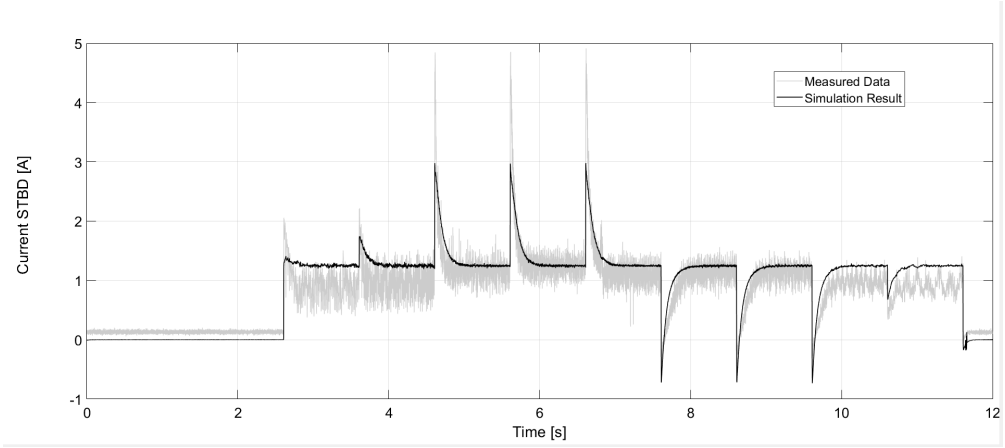

FIGURE 35: Result Comparison of Test-II: Current Starboard

The result shown in Fig 32 to Fig 35 indicates that after including all the determined parameter values, the simulation result is still able to match well with the recorded data. However, there is another odd phenomenon which exists in both Test-I and Test-II: compared with motor rotating speed, the difference between simulation result and

measured test data in armature current is more obvious. This is mainly because of the asymmetrical behavior of measured armature current: in Fig 29, 30, 34 and 35, it is clearly shown that at step 3 to step 5 when increasing step voltages are given, height of the peaks of measured data (the grey solid line) are almost as twice as the height of peaks at step 6 to step 8 when decreasing step voltages are given. This is sort of unusual after considering the fact that the input voltage (shown in Fig 15) added to the DC motor is symmetrical. With this input signal, and if the system behavior is determined by the mathematical model established in section 2.1.2, the system response is also expected to be symmetrical. Therefore, there are two possible reasons leading to this asymmetrical behavior. The first reason is the reliability of current sensor: by looking through the noise level under steady state of measured data, it is evident that the reliability of these two current sensors is poor, then needless to mention their reliability under dynamic state. Another reason that may lead to this asymmetrical behavior is: there are some unknown characteristics in this system, such as the difference in physical phenomenon between speed increasing and decreasing stage.

But all in all, based on the result comparison between simulation model and test data of Test-I and Test-II, such conclusion that all the parameters identified in Table 3.5 are valid enough for most cases could be drawn. To make this conclusion more convincing, the result comparison of other two dry-run tests is given in Appendix C, and good matches between experimental and simulation result are clearly shown.

Chapter 4

Determination of the Resistance Curve

In this Chapter the effort made on acquiring the expression of resistance curve, including the introduction of test-setup and result analysis, is elaborated.

4.1 Introduction of the Test-setup

The aim of conducting resistance test is to provide data from which the expression of resistance curve of model hull could be determined. Besides, this test also provides required data that could be applied in the propeller open-water test (in Chapter 6 it will be discussed).

The conventional way of conducting model-scale resistance test is the towing tank test, whose detailed procedure could be found in ITTC Recommended Procedures & Guidelines and will not be repeated here. Yet some key points about model installation should be addressed:

- *The model should be positioned such that it is in the centreline of the tank.*
- *The tow force should, where possible, be applied in the line of centerplane and* ***at the*** *LCB.*
- *The model should be attached to the measuring head of the resistance dynamometer by a connection, which can transmit and measure only a horizontal tow force.*
- *Yawing and swaying of the model must be prevented without restraining any other direction of movement.*

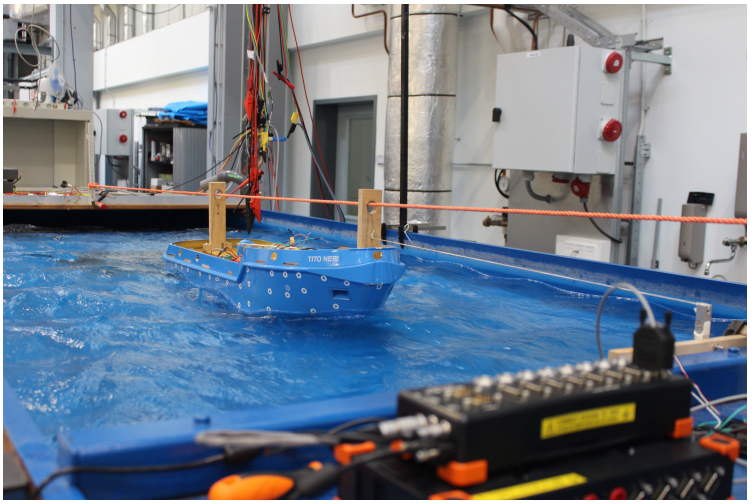

FIGURE 36: Setup of Resistance Test

Since the model boat "Tito Neri" is a complete model with all systems equipped, it has difficulty being mounted on the towing carrier. Therefore, another way (which is similar to the towing tank test) of conducting test needs to be found.

Fig 36 shows the test-setup: the test is conducted in the flume tank in 3ME Faculty. Unlike the traditional way through which the model hull is mounted on a carrier and sails in the towing tank, Tito Neri is connected to one load cell which is fixed on the edge of the flume tank through the white wire. By changing the speed of the generated water flow, the value of tension force (which is equal to the drag force) at different velocity will be measured by the load cell and transferred to DEWE-43A Board, then recorded by DEWE Software installed in the user's laptop.

As shown in Fig 36, the model boat is positioned in the centerline of flume tank in order to make sure that the effect of coming water flow is symmetrical, the white wire connected to the load cell is perfectly horizontal, **yet its extension line fails to go through the** LCB because the load cell cannot be placed in the water. Although there are no artificial trim effects in this test which indicates that its result is still trustful, this error becomes fatal in other tests and related information will be given in Chapter 6. The orange rope and wooden structure could prevent the model boat from yawing and swaying, while the vertical and longitudinal movements are free to occur.

The result of resistance test is given below:

TABLE 4.1: **Result of Resistance Test**

v_s	R_{ahead}	R_{astern}
$[m/s]$	$[N]$	$[N]$
0.19	0.2812	0.3265
0.26	0.5679	0.6632
0.32	0.9047	1.0124
0.39	1.3298	1.5829
0.45	1.8792	2.1911
0.52	2.4252	2.8894
0.58	3.2323	

As shown in Table 4.1, both ahead resistance and astern resistance were measured. When measuring the astern resistance at $0.58m/s$, there was a risk that the lateral movements could not be restrained anymore, so the measurement stopped at $0.52m/s$.

4.2 Result Analysis of the Resistance Test

Based on the test result given in Table 4.1, after entering the measured data into Microsoft Excel and plot the graph of resistance versus velocity, the resistance curve (ahead

and astern) looks like:

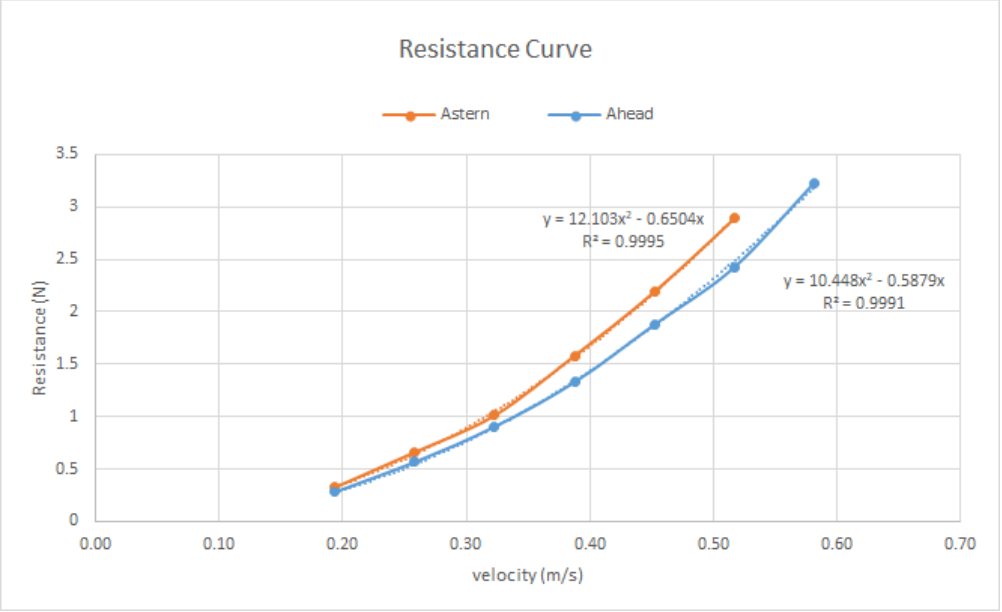

FIGURE 37: Resistance Curve of Tito Neri

After the graph shown in Fig 37 is created, by using the function "adding trend line" in Excel, the expression of resistance curve could be determined as follows:

For ahead resistance:

$$R_{ahead} = 10.448v_s^2 - 0.5879v_s \tag{4.1}$$

For astern resistance:

$$R_{astern} = 12.103v_s^2 - 0.6504v_s \tag{4.2}$$

The expressions shown in Fig 4.1, 4.2 are both parabolic polynomials and it fits the resistance law, which indicates that the result of resistance test should be reasonable. However, perhaps due to the error of load cell, the values of force measured under high velocities are not very accurate. More details will be given in next chapter.

Chapter 5

Discussion about Propeller Open-water Diagram

In this Chapter the main topic for discussion is determining the propeller open-water diagram. Like the tests elaborated in previous Chapters, the basic theory, test-setup, test result analysis and further discussions will be included.

5.1 Basic Theory of the Propeller Open-water Diagram

There are two different types of propeller open-water diagram: K_T, K_Q versus J type and the four-quadrant C_T^*, C_Q^* versus β type. The expression of β, C_T^*, C_Q^* is given below:

$$\begin{cases} \beta = \arctan(\dfrac{v_A}{0.7\pi \cdot n_p \cdot D}) \\ C_T^* = \dfrac{T}{\frac{1}{2} \cdot \rho \cdot (v_A^2 + (0.7\pi \cdot n_p \cdot D)^2) \frac{\pi}{4} \cdot D^2} \\ C_Q^* = \dfrac{Q}{\frac{1}{2} \cdot \rho \cdot (v_A^2 + (0.7\pi \cdot n_p \cdot D)^2) \frac{\pi}{4} \cdot D^3} \end{cases} \tag{5.1}$$

Compared with the $J - K_T, K_Q$ type, one significant advantage of the four-quadrant type is its continuity: when propeller rotating speed $n_p = 0$, the advanced ratio J will become infinite and the diagram will be discontinuous. The four-quadrant type, on the other hand, does not have this problem.

Both types of the open-water diagram mentioned above need to be acquired through propeller open-water tests. Here, the word "open-water" is applied to differ from the normal operating condition of propeller: the behind vessel condition. Under open-water condition, there is no interaction between hull and propeller, which means that the effect of wake field and thrust deduction (or resistance increasing) could be eliminated.

While conducting the open-water test, a wide enough range of J (or β) should be reached. In order to do so, there are two ways to conduct the test:

- Fix the value of advance velocity v_A while changing the value of propeller rotating speed n_p.
- Fix n_p while changing v_A.

Obviously, if bollard-pull condition (when $v_A = 0$) wants to be included, the first way given above should not be chosen because the fixed value of v_A cannot be 0. The second way, on the other hand, does not have this limitation. Therefore, the second way given above is the optimal choice for the test.

5.2 Introduction of the Test-setup

Traditionally, the propeller open-water test should be conducted either in the towing tank or inside the cavitation tunnel. However, just like the example of resistance test given in last Chapter, the situation of Tito Neri is special (the ducted propeller equipped on Tito Neri is too small) therefore its open-water test needs to be designed and conducted in a different way.

Before introducing the test-setup and procedure, some basic characteristics of the ducted propeller should be given:

TABLE 5.1: **Basic Characteristics of Tito Neri's Ducted Propeller**

Propeller diameter D_p (m)	0.065
Number of propeller blades Z_p	4
P/D ratio	1.4

Hardware of the setup and the connections between each other is shown below:

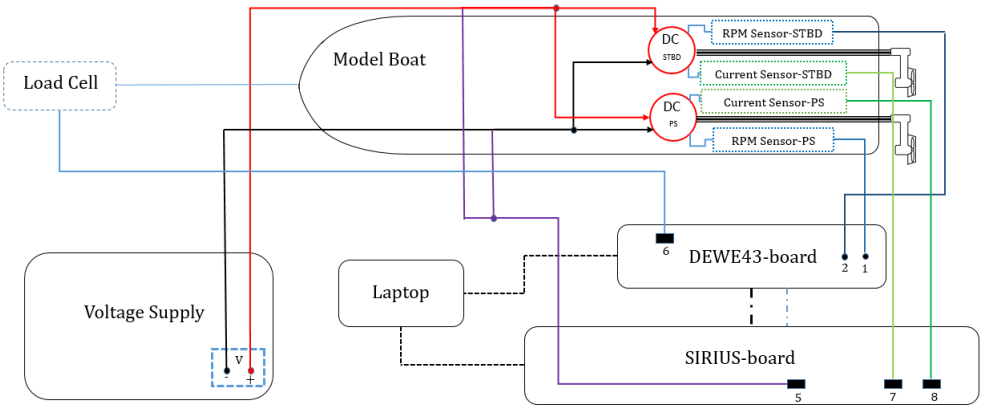

FIGURE 38: Schematic block diagram of open water test setup

The location to conduct this test is again the flume tank in 3ME Faculty. From Fig 38 it is acknowledged that the test is conducted by using the whole model boat. The DC motors are now driven by a voltage supply, and the corresponding shaft rotating speed, motor current as well as (part of) the thrust force will be measured and recorded.

The method to conduct the open-water test by using this setup is: fix the propeller rotating speed by giving the DC motor a constant voltage, meanwhile changing the propeller advance velocity by adjusting the water flow velocity so that different values of advanced ratio J (or C_T^*), which is equal to $\frac{v_A}{n_p \cdot D}$ could be acquired (including the bollard-pull condition when $J = 0$). Besides, in order to acquire enough data, different voltages (from $6V$ to $7.5V$) are given and the test is repeated under each voltage. However, there

is a price to do so: although by changing the pump power of flume tank, water flow with different velocity could be generated, which makes it possible to simulate the situation of towing tank, there is a big problem of conducting "open-water" test in this way: since the model hull is included, the interaction between propeller and the hull is also brought in, which makes the test environment not "open-water" any more. Therefore, extra attention should be made when analyzing the test result.

5.3 Result Analysis of the Open-water Test

As mentioned in the last paragraph of section 5.2, the interaction between propeller and the hull must be taken into account when analyzing the test result. Since the interaction is different for bollard condition and for other conditions (when v_A is not zero), it should be discussed individually:

For bollard-pull condition, the concepts of wake field is no more applicable because the advance velocity remains zero, and the interaction between propeller and the hull is only accounted for by thrust deduction.

For other conditions, both the effect of wake field (the water flow velocity which is equal to v_s should be multiplied by $1 - w$ to get v_A) and thrust deduction (the thrust force should be multiplied by $1 - t$ to balance with other forces) should be considered.

Besides, in order to acquire the four-quadrant open-water diagram, the test needs to be conducted in different conditions: the thrust force now is the result of superposition of tension force (the force measured by load cell) and wave force (which can be deducted from resistance curve), which differs from one quadrant to another.

Fig 39 to Fig 42 shows the force configuration of each quadrant:

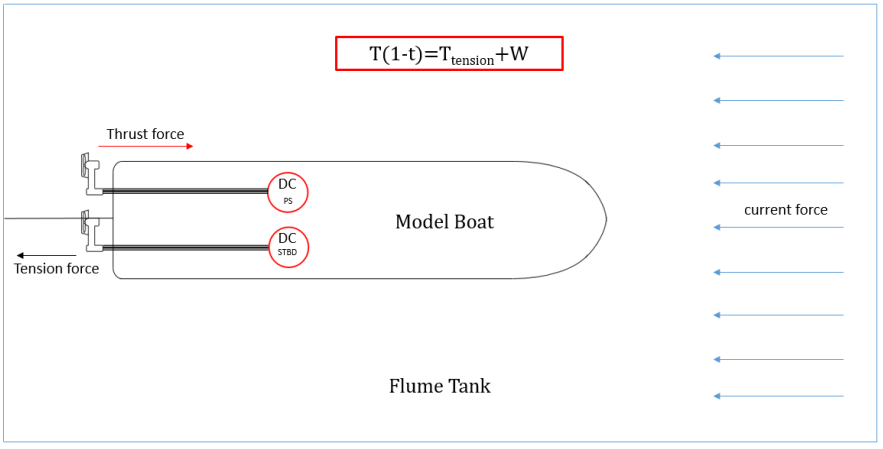

FIGURE 39: Force configuration of 1st Quadrant

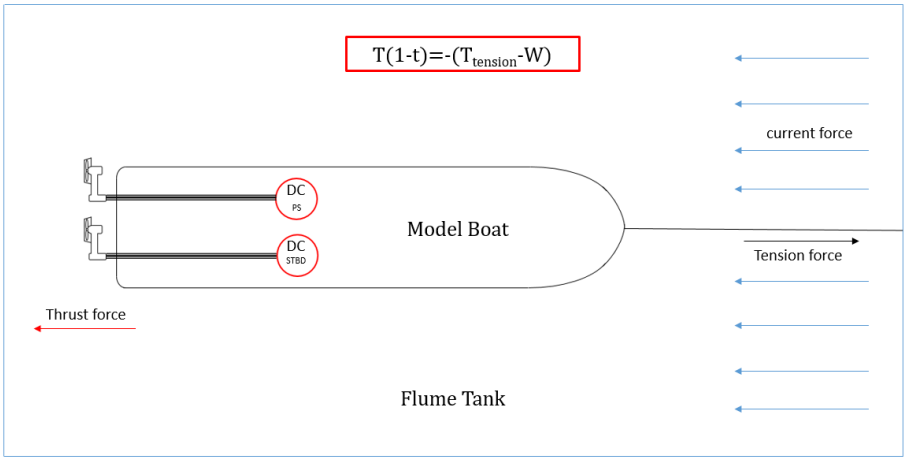

FIGURE 40: Force configuration of 2nd Quadrant

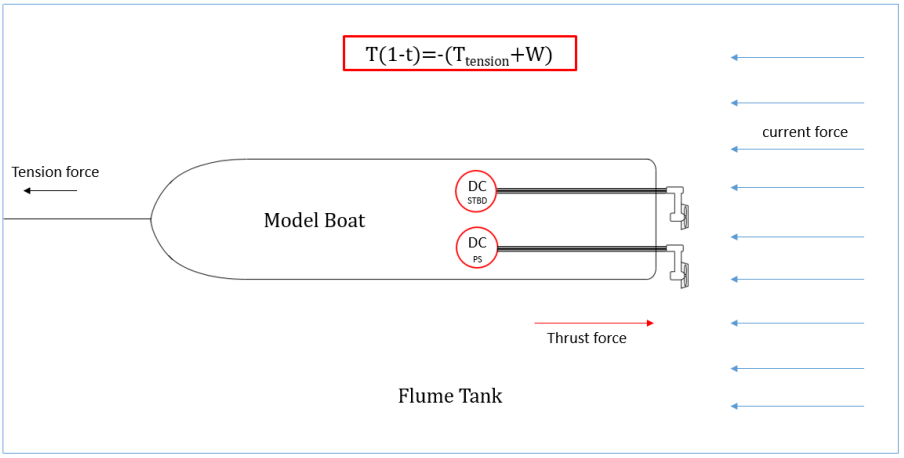

FIGURE 41: Force configuration of 3rd Quadrant

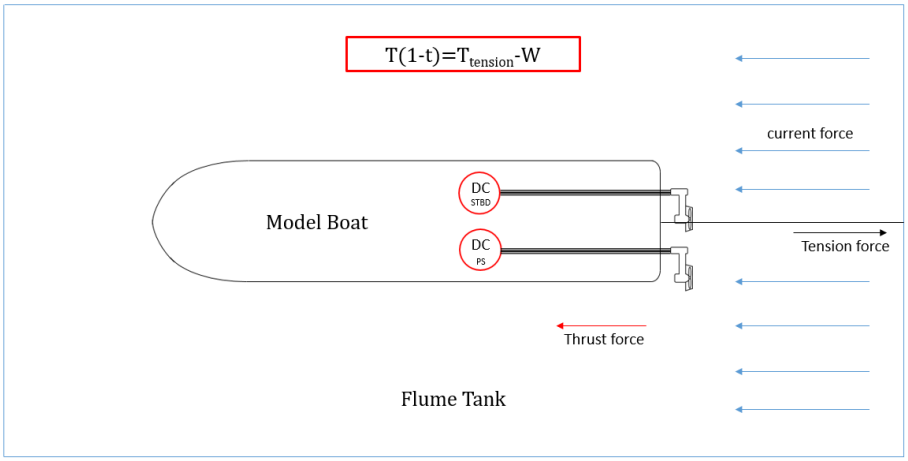

FIGURE 42: Force configuration of 4th Quadrant

Here the test data of the first-quadrant is given below as an example:

TABLE 5.2: Test Data of 6V

v_A	n_p(PS)	n_p(STBD)	I_{ps}	I_{stbd}	V_{ps}	V_{stbd}	T_{masure}	R	T
$[m/s]$	$[rps]$	$[rps]$	$[A]$	$[A]$	$[V]$	$[V]$	$[N]$	$[N]$	$[N]$
0.13	12.29	13.30	1.47	1.56	5.92	6.04	2.53	0.10	2.859
0.25	12.34	13.17	1.58	1.54	5.94	6.06	1.76	0.57	2.534
0.32	13.15	13.17	1.58	1.65	5.94	6.06	1.48	0.90	2.595
0.38	12.75	13.23	1.57	1.57	5.95	6.06	0.93	1.33	2.461

TABLE 5.3: Test Data of 6.5V

v_A	n_p(PS)	n_p(STBD)	I_{ps}	I_{stbd}	V_{ps}	V_{stbd}	T_{masure}	R	T
$[m/s]$	$[rps]$	$[rps]$	$[A]$	$[A]$	$[V]$	$[V]$	$[N]$	$[N]$	$[N]$
0.13	13.80	14.53	1.74	1.75	6.43	6.55	3.10	0.10	3.480
0.25	13.77	14.46	1.68	1.7	6.43	6.55	2.34	0.57	3.159
0.38	14.46	14.77	1.74	1.7	6.43	6.55	1.69	1.33	3.278
0.44	13.90	14.71	1.63	1.68	6.43	6.55	0.93	1.88	3.059

TABLE 5.4: Test Data of 7V

v_A	n_p(PS)	n_p(STBD)	I_{ps}	I_{stbd}	V_{ps}	V_{stbd}	T_{masure}	R	T
$[m/s]$	$[rps]$	$[rps]$	$[A]$	$[A]$	$[V]$	$[V]$	$[N]$	$[N]$	$[N]$
0.13	14.84	15.82	1.77	1.86	6.89	7.02	3.60	0.10	4.019
0.25	15.00	16.15	1.68	1.88	6.89	7.02	2.93	0.57	3.805
0.38	15.12	15.86	1.64	1.79	6.90	7.03	2.22	1.33	3.863
0.44	15.02	15.90	1.42	1.78	6.91	7.03	1.62	1.88	3.801
0.49	15.17	15.94	1.54	1.76	6.91	7.03	1.14	2.36	3.803

TABLE 5.5: Test Data of 7.5V

v_A	n_p(PS)	n_p(STBD)	I_{ps}	I_{stbd}	V_{ps}	V_{stbd}	T_{masure}	R	T
$[m/s]$	$[rps]$	$[rps]$	$[A]$	$[A]$	$[V]$	$[V]$	$[N]$	$[N]$	$[N]$
0.13	16.32	17.38	2	1.98	7.45	7.59	4.54	0.10	5.037
0.25	16.55	17.40	1.98	1.99	7.45	7.59	3.79	0.57	4.738
0.38	16.50	17.40	1.89	1.94	7.45	7.58	2.78	1.33	4.470
0.51	16.70	17.64	1.9	1.92	7.45	7.59	1.77	2.43	4.560
0.57	16.58	17.49	1.74	1.79	7.40	7.53	1.16	3.23	4.777

From the data shown in the above 4 tables, the open-water diagram could be determined as follows:

$$J = \frac{v_A}{n_p \cdot D} \tag{5.2}$$

$$K_T = \frac{T}{\rho \cdot n_p^2 \cdot D^4} \tag{5.3}$$

The determination of K_Q relies on determining the open-water propeller torque Q, under steady state, there is:

$$i_{gbt} \cdot i_{gbb} \cdot K_m i_{a,0} - i_{gbt} \cdot i_{gbb} \cdot M_{BF} - i_{gbb} \cdot M_{F1} - M_{F2} = Q \tag{5.4}$$

Then K_Q could be determined by:

$$K_Q = \frac{Q}{\rho \cdot D^5 \cdot (\frac{n_{E,0}}{i_{gbt} \cdot i_{gbb}})^2} \tag{5.5}$$

Based on the information given above, the test result is shown below:

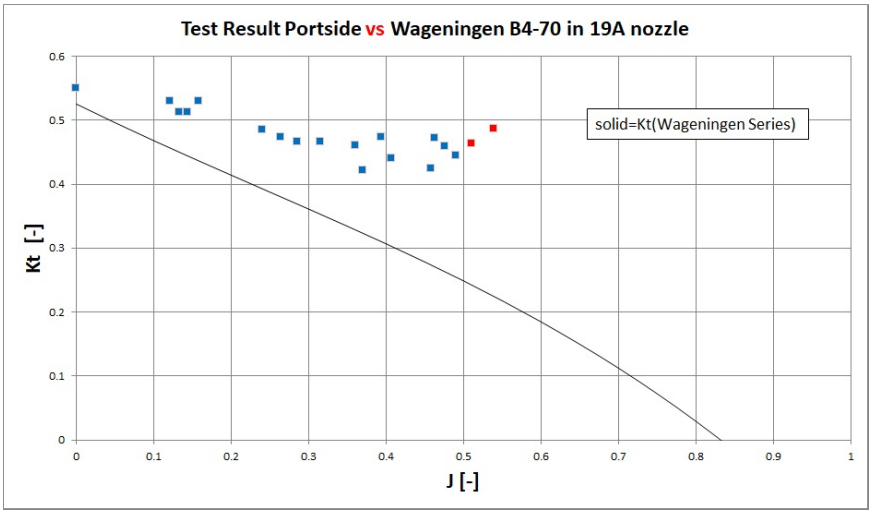

FIGURE 43: Result of Open-water Test K_T Portside

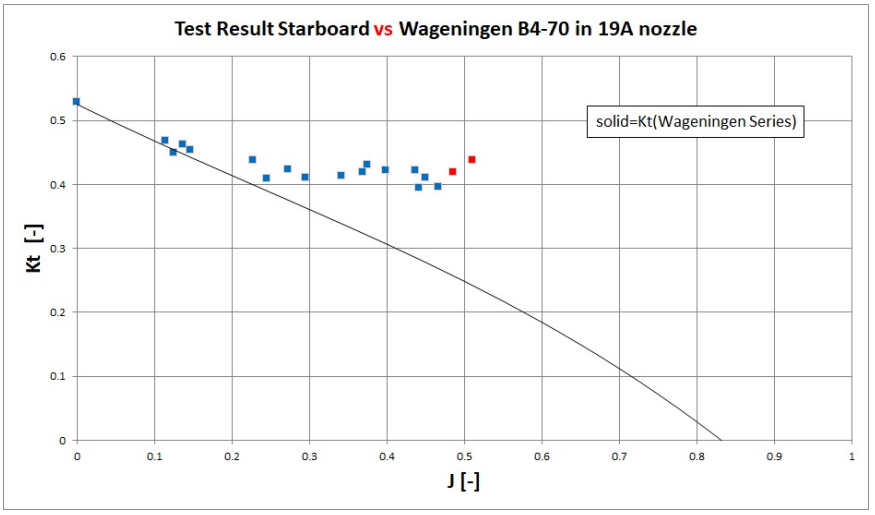

FIGURE 44: Result of Open-water Test K_T Starboard

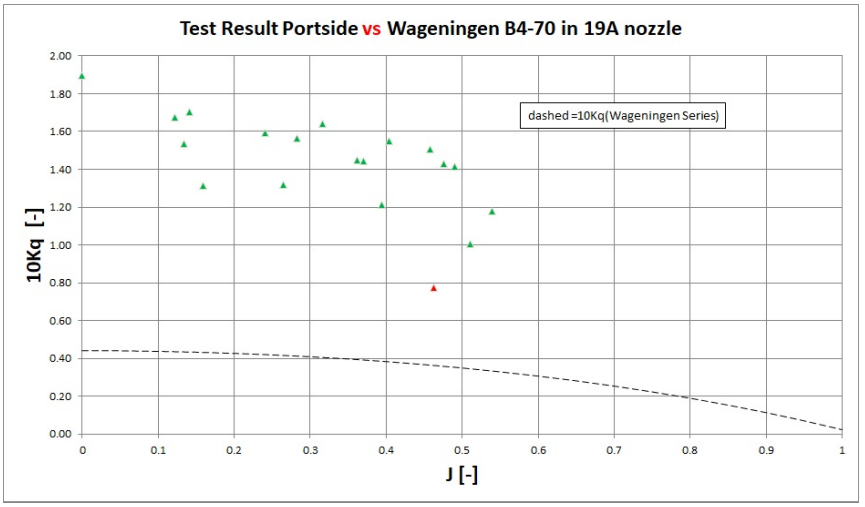

FIGURE 45: Result of Open-water Test $10K_Q$ Portside

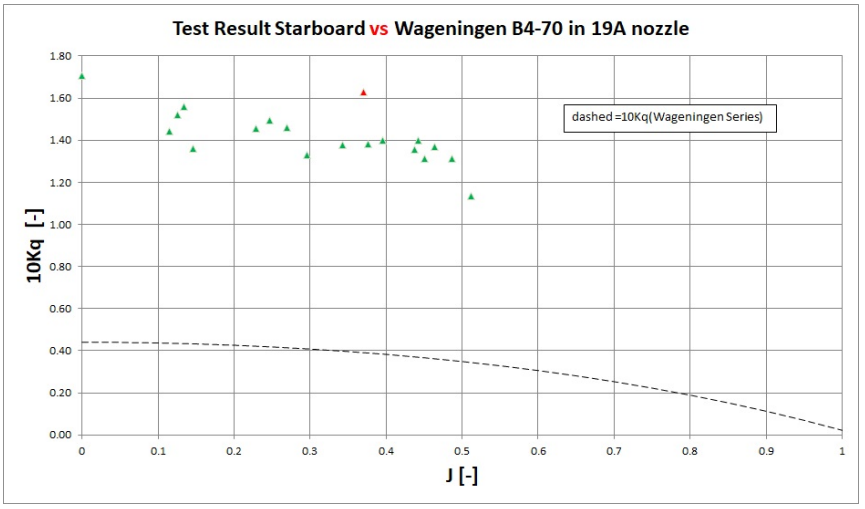

FIGURE 46: Result of Open-water Test $10K_Q$ Starboard

In Fig 43, 44, 45 and 46, the dots represent the test result. Obviously, it is impossible to derive the expression of $K_T, K_Q - J$ curves based on the given data dots and further discussions should be made in order to modify the result.

Firstly, from Fig 43 and Fig 44, it is acknowledged that the value of K_T becomes higher and higher than expected when J increases, especially from the two red dots in Fig 43 and Fig 44. To understand the behind reason, the variables contained by Eq 5.2 and Eq 5.3 are looked through here: since the density of fresh water ρ under 20°C (which is $0.9982063 g/cm^3$) and the diameter of propeller D are determined physical quantities, and the value of v_s, n_E are directly measured by corresponding sensors whose relationship with v_A, n_p is clear and simple, thrust force T becomes the most questionable variable that may lead to the weird circumstance shown in Fig 43 and Fig 44.

According to the expression given in Fig 39, the value of T is determined by the sum of drag force W, which is equal to resistance R, and tension force $T_{tension}$ along the wire, which is measured by load cell. Since the expression of R is also derived from the data measured by load cell during resistance test (recall section 4.2), the reliability of load cell has vital importance on determining the value of T. Unfortunately, the author failed to realize this point until another test (in which the steering force of different angles were measured by the same load cell) was conducted. During that test, the sensitivity of load cell, which should maintain constant, was found to be unstable and need to be calibrated roughly every two minutes. In resistance test and open-water test, however, it was calibrated every 10 minutes or even every 30 minutes depending on the test procedure. Therefore, according to the procedure, there is a great possibility that the force measured under high velocities in resistance test (as mentioned in the last paragraph of section 4.2), and the tension force $T_{tension}$ measured under high advanced ratio J in open-water test, are not reliable. All these factors will lead to error in determining the value of thrust force T, and finally will lead to inaccuracy of K_T.

After examining the relationship of $K_T - J$ shown in Fig 43 and Fig 44, now Fig 45 and 46 which present the relationship of $K_Q - J$ should be looked through. The dashed line in Fig 45 and 46 is the $10K_Q - J$ curve of $K_a4 - 70$ propeller in $19A$ duct (with $P/D = 1.0$). It is chosen as the reference curve due to the geometrical similarity between $K_a4 - 70$ propeller in $19A$ duct and the ducted propeller of Tito Neri. Apparently, the green dots are almost three times higher than the dashed line, which indicates the value of open-water torque Q determined by Eq 5.4 is larger than expected. One possible reason is: the value of K_m, M_{BF}, M_{F1} and M_{F2} applied in Eq 5.4 were determined by dry-run tests. Now the propulsion system is operating under water, which has no influence on K_m, M_{BF}, M_{F1}. M_{F2}, however, must be affected since water is expected to go inside the shaft cover and viscous friction will be changed. Therefore, the actual value of M_{F2} under wet condition should be lower than the value determined under dry condition, which will result in increasing value of K_Q.

However, since the value of M_{F2} is almost small enough to be neglected, even if it may be inaccurate, the key factor leading "error" in K_Q should not be the inaccuracy of M_{F2}. Except the reason given above, Fig 47 indicates that the open-water efficiency η_o of Tito Neri's ducted propeller is relatively low compared with $K_a4 - 70$ propeller in $19A$ duct. And after measuring the geometrical dimensions, it was discovered that the P/D value at $0.7R$ of Tito Neri's propeller is 1.4 (given in Table 5.1), which is different from the reference propeller ($K_a4 - 70$ propeller in $19A$ duct with $P/D = 1.0$). This information suggests that the chosen reference propeller may not be a proper representative of the ducted propeller of Tito Neri, although the $K_T - J$ relationship of them seems to be similar with each other.

Besides the reasons mentioned above, the odd red dot in Fig 45, which is obviously lower than expected, may indicate another key factor leading errors in determining the value of open-water torque Q when using Eq 5.4: by checking the corresponding experimental data in Table 5.4, it is observed that the value of **measured electrical current** I_{ps} (the red $1.42A$) is definitely smaller than expected (the value should be around $1.6A$ according to other data), which results in a lower value of Q and ultimately a lower value of K_Q. Therefore, when Eq 5.4 is applied to determine Q, the measured value of electrical current I will play an important role. Unfortunately, as mentioned in section 3.4.2, the measurement data could sometimes be deceived by the instability of current sensor, and this must be modified in the future.

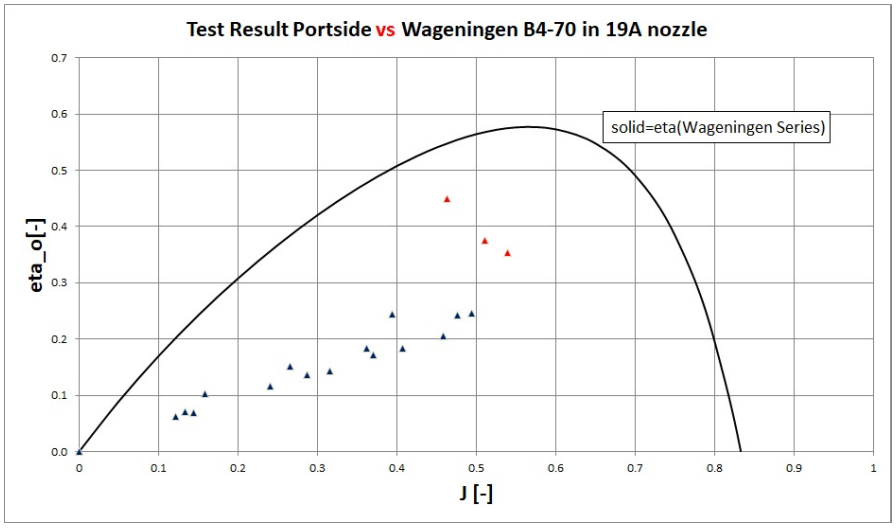

FIGURE 47: Result of Open-water Test η_o Portside

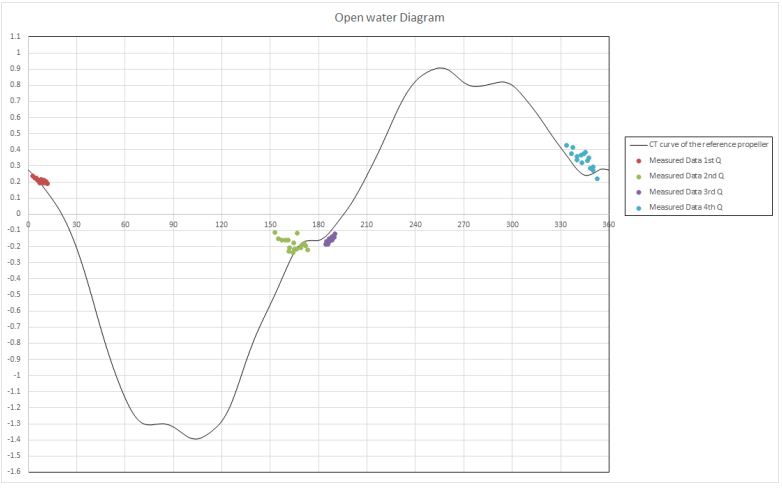

FIGURE 48: Result of Open-water Test C_T^* Starboard

Since effort has been made on acquiring the four-quadrant open-water diagram, despite the result is not valid enough, it is still given in Fig 48. Obviously, the range of C_T^*

is very limited by using the current test-setup and in the future more effort should be made on modifying it for sure.

5.4 Validation of K_T, K_Q value under bollard-pull condition

Since the expression of $K_T, K_Q - J$ curves could not be derived, and the expression of resistance curve now becomes questionable, it is impossible to build the simulation model of the propulsion system operating under straight-line sailing condition. However, according to the description given in last section, the K_T value of bollard-pull condition should be reasonable: when conducting bollard-pull test, the load cell was just calibrated and there was less interaction between hull & propeller compared with normal condition. The K_Q value, on the other hand, may not be so accurate due to the difference of M_{F2} between dry and wet condition, yet since M_{F2} does not play an important role in determining the value of K_Q, the result acquired so far is at least acceptable. Therefore, the simulation model of the propulsion system operating under bollard-pull condition is built and validated.

5.4.1 The simulation model of Tito Neri's Propulsion System of Bollard-pull Condition

Compared with the simulation model of dry-run condition, K_T and K_Q are added to the simulation model of propulsion chain, which is shown in Fig 49. And in Fig 50, the result comparison of tension force is included.

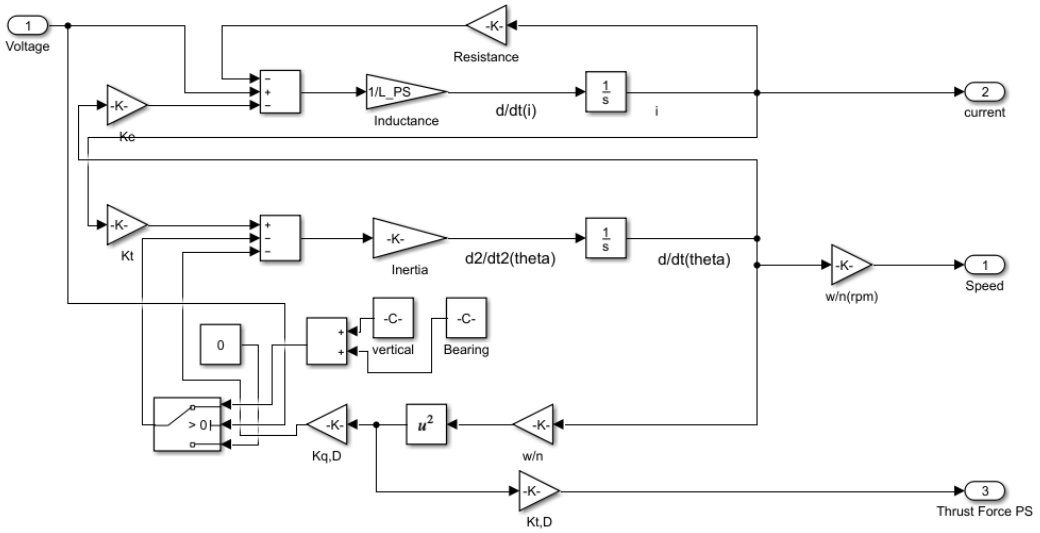

FIGURE 49: Simulation Model of Single Shaft-line

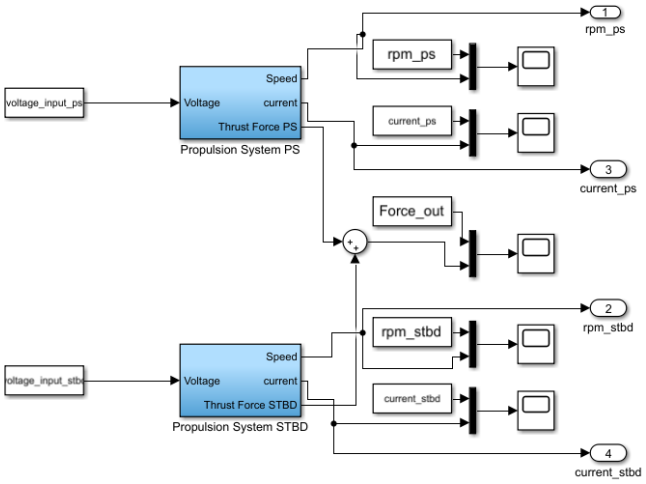

FIGURE 50: Simulation Model of Tito Neri's Propulsion Sytem under Bollard-pull Condition

5.4.2 Validation of the Simulation Model

Method to validate the simulation model is the same as before: by comparing its behavior with measured data of real tests. Here the input voltage signal is sinusoidal with a frequency of $0.01Hz$, which is shown in Fig 51, and the result comparison is given in Fig 52 to 56.

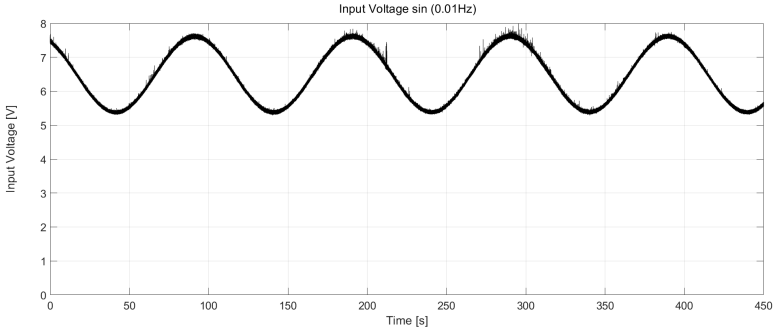

FIGURE 51: Input Voltage Signal $0.01Hz$ under Bollard-pull Condition

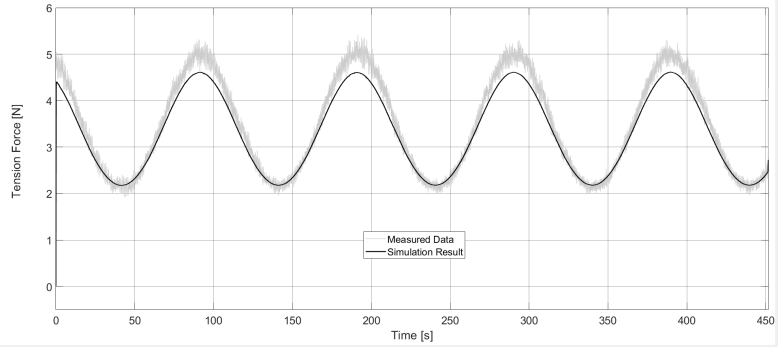

FIGURE 52: Comparison of Tension Force under Bollard-pull Condition

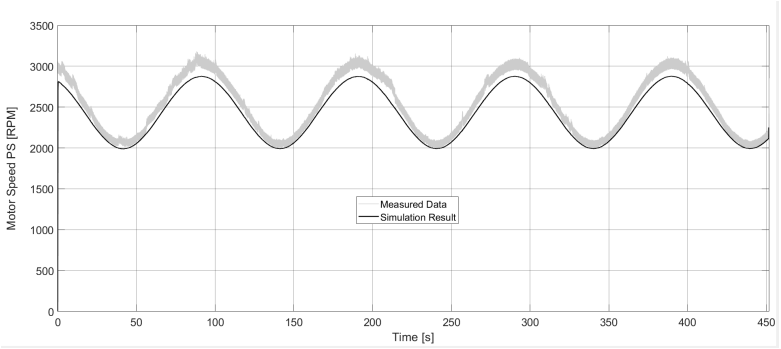

FIGURE 53: Comparison of motor speed PS under Bollard-pull Condition

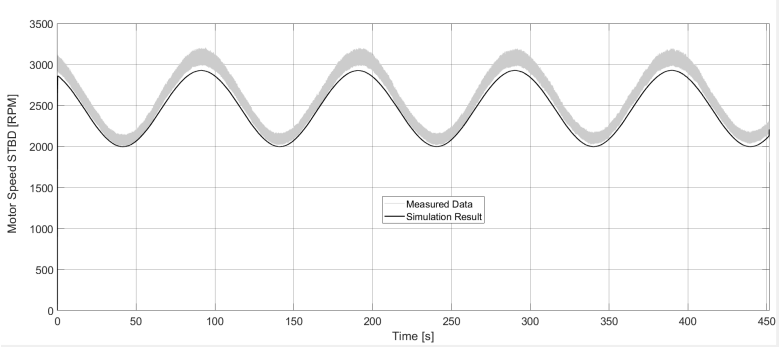

FIGURE 54: Comparison of motor speed STBD under Bollard-pull Condition

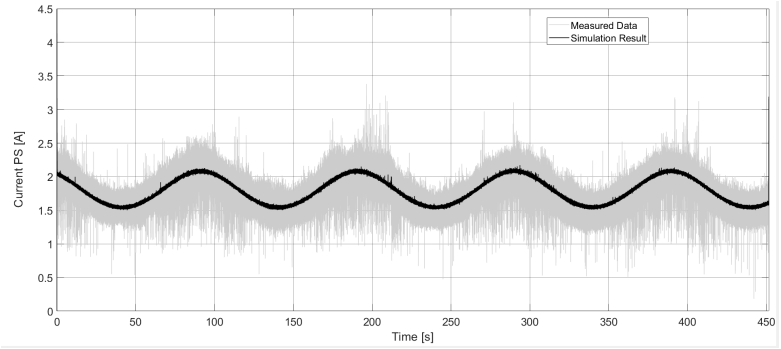

FIGURE 55: Comparison of current PS under Bollard-pull Condition

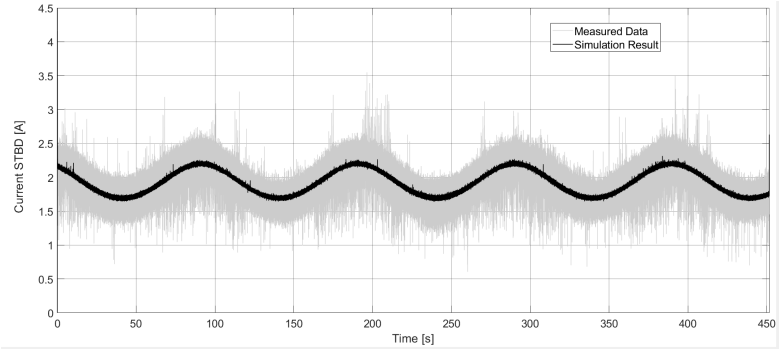

FIGURE 56: Comparison of current STBD under Bollard-pull Condition

From Fig 52, 53 and 54, it is acknowledged that except peak value, the simulation result and the measured data of tension force, and of motor speed match very well. Fig 55 and Fig 56 indicate that the comparison of current is almost perfect despite the measured data is extremely noisy.

The value of K_T *and* K_Q *under bollard-pull condition for each shaft-line is:* $K_T|_{PS} = 0.55, K_T|_{STBD} = 0.53, K_Q|_{PS} = 0.1898, K_Q|_{STBD} = 0.1704$.

To make the validity of this simulation model more convincing and complete, in Appendix D, the result comparison of block input signal is given.

Chapter 6

Linearization of Tito Neri's Propulsion Sytem

As is all known, compared with non-linear model, there are some favorable properties of linear model, such as simpleness and transparency, that makes it being widely used in the field of control engineering. The mathematical model derived in Chapter 2, however, like other models of ship propulsion system, is non-linear. Therefore, in this Chapter, firstly, a linearized ship propulsion system model raised by D.Stapersma and A.Vrijdag [2] is going to be introduced and the method of linearization will be elaborated. After that, some variations about the linearized model will be discussed to make it more complete. Then, based on all the information, the mathematical model of Tito Neri's propulsion system will be linearized (also as an extension of [2]), and its behavior under bollard-pull condition will be validated.

6.1 Introduction of the Original Linearized Model

Compared with non-linear models, linearized models often have simpler structures and require less detailed parameters to derive. Yet behind these advantages, there is indeed an expensive price to use linearized models: due to the principle of linearization, they are only valid around equilibrium point or specially set-point. Therefore, *the linearized ship propulsion model should not be seen as the replacement for a non-linear model, but rather as an additional tool that can be used. The main reason to derive this linearized model is that linear models can be used to predict system behaviour (such as the behavior in waves) in the frequency domain, besides, this model is also applicable for initial controller design and tuning*[2].

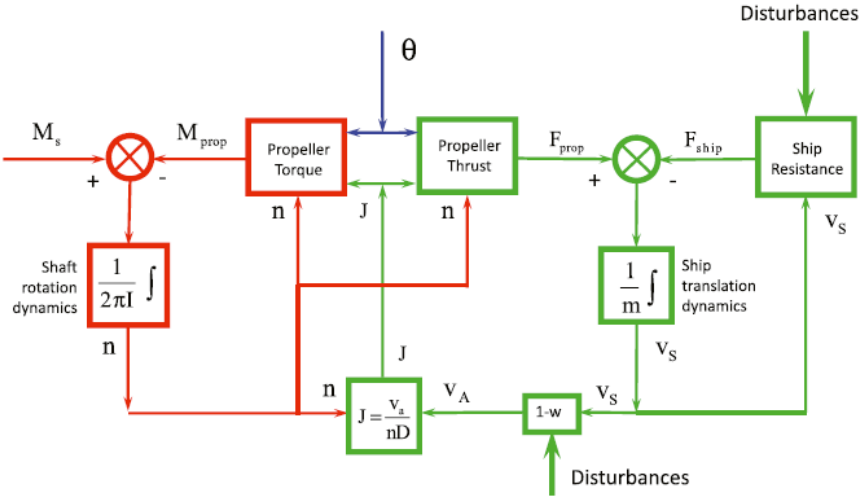

FIGURE 57: General Ship propulsion block diagram [2]

A ship propulsion system, as mentioned in Chapter 2, consists of two loops which is connected by the operation of propeller.

On the left side it shows the shaft rotation loop, whose behavior could be determined by Eq 6.1:

$$\boldsymbol{2\pi \cdot I_p \cdot \frac{dn}{dt} = M_S - M_{prop}} \tag{6.1}$$

On the right side the ship translation loop is given, whose behavior could be determined by Eq 6.2:

$$\boldsymbol{m_{ship} \cdot \frac{dv_s}{dt} = F_{prop} - F_{ship}} \tag{6.2}$$

Obviously, due to multiplicative action in the mathematical model, for instance ship resistance $R = \alpha \cdot v_s^e$, and the curvature in the characteristics of component models, like the curvature of K_T and K_Q curves, the ship propulsion system shown in Fig 57 is non-linear. In 2016, D.Stapersma raised up a method regarding with normalization and linearization (Appendix. B in [2]), and the author of this Thesis gives an extended version of this method in the coming sub-section.

6.1.1 Linearization & Normalization Method

Assuming a variable Z is the product of powers of other variables:

$$Z = c \cdot Y_1^{e_1} \cdot Y_2^{e_2} \cdot Y_n^{e_n} = c \cdot \prod_{i=1}^{n} Y_i^{e_i} \tag{6.3}$$

Where c is a constant multiplier and e_i is a constant exponent. In an equilibrium point the variable equals to:

$$Z_0 = c \cdot \prod_{i=1}^{n} Y_{i,0}^{e_i} \tag{6.4}$$

After normalization, it results in:

$$\frac{Z}{Z_0} = \prod_{i=1}^{n} (\frac{Y_i}{Y_{i,0}})^{e_i} \tag{6.5}$$

Near equilibrium point small increments δZ, δY_i can be introduced as:

$$\begin{cases} Z = Z_0 + \delta Z \\ Y_i = Y_{i,0} + \delta Y_i \end{cases} \tag{6.6}$$

Substituting Eq 6.6 into Eq 6.5, it will give:

$$\frac{Z_0 + \delta Z}{Z_0} = \prod_{i=1}^{n} (\frac{Y_{i,0} + \delta Y_i}{Y_{i,0}})^{e_i} \tag{6.7}$$

Eq 6.7 could be transformed to:

$$\frac{\delta Z}{Z_0} = \prod_{i=1}^{n} (1 + \frac{\delta Y_i}{Y_{i,0}})^{e_i} - 1 \tag{6.8}$$

After Taylor series expansion and ignoring second as well as higher order terms, Eq 6.8 will become:

$$\begin{aligned} \frac{\delta Z}{Z_0} &= \prod_{i=1}^{n} [1 + e_i \cdot \frac{\delta Y_i}{Y_{i,0}} + \frac{e_i \cdot (e_i - 1)}{2} (\frac{\delta Y_i}{Y_{i,0}})^2 + \cdots] - 1 \\ &\approx 1 + \sum_{i=1}^{n} e_i \cdot \frac{\delta Y_i}{Y_{i,0}} - 1 \\ &= \sum_{i=1}^{n} e_i \cdot \frac{\delta Y_i}{Y_{i,0}} \end{aligned} \tag{6.9}$$

And if by definition,

$$\delta Z^* = \frac{\delta Z}{Z_0} \tag{6.10}$$

Eq 6.3 could be transformed to:

$$\boldsymbol{\delta Z^* = \sum_{i=1}^{n} e_i \cdot \delta Y_i^*} \tag{6.11}$$

The derivation above indicates that after normalization and linearization, the multiplication of variables Y_i could be transformed to a format of summation, and the exponents e_i change to become constant multiplication factors.

6.1.2 Linearization of Shaft Rotation and Ship Translation Loop

6.1.2.1 Linearization of Shaft Rotation Loop

By applying the same procedure shown in section 6.1.1 to Eq 2.3, which describes the behavior of *shaft rotation loop*:

$$\frac{2\pi \cdot I_p}{M_{S,0}} \cdot \frac{n_0}{n_0} \cdot \frac{dn}{dt} = \frac{M_S}{M_{S,0}} - \frac{M_{prop}}{M_{S,0}} \tag{6.12}$$

Since in a steady nominal condition the shaft and propeller torque are equal (when friction is neglected), therefore:

$$M_{S,0} = M_{prop,0}$$

And around equilibrium point:

$$\begin{cases} M_S = M_{S,0} + \delta M_S \\ M_{prop} = M_{prop,0} + \delta M_{prop} \end{cases}$$

Now Eq 6.12 becomes:

$$\frac{2\pi \cdot I_p}{M_{S,0}} \cdot \frac{n_0}{n_0} \cdot \frac{dn}{dt} = \frac{M_{S,0} + \delta M_S}{M_{S,0}} - \frac{M_{prop,0} + \delta M_{prop}}{M_{prop,0}} \tag{6.13}$$

If defining the *integration constant of shaft system* as:

$$\tau_n \equiv \frac{2\pi \cdot I_p \cdot n_0}{M_{S,0}} \tag{6.14}$$

Eq 6.13 now becomes:

$$\tau_n \cdot \frac{dn^*}{dt} = \delta M_S^* - \delta M_{prop}^* \tag{6.15}$$

Since the relation between engine torque M_b and shaft torque M_S is [20]:

$$M_S = i_r \cdot k_e \cdot \eta_{GB} \cdot M_b$$

i_r is gear-box reduction ratio and k_e is number of engines. If gear-box efficiency η_{GB} is assumed to be constant then there is:

$$\delta M_S^* = \delta M_b^* \tag{6.16}$$

And if the change of relative rotative efficiency is neglected, there is:

$$\delta M_{prop}^* = \delta Q^* \tag{6.17}$$

Substituting Eq 6.16 and Eq 6.17 into Eq 6.15:

$$\tau_n \cdot \frac{dn^*}{dt} = \delta M_b^* - \delta Q^* \tag{6.18}$$

Open water torque Q is equal to:

$$Q = \rho \cdot D^5 \cdot n^2 \cdot K_Q$$

And if water density ρ is assumed to be constant, after normalizing, there is:

$$\delta Q^* = 2 \cdot \delta n^* + \cdot \delta K_Q^*$$

To be specific, K_Q is a function of both advance ratio J and propeller pitch angle θ, therefore:

$$\delta K_Q^* = b \cdot \delta J^* + q \cdot \delta \theta^* \tag{6.19}$$

In which:

$$\begin{cases} b \equiv (\frac{J_0}{K_{Q,0}}) \cdot (\frac{\delta K_Q}{\delta J})|_\theta \\ q \equiv (\frac{\theta_0}{K_{Q,0}}) \cdot (\frac{\delta K_Q}{\delta \theta})|_J \end{cases}$$

And since $J = \frac{v_s \cdot (1-w)}{n \cdot D}$, after normalization:

$$\delta J^* = \delta v_s^* - \delta w^* - \delta n^* \tag{6.20}$$

Substituting Eq 6.20 into Eq 6.19, there is:

$$\delta K_Q^* = b \cdot (\delta v_s^* - \delta w^* - \delta n^*) + q \cdot \delta\theta^* \tag{6.21}$$

Finally, after substituting Eq 6.21 into Eq 6.18, the differential equation of *shaft rotation loop* is given as:

$$\boldsymbol{\tau_n \cdot \frac{dn^*}{dt} = \delta M_b^* - (2-b) \cdot \delta n^* - b \cdot \delta v_s^* + b \cdot \delta w^* - q \cdot \delta\theta^*} \tag{6.22}$$

6.1.2.2 Linearization of Ship Translation Loop

While in *ship translation loop*, after applying normalization procedure to Eq 2.4, there is:

$$\frac{m_{ship} \cdot v_{s,0}}{F_{prop,0}} \cdot \frac{dv_s}{v_{s,0} \cdot dt} = \frac{F_{prop}}{F_{prop,0}} - \frac{F_{ship}}{F_{prop,0}} \tag{6.23}$$

Around equilibrium point,

$$\begin{cases} F_{prop} = F_{prop,0} + \delta F_{prop} \\ F_{ship} = F_{ship,0} + \delta F_{ship} \end{cases}$$

And in steady conditions, there is:

$$F_{prop,0} = F_{ship,0}$$

If define *integrator constant of ship translation* τ_v as:

$$\tau_v \equiv \frac{m_{ship} \cdot v_{s,0}}{F_{prop,0}}$$

Then Eq 6.23 could be transformed to:

$$\tau_v \cdot \frac{dv_s}{v_{s,0} \cdot dt} = \frac{F_{prop,0} + \delta F_{prop}}{F_{prop,0}} - \frac{F_{ship,0} + \delta F_{ship}}{F_{prop,0}} \tag{6.24}$$

By definition, Eq 6.24 is equal to:

$$\tau_v \cdot \frac{dv_s^*}{dt} = \delta F_{prop}^* - \delta F_{ship}^* \tag{6.25}$$

Since ship force could be replaced by resistance, there is:

$$\delta F_{ship}^* = \delta R^*$$

And ship resistance could be presented as:

$$R = \alpha \cdot v_s^e$$

Therefore, after normalization, there is:

$$\delta R^* = \delta \alpha^* + e \cdot \delta v_s^* \tag{6.26}$$

Where

$$e \equiv \frac{v_{s,0}}{R_0} \cdot \frac{\delta R}{\delta v_s} | \alpha$$

As for propeller force, since it is equal to thrust force, there is:

$$\delta F_{prop}^* = \delta T^*$$

And the expression of thrust force T is:

$$T = \rho \cdot D^4 \cdot n^2 \cdot K_T$$

After normalization, there is:

$$\delta T^* = 2 \cdot \delta n^* + \delta K_T^* \tag{6.27}$$

Just like K_Q, K_T is also a function of J and θ, so:

$$\delta K_T^* = a \cdot \delta J^* + p \cdot \delta \theta^* \tag{6.28}$$

In which the normalized propeller derivatives a and p are:

$$\begin{cases} a \equiv (\frac{J_0}{K_{T,0}}) \cdot (\frac{\delta K_T}{\delta J})|_\theta \\ p \equiv (\frac{\theta_0}{K_{T,0}}) \cdot (\frac{\delta K_T}{\delta \theta})|_J \end{cases}$$

By substituting Eq 6.20 into Eq 6.28, there is:

$$\delta K_T^* = a \cdot (\delta v_s^* - \delta w^* - \delta n^*) + p \cdot \delta \theta^* \tag{6.29}$$

Now if substitute Eq 6.29 into Eq 6.27, there is:

$$\delta T^* = (2 - a) \cdot \delta n^* + a \cdot \delta v_s^* - a \cdot \delta w^* + p \cdot \delta \theta^* \tag{6.30}$$

Finally, if Eq 6.26 and 6.30 are substituted into Eq 6.25, the linearized differential equation for *ship translation loop* is:

$$\boldsymbol{\tau_v \cdot \frac{d v_s^*}{dt} = (2 - a) \cdot \delta n^* - (e - a) \cdot \delta v_s^* - \delta \alpha^* - a \cdot \delta w^* + p \cdot \delta \theta^*} \tag{6.31}$$

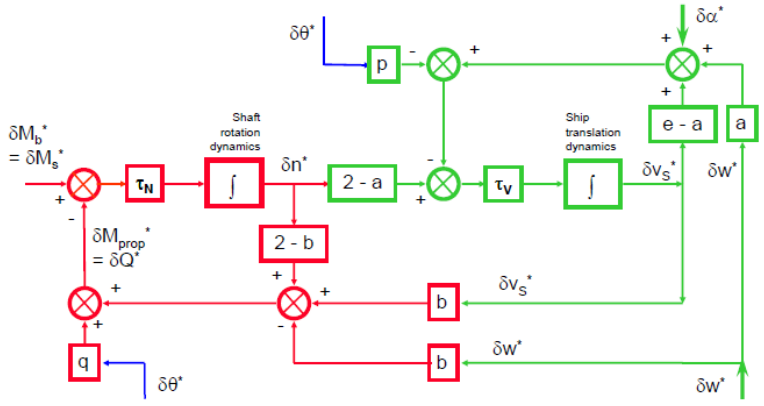

FIGURE 58: Linearized block diagram of core propulsion system [2]

***Summary of 6.1.2**

After normalization and linearization, the block diagram of core propulsion system now could be transformed from Fig 57 to Fig 58. And Eq 6.1, 6.2 are linearized to Eq 6.22, 6.31. In Eq 6.22 and 6.31, τ_n and τ_v are constants according to their definition, a, b, p, q and e are variables (at equilibrium point they are constants) whose definition are given

in the content above. $\delta\theta^*$ and δM_b^* are inputs of this system which could be controlled while δv_s^* and δn^* are state variables. The other two parameters, $\delta\omega^*$ and $\delta\alpha^*$ reflect the environmental disturbances.

According to D.Stapersma and A.Vrijdag [2], *the model derived above provides a solid framework for further work aiming at understanding and improving dynamic behaviour of ship propulsion plants, especially sailing in waves. The linearised model can also be used to determine initial settings of controller parameters, which can subsequently be tested in a nonlinear model.* In the paper it is also mentioned that some variations and extensions will be given in the future. The following content could provide an example.

6.2 Related Variations

In previous section the method of linearization & normalization as well as the theoretical linearized model is introduced. Apparently, this model could represent the operating condition of a vessel equipped with CPP(s) under straight-line sailing condition. In other words, this specific model does not cover all types of propulsion system (like FPP) and does not take all the operating situations into consideration, for instance bollard-pull condition. Therefore, some variations will be addressed in this section.

6.2.1 Discussion about Bollard-pull Condition

Firstly, the variation about bollard-pull condition (with CPP propulsion system) will be discussed. For *shaft rotation loop* the situation is same as straight-line sailing condition, and the equation is same as Eq 2.3, from 2.1.2.1 it is acknowledged that after normalization, Eq 2.3 could be transformed to Eq 6.18:

$$\tau_n \cdot \frac{dn^*}{dt} = \delta M_b^* - \delta Q^*$$

Here is a significant difference between bollard-pull condition and straight line sailing condition:

Under bollard-pull condition, the openwater propeller torque Q is equal to:

$$Q = \boldsymbol{K_{Q,0}} \cdot \rho \cdot D^5 \cdot n^2$$

While under free sailing condition, the torque Q is equal to:

$$Q = \boldsymbol{K_Q} \cdot \rho \cdot D^5 \cdot n^2$$

The difference is: $\boldsymbol{K_{Q,0}}$ is constant because under bollard-pull condition the torque coefficient does not change, while $\boldsymbol{K_Q}$, under free sailing condition, is a variable related with J and θ.

Therefore, under bollard-pull condition, after normalization, openwater torque Q becomes:

$$\delta Q^* = 2 \cdot \delta n^*$$

Then the differential equation of *shaft loop under bollard-pull condition* is:

$$\boldsymbol{\tau_n \cdot \frac{dn^*}{dt} = \delta M_b^* - 2 \cdot \delta n^*} \tag{6.32}$$

Since under bollard-pull condition ship speed maintains to be zero, the basic equation of *ship translation loop* is:

$$0 = F_{prop} - F_T$$

F_R is the tension force along the rope which is used to fix the position of ship. Around equilibrium point, there is:

$$\begin{cases} F_{prop} = F_{prop,0} + \delta F_{prop} \\ F_T = F_{T,0} + \delta F_T \end{cases}$$

And in a steady condition, there is:

$$F_{prop,0} = F_{T,0} \tag{6.33}$$

If F_R is replaced by thrust force T, after normalization and substitution, the linearized equation of Eq 6.33 is:

$$\boldsymbol{0 = 2 \cdot \delta n^* - \delta F_T^*} \tag{6.34}$$

6.2.2 Linearization of FPP Equipped Propulsion System

Another variation will discuss changes in the linearized model when CPP is substituted by FPP. The reason why this variation should be addressed is: the MT218 model boat has two nozzled azimuth thrusters, which could be treated as FPPs. And the following discussion will be separated into straight-line sailing condition and bollard-pull condition.

Under straight line sailing condition, the basic equations of shaft loop and ship translation loop will not change when CPP is substituted by FPP. So Eq 2.3 is still able to describe the behavior of shaft loop. And after linearization and normalization procedures shown in 6.1.1, Eq 2.3 will be transformed to Eq 6.18, also from section 6.1.2 it is acknowledged that:

$$\delta Q^* = 2 \cdot \delta n^* + \delta K_Q^*$$

Because of the substitution from CPP to FPP, now the open-water torque coefficient K_Q is only a function of advanced ratio J. Therefore:

$$\delta K_Q^* = b \cdot \delta J^* \tag{6.35}$$

In which:

$$b \stackrel{\equiv}{} (\frac{J_0}{K_{Q,0}}) \cdot (\frac{\delta K_Q}{\delta J})$$

The normalization of advanced ratio J is presented in Eq 6.20, after substituting Eq 6.20 into Eq 6.35, there is:

$$\delta K_Q^* = b \cdot (\delta v_s^* - \delta \omega^* - \delta n^*) \tag{6.36}$$

The final version of *shaft rotation loop differential equation* is:

$$\boldsymbol{\tau_n \cdot \frac{dn^*}{dt} = \delta M_b^* - (2 - b) \cdot \delta n^* - b \cdot \delta v_s^* + b \cdot \delta w^*} \tag{6.37}$$

As for *ship translation loop*, the procedure of linearization and normalization will not be repeated, below is the final version of differential equation:

$$\boldsymbol{\tau_v \cdot \frac{dv_s^*}{dt} = (2-a)\cdot \delta n^* - (e-a)\cdot \delta v_s^* - \delta \alpha^* - a \cdot \delta w^*} \tag{6.38}$$

Under **bollard-pull condition**, since the situation (including basic equations for both loops and the linearization procedures) has no difference when CPP is replaced by FPP, Eq 6.32 and 6.34 could be directly adapted to describe the linearized behavior of shaft rotation and thrust force.

*Summary of Linearized Equations, Constants & Variables

In this part all the linearized equations under different circumstances, as well as the related constants and variables are summarized.

Obviously when equations shown in Table 6.1 are derived, the effect of transmission system and friction torque has not been taken into account. The reason is: the transmission system together with the friction model differs from one propulsion system to another, therefore it is impossible to give an overall presentation. In next chapter, a case study about the propulsion system of Tito Neri will provide an example of how to deal with their effects when linearization is applied.

TABLE 6.1: **Linearized Equations under different circumstances**

	Straight-line sailing condition	**Bollard-pull condition**
CPP	Eq 6.22 and Eq 6.31	Eq 6.32 and Eq 6.34
FPP	Eq 6.37 and Eq 6.38	Eq 6.32 and Eq 6.34

TABLE 6.2: **Expressions of mentioned constants&variables**

Constants & Variables	**Expression**
$\boldsymbol{\tau_n}$	$2 \cdot \pi \cdot I_p \cdot n_0 / M_{S,0}$
$\boldsymbol{\tau_v}$	$m_{ship} * v_{s,0} / F_{prop,0}$
$\boldsymbol{a}$	$(\frac{J_0}{K_{T,0}}) \cdot (\frac{\delta K_T}{\delta J})\|_\theta$
$\boldsymbol{b}$	$(\frac{J_0}{K_{Q,0}}) \cdot (\frac{\delta K_Q}{\delta J})\|_\theta$
$\boldsymbol{e}$	$\frac{v_{s,0}}{R_0} \cdot \frac{\delta R}{\delta v_s}\|\alpha$
$\boldsymbol{p}$	$(\frac{\theta_0}{K_{T,0}}) \cdot (\frac{\delta K_T}{\delta \theta})\|_J$
$\boldsymbol{q}$	$(\frac{\theta_0}{K_{Q,0}}) \cdot (\frac{\delta K_Q}{\delta \theta})\|_J$

6.3 Linearization of Tito Neri's Propulsion System

Since the open-water diagram acquired in Chapter 5 is not valid enough to be applied, it is impossible to build and validate the linearized model under straight-line sailing

condition. Therefore, coming discussions will only focus on bollard-pull condition.

Based on the discussion given above and in section 2.1.2, the mathematical model of Tito Neri's propulsion system under bollard-pull condition contains three differential equations: Eq 2.11, Eq 2.12 and Eq 6.33. Each of them will be linearized individually.

6.3.1 Linearization of Electrical Circuit (Eq 2.11)

Around equilibrium point, there is:

$$L \cdot \frac{di_a}{dt} = (v_{a,0} + \delta v_a) - R \cdot (i_{a,0} + \delta i_a) - K_b \cdot (\omega_{E,0} + \delta\omega_E) \tag{6.39}$$

And in steady state, there is:

$$0 = v_{a,0} - R \cdot i_{a,0} - K_b \cdot \omega_{E,0} \tag{6.40}$$

Subtracting Eq 6.40 from Eq 6.39, there is:

$$L \cdot \frac{di_a}{dt} = \delta v_a - R \cdot \delta i_a - K_b \cdot \delta\omega_E \tag{6.41}$$

Divide both sides with nominal voltage supply minus back EMF voltage $v_{a,0} - K_b \cdot \omega_{E,0}$, Eq 6.41 could be transformed to:

$$\frac{L}{v_{a,0} - K_b \cdot \omega_{E,0}} \cdot \frac{di_a}{dt} = \frac{\delta v_a}{v_{a,0} - K_b \cdot \omega_{E,0}} - \frac{R \cdot \delta i_a}{v_{a,0} - K_b \cdot \omega_{E,0}} - \frac{K_b \cdot \delta\omega_E}{v_{a,0} - K_b \cdot \omega_{E,0}} \tag{6.42}$$

And from Eq 6.40 it is acknowledged that $v_{a,0} - K_b \cdot \omega_{E,0} = R \cdot i_{a,0}$, therefore:

$$\frac{L}{R \cdot i_{a,0}} \cdot \frac{di_a}{dt} = \frac{\delta v_a}{v_{a,0} - K_b \cdot \omega_{E,0}} - \frac{R \cdot \delta i_a}{R \cdot i_{a,0}} - \frac{K_b \cdot \omega_{E,0}}{v_{a,0} - K_b \cdot \omega_{E,0}} \cdot \frac{\delta\omega_E}{\omega_{E,0}} \tag{6.43}$$

And if *electrical constant* is defined as $\tau_e \equiv \frac{L}{R}$, Eq 6.43 could be transformed to:

$$\tau_e \cdot \frac{di_a^*}{dt} = \delta v_a^* - \delta i_a^* - \frac{K_b \cdot \omega_{E,0}}{v_{a,0} - K_b \cdot \omega_{E,0}} \cdot \delta\omega_E^* \tag{6.44}$$

Since $\omega_E = 2 \cdot \pi \cdot n_E$, the final version of differential equation is:

$$\boldsymbol{\tau_e \cdot \frac{di_a^*}{dt} = \delta v_a^* - \delta i_a^* - \frac{2 \cdot \pi \cdot K_b \cdot n_{E,0}}{v_{a,0} - 2 \cdot \pi \cdot K_b \cdot n_{E,0}} \cdot \delta n_E^*} \tag{6.45}$$

Keep notice that here:

$$\delta v_a^* = \frac{\delta v_a}{v_{a,0} - K_b \cdot \omega_{E,0}}$$

6.3.2 Linearization of Shaft Rotation Loop (Eq 2.12)

If defining:

$$I_P = I_{P1} + \frac{I_{P2}}{i_{gbt}^2} + \frac{I_{P3}}{i_{gbt}^2 \cdot i_{gbb}^2}$$

Together with the relation $\omega_E = 2 \cdot \pi \cdot n_E$, under bollard-pull condition, Eq 2.12 could be rewritten as:

$$2 \cdot \pi \cdot I_P \cdot \frac{dn_E}{dt} = K_m \cdot i_a - M_{BF} - \frac{M_{F1}}{i_{gbt}} - \frac{M_{F2}}{i_{gbt} \cdot i_{gbb}} - \frac{K_{Q,0} \cdot \rho \cdot D^5 \cdot (\frac{n_E}{i_{gbt} \cdot i_{gbb}})^2}{i_{gbt} \cdot i_{gbb}} \tag{6.46}$$

And around equilibrium point there is:

$$2 \cdot \pi \cdot I_P \cdot \frac{dn_E}{dt} = K_m(i_{a,0} + \delta i_a) - M_{BF} - \frac{M_{F1}}{i_{gbt}} - \frac{M_{F2}}{i_{gbt} \cdot i_{gbb}} - \frac{K_{Q,0} \cdot \rho \cdot D^5 \cdot (n_{E,0} + \delta n_E)^2}{i_{gbt}^3 \cdot i_{gbb}^3} \tag{6.47}$$

In steady state:

$$0 = K_m i_{a,0} - M_{BF} - \frac{M_{F1}}{i_{gbt}} - \frac{M_{F2}}{i_{gbt} \cdot i_{gbb}} - \frac{K_{Q,0} \cdot \rho \cdot D^5 \cdot n_{E,0}^2}{i_{gbt}^3 \cdot i_{gbb}^3} \tag{6.48}$$

Subtracting Eq 6.48 from Eq 6.47 (according to Chapter 3, it is acknowledged that all friction torques are assumed to be constant), there is:

$$2 \cdot \pi \cdot I_P \cdot \frac{dn_E}{dt} = K_m \cdot \delta i_a - \frac{K_{Q,0} \cdot \rho \cdot D^5 \cdot (2 \cdot n_{E,0} \cdot \delta n_E + \delta n_E^2)}{i_{gbt}^3 \cdot i_{gbb}^3} \tag{6.49}$$

The second order term δn_E^2 could be neglected, and divide both sides with $K_m i_{a,0} - M_F$, which is equal to $K_{Q,0} \cdot \rho \cdot D^5 \cdot n_{E,0}^2/(i_{gbt}^3 \cdot i_{gbb}^3)$, and M_F is defined as:

$$M_F = M_{BF} + \frac{M_{F1}}{i_{gbt}} + \frac{M_{F2}}{i_{gbt} \cdot i_{gbb}}$$

Eq 6.49 could be transformed to:

$$\frac{2 \cdot \pi \cdot I_P \cdot n_{E,0}}{K_m i_{a,0} - M_F} \cdot \frac{dn_E}{n_{E,0} \cdot dt} = \frac{K_m \cdot i_{a,0}}{K_m \cdot i_{a,0} - M_F} \cdot \frac{\delta i_a}{i_{a,0}} - \frac{2 \cdot K_{Q,0} \cdot \rho \cdot D^5 \cdot n_{E,0} \cdot \delta n_E}{K_{Q,0} \cdot \rho \cdot D^5 \cdot n_{E,0}^2} \quad (6.50)$$

And if *mechanical constant* is defined as $\tau_m \equiv \frac{2 \cdot \pi \cdot I_P \cdot n_{E,0}}{K_m i_{a,0} - M_F}$, after fraction and reduction, the differential equation of **shaft rotation loop** is:

$$\boldsymbol{\tau_m \cdot \frac{dn_E^*}{dt} = \frac{K_m \cdot i_{a,0}}{K_m \cdot i_{a,0} - M_F} \cdot \delta i_a^* - 2 \cdot \delta n_E^*} \quad (6.51)$$

6.3.3 Linearization of Eq 6.33

Under **bollard-pull condition**, there is:

$$F_T = K_{Q,0} \cdot D^4 \rho n_E^2|_{[PS]} + K_{Q,0} \cdot D^4 \rho n_E^2|_{[STBD]} \quad (6.52)$$

Around equilibrium point, there is:

$$F_{T,0} + \delta F_T = K_{Q,0} \cdot D^4 \rho \cdot (n_{E,0} + \delta n_E)^2|_{[PS]} + K_{Q,0} \cdot D^4 \rho \cdot (n_{E,0} + \delta n_E)^2|_{[STBD]} \quad (6.53)$$

In steady state:

$$F_{T,0} = K_{Q,0} \cdot D^4 \rho n_{E,0}^2|_{[PS]} + K_{Q,0} \cdot D^4 \rho n_{E,0}^2|_{[STBD]} \quad (6.54)$$

After subtracting Eq 6.54 from Eq 6.53 and ignoring high order terms, there is:

$$\delta F_T = 2 \cdot K_{Q,0} \cdot D^4 \rho \cdot n_{E,0} \delta n_E|_{[PS]} + 2 \cdot K_{Q,0} \cdot D^4 \rho \cdot n_{E,0} \delta n_E|_{[STBD]} \quad (6.55)$$

From Chapter 3 to Chapter 5, it is acknowledged that the characteristics, such as $n_{E,0}$ & $K_{Q,0}$, of Portside and Starboard are different. Here, in order to simplify the normalization procedure, and also because the difference is very little, they are assumed to be equal. Therefore, if divide both sides with $2 \cdot K_{Q,0} \cdot D^4 \rho \cdot n_{E,0}^2$ (which is equal to $F_{T,0}$), Eq 6.55 could be transformed to:

$$\frac{\delta F_T}{2 \cdot K_{Q,0} \cdot D^4 \rho \cdot n_{E,0}^2} = \frac{4 \cdot K_{Q,0} \cdot D^4 \rho \cdot n_{E,0} \delta n_E}{2 \cdot K_{Q,0} \cdot D^4 \rho \cdot n_{E,0}^2} \tag{6.56}$$

After fraction, the linearized form of Eq 2.13 is:

$$\boldsymbol{\delta F_T^* = 2 \cdot \delta n^*} \tag{6.57}$$

6.4 Validation of the Linearized Model under Bollard-pull Condition

Now if δn_E^* ,δi_a^* and δF_R^* are considered as outputs, δv_a^* is treated as the input, based on Eq 6.45, 6.51 and 6.57, the Laplace Transfer Functions are given below (the derivation procedures are given in Appendix F):

$$\frac{\delta N_E^*}{\delta V_a^*} = \frac{K_m \cdot R \cdot i_{a,0}^2}{H \cdot \tau_e \cdot \tau_m \cdot s^2 + H \cdot (2\tau_e + \tau_m) \cdot s + 2 \cdot H + 2\pi K_m^2 \cdot i_{a,0} \cdot n_{E,0}} \tag{6.58}$$

$$\frac{\delta I_a^*}{\delta V_a^*} = \frac{2 \cdot H + H \cdot \tau_m \cdot s}{H \cdot \tau_e \cdot \tau_m \cdot s^2 + H \cdot (2\tau_e + \tau_m) \cdot s + 2 \cdot H + 2\pi K_m^2 \cdot i_{a,0} \cdot n_{E,0}} \tag{6.59}$$

$$\frac{\delta F_T^*}{\delta V_a^*} = \frac{2K_m \cdot R \cdot i_{a,0}^2}{H \cdot \tau_e \cdot \tau_m \cdot s^2 + H \cdot (2\tau_e + \tau_m) \cdot s + 2 \cdot H + 2\pi K_m^2 \cdot i_{a,0} \cdot n_{E,0}} \tag{6.60}$$

In which $H = K_m \cdot R \cdot i_{a,0}^2 - M_F \cdot R \cdot i_{a,0}$.

As mentioned before, the linearized model is valid within a limited region, such as a region around equilibrium point. In this Thesis, the equilibrium point (or steady state) at when a constant voltage of 6.5 volts is added to the system under bollard-pull condition is selected for analysis.

After applying the values given in Table 6.3, based on Eq 6.58, 6.59 and Eq 6.60, the related Bode Plot could be created. And in order to validate the linearized model which

TABLE 6.3: **Constants & Variables at operating point under Bollard-pull Condition**

Constants & Variables at Test-point	Value	Unit
$\boldsymbol{v_{a,0}}$	6.5	$[V]$
$\boldsymbol{i_{a,0(PS)}}$	1.86	$[A]$
$\boldsymbol{i_{a,0(SB)}}$	1.97	$[A]$
$\boldsymbol{I_{P(PS)}}$	2.017×10^{-5}	$[kg \cdot m^2]$
$\boldsymbol{I_{P(SB)}}$	1.997×10^{-5}	$[kg \cdot m^2]$
$\boldsymbol{n_{E,0(PS)}}$	42.7	$[rps]$
$\boldsymbol{n_{E,0(SB)}}$	44.1	$[rps]$
$\boldsymbol{M_{F(PS)}}$	0.01887	$[N \cdot m]$
$\boldsymbol{M_{F(SB)}}$	0.02287	$[N \cdot m]$
$\boldsymbol{R_{(PS)}}$	1.0418	$[\Omega]$
$\boldsymbol{R_{(SB)}}$	0.8923	$[\Omega]$
$\boldsymbol{K_{m(PS)}}$	0.0181	$[N \cdot m/A]$
$\boldsymbol{K_{m(SB)}}$	0.0183	$[N \cdot m/A]$
$\boldsymbol{\tau_{e(PS)}}$	0.0007	[-]
$\boldsymbol{\tau_{e(SB)}}$	0.0006	[-]
$\boldsymbol{\tau_{m(PS)}}$	0.3658	[-]
$\boldsymbol{\tau_{m(SB)}}$	0.4197	[-]

is presented by those three first-order differential equations, the following input voltage signal v_a has been added to the propulsion system:

$$v_a = v_{a,0} + A \cdot sin(Bt + C) \tag{6.61}$$

Eq 6.61 indicates that the input voltage v_a is a superposition of two different terms.

One is the nominal term $v_{a,0}$ (in this case $v_{a,0} = 6.5V$) and the other is sinusoidal term $A \cdot sin(Bt+C)$. To fulfill the condition of normalization, the amplitude A must be small enough compared to $v_{a,0}$. An example of input voltage signal is shown in Fig 59:

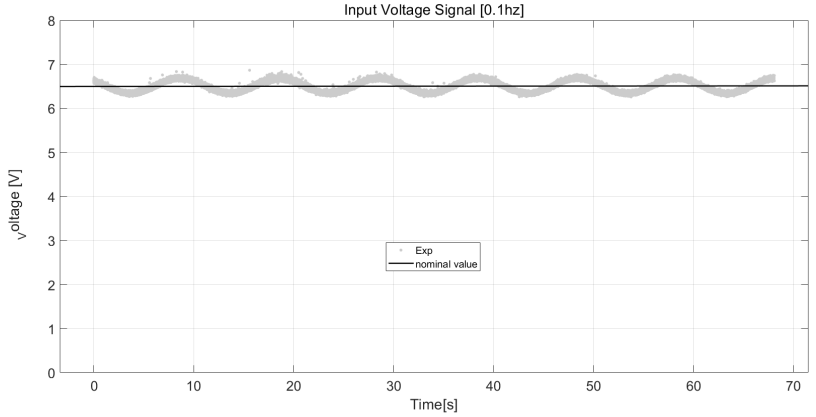

FIGURE 59: Input Voltage Signal at 0.1Hz

And when this type of input voltage is added, the response of propulsion system is shown below:

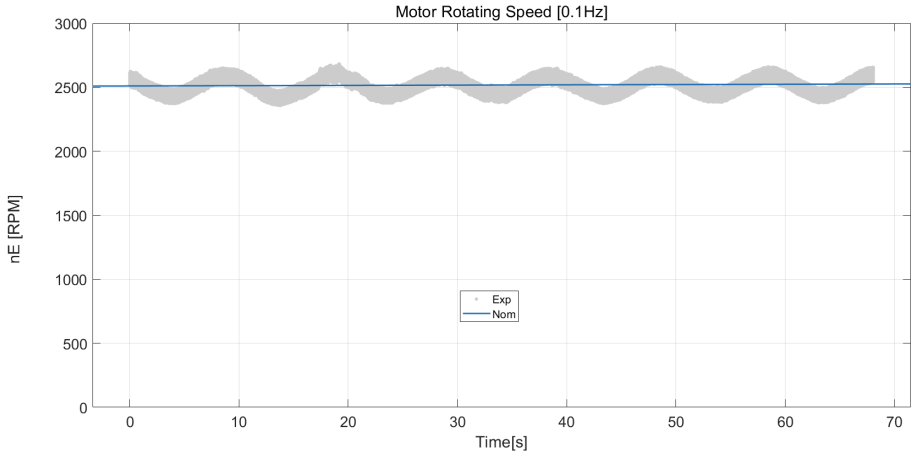

FIGURE 60: Motor Speed at 0.1Hz

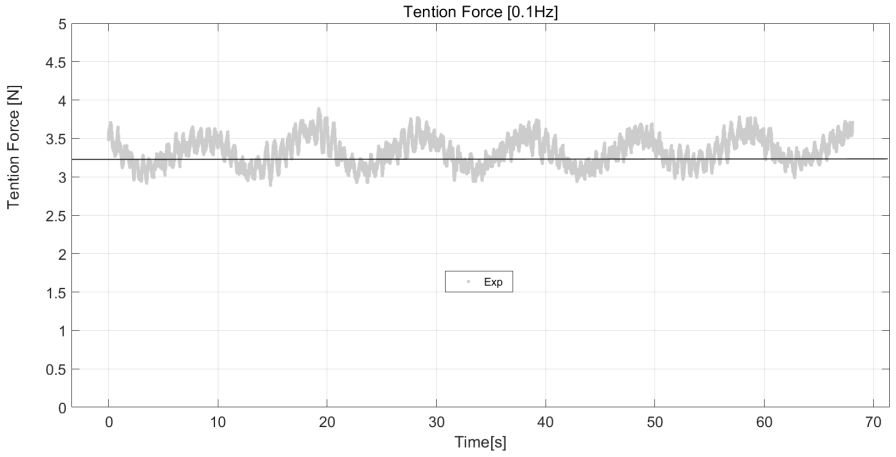

FIGURE 61: Tension Force at 0.1Hz

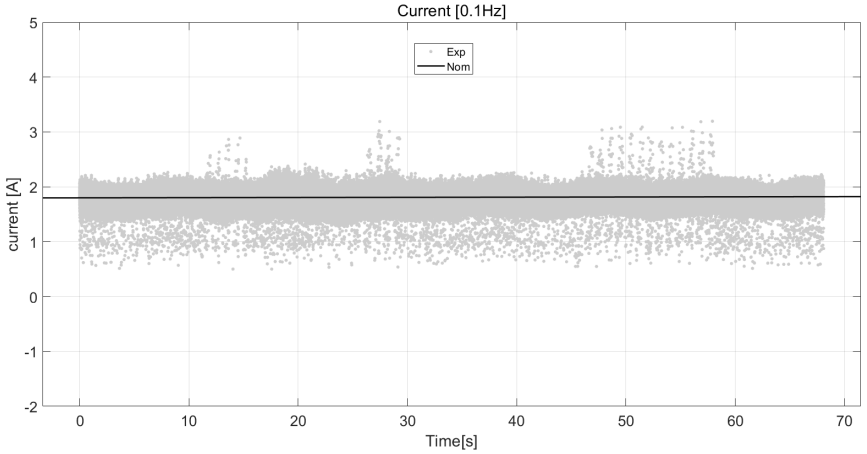

FIGURE 62: Current at 0.1Hz

Based on Fig 60 to Fig 62, it is acknowledged that the expression of system response n_E, i_a and F_T could be derived as:

$$n_E = n_{E,0} + A_1 \cdot sin(Bt + C_1) \tag{6.62}$$

$$F_T = F_{T,0} + A_2 \cdot sin(Bt + C_2) \tag{6.63}$$

$$i_a = i_{a,0} + A_3 \cdot sin(Bt + C_3) \tag{6.64}$$

Please be aware that despite the experimental data of current shown in Fig 62 is extremely noisy, by using least-square method, the fitted curve could be perfectly described by Eq 6.64.

In order to compare experimental data with the Bode Plot of the former linearized model, the data must be normalized. After normalization, Eq 6.61 to Eq 6.64 will become:

$$\delta v_a^* = \frac{\delta v_a}{v_{a,0} - 2\pi \cdot K_m \cdot n_{E,0}} = \frac{v_a - v_{a,0}}{v_{a,0} - 2\pi \cdot K_m \cdot n_{E,0}} = \frac{A \cdot sin(Bt + C)}{v_{a,0} - 2\pi \cdot K_m \cdot n_{E,0}} \tag{6.65}$$

$$\delta n_E^* = \frac{A_1 \cdot sin(Bt + C_1)}{n_{E,0}} \tag{6.66}$$

$$\delta F_T^* = \frac{A_2 \cdot sin(Bt + C_2)}{F_{T,0}} \tag{6.67}$$

$$\delta i_a^* = \frac{A_3 \cdot sin(Bt + C_3)}{i_{a,0}} \tag{6.68}$$

Based on the normalized variables, the corresponding points of experimental data (under specific frequency) which could be added to the Bode Plot are determined by (in Appendix E another form is given):

$$\begin{cases} \frac{\delta n_E^*}{\delta v_a^*}|_{Gain} = 20 \cdot \log(\frac{A_1}{A} \cdot \frac{v_{a,0} - 2\pi \cdot K_m \cdot n_{E,0}}{n_{E,0}}) \\ \frac{\delta n_E^*}{\delta v_a^*}|_{Phase} = C_1 - C \end{cases} \tag{6.69}$$

$$\begin{cases} \dfrac{\delta F_T^*}{\delta v_a^*}|_{Gain} = 20 \cdot \log(\dfrac{A_2}{A} \cdot \dfrac{v_{a,0} - 2\pi \cdot K_m \cdot n_{E,0}}{F_{T,0}}) \\ \dfrac{\delta F_T^*}{\delta v_a^*}|_{Phase} = C_2 - C \end{cases} \tag{6.70}$$

$$\begin{cases} \dfrac{\delta i_a^*}{\delta v_a^*}|_{Gain} = 20 \cdot \log(\dfrac{A_3}{A} \cdot \dfrac{v_{a,0} - 2\pi \cdot K_m \cdot n_{E,0}}{i_{a,0}}) \\ \dfrac{\delta i_a^*}{\delta v_a^*}|_{Phase} = C_3 - C \end{cases} \tag{6.71}$$

The method given above is a reasonable way of transferring experimental data to corresponding points of Bode Plot. Besides, the expressions given in Eq 6.65 to Eq 6.68 are determined by curve fitting and more details are given in Appendix E. By analyzing the experimental data of different frequency, the result comparison is shown below:

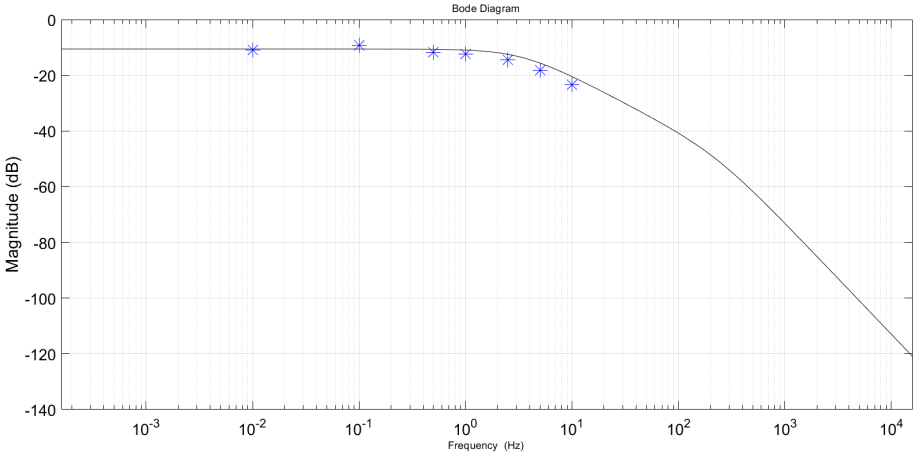

FIGURE 63: Magnitude Diagram of $\frac{\delta n_E^*}{\delta v_a^*}|_{PS}$

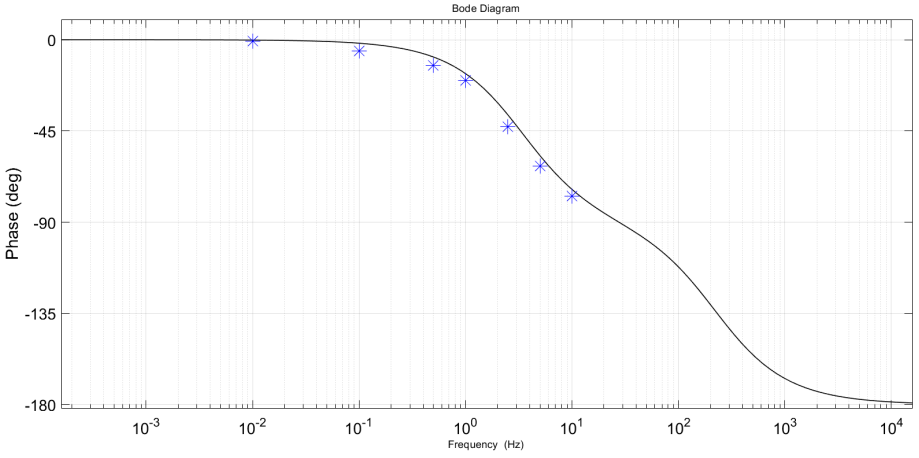

FIGURE 64: Phase Diagram of $\frac{\delta n_E^*}{\delta v_a^*}|_{PS}$

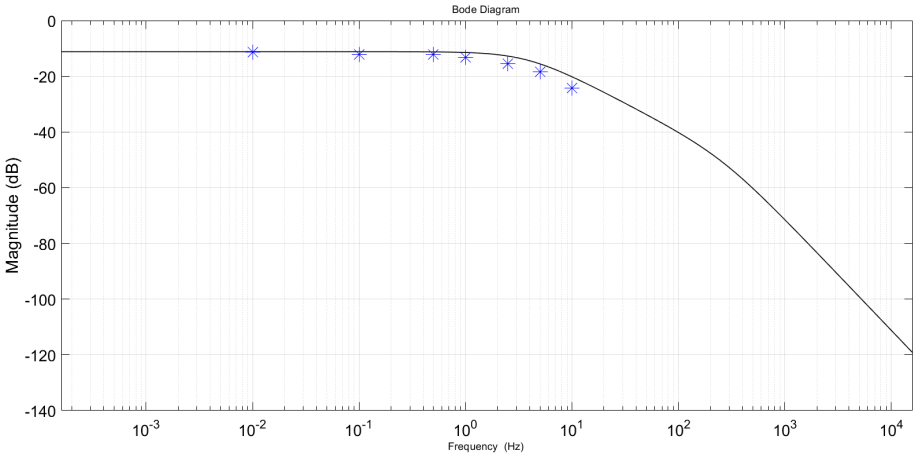

FIGURE 65: Magnitude Diagram of $\frac{\delta n_E^*}{\delta v_a^*}|_{STBD}$

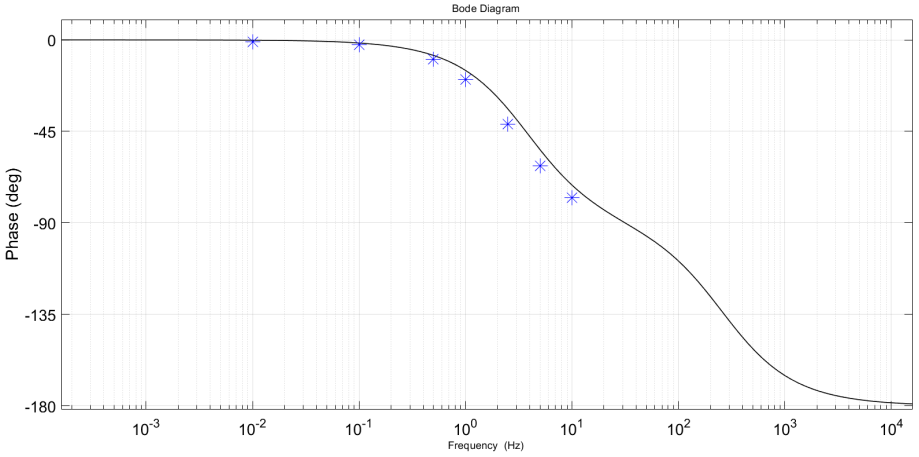

FIGURE 66: Phase Diagram of $\frac{\delta n_E^*}{\delta v_a^*}|_{STBD}$

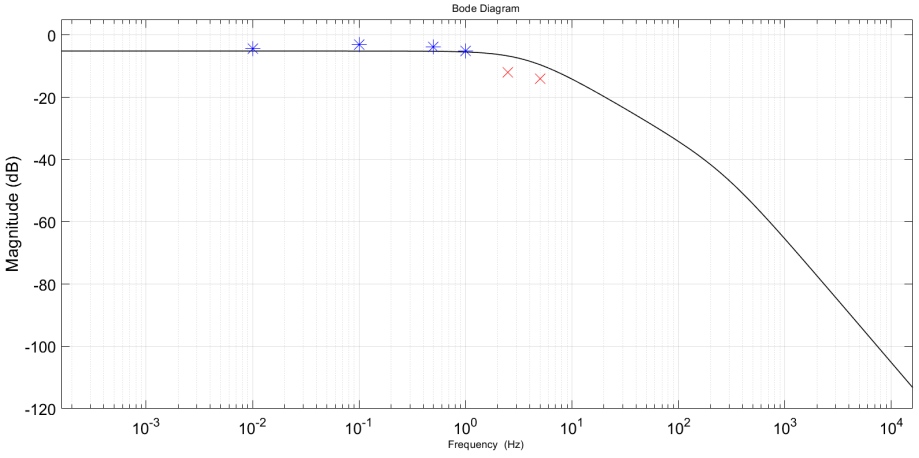

FIGURE 67: Magnitude Diagram of $\frac{\delta F_T^*}{\delta v_a^*}$

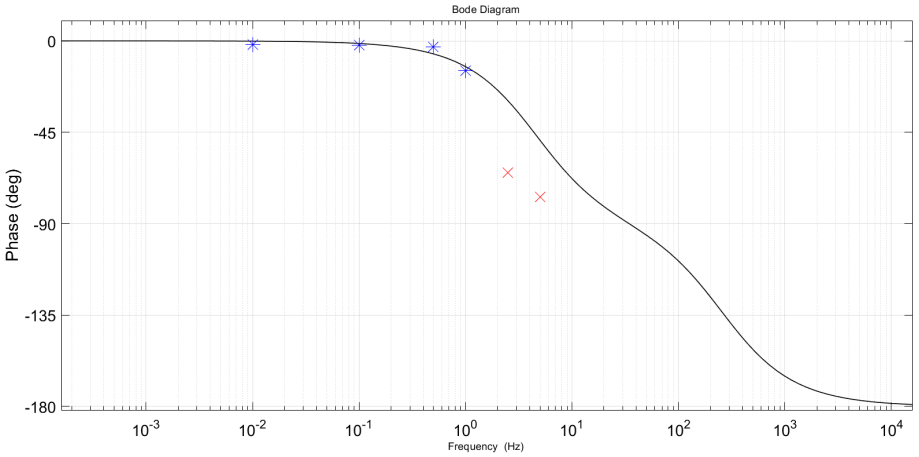

FIGURE 68: Phase Diagram of $\frac{\delta F_T^*}{\delta v_a^*}$

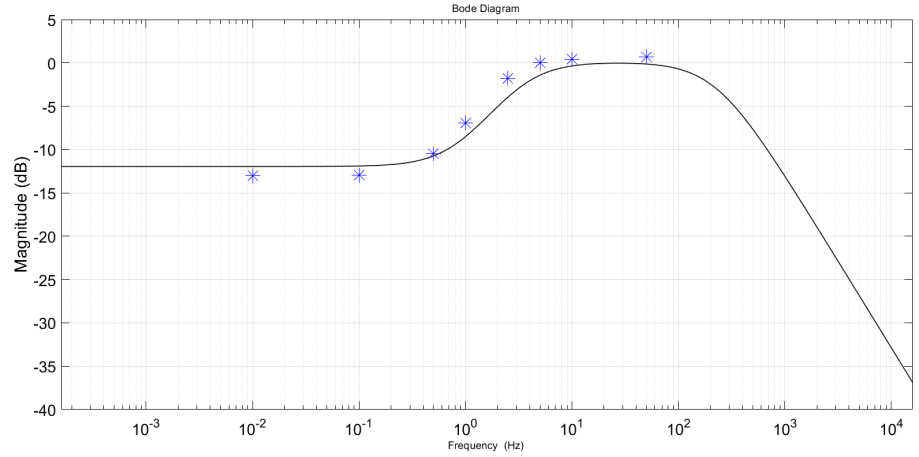

FIGURE 69: Magnitude Diagram of $\frac{\delta i_a^*}{\delta v_a^*}|_{PS}$

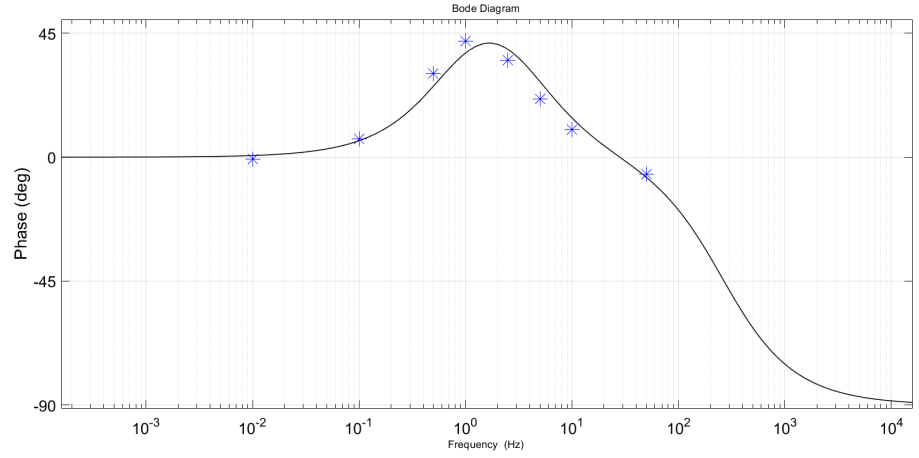

FIGURE 70: Phase Diagram of $\frac{\delta i_a^*}{\delta v_a^*}|_{PS}$

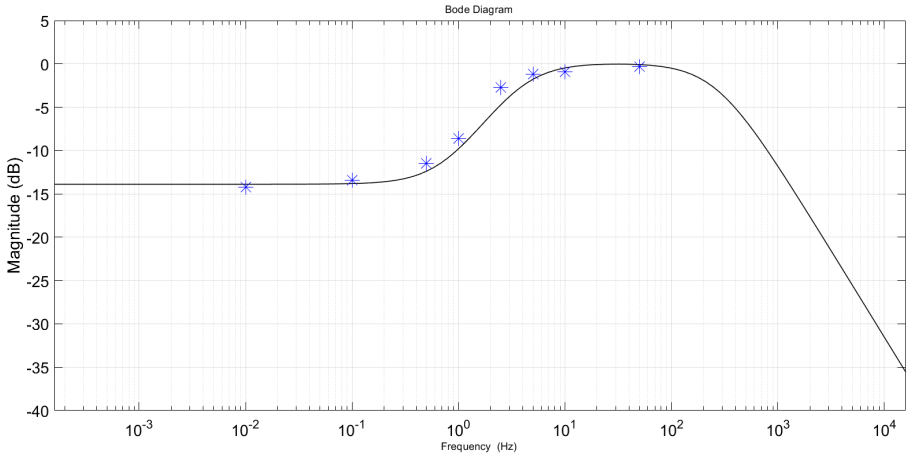

FIGURE 71: Magnitude Diagram of $\frac{\delta i_a^*}{\delta v_a^*}|_{STBD}$

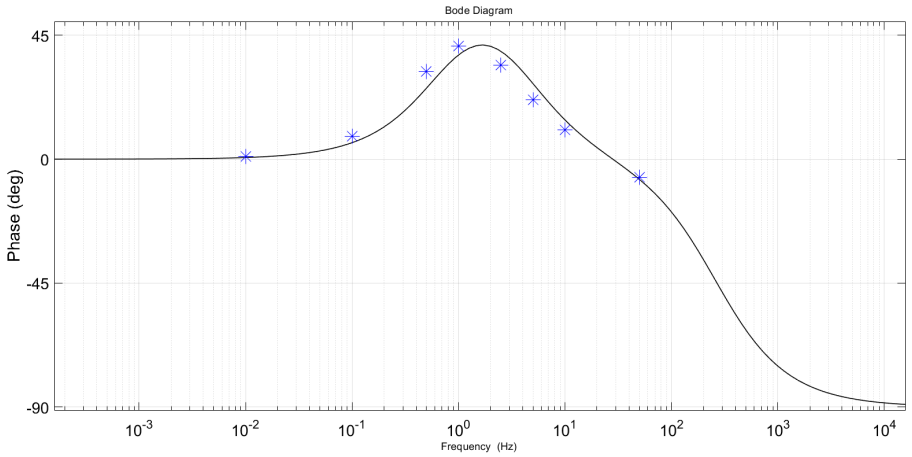

FIGURE 72: Phase Diagram of $\frac{\delta i_a^*}{\delta v_a^*}|_{STBD}$

In Bode Plot, the experimental data is reflected as star dots while the behavior of linearized model is presented by the solid curve.

The magnitude diagrams in ABS are shown in Appendix G.

The well-matched result comparison shown above indicates that the linearized model is valid enough to be used in predicting the system behavior in frequency domain. However, if looking through the experimental data, it is easy to discover that the characteristic of δi_a^*, δn_E^* and δF_T^* is different: the highest frequency of input signal which has been added during experiment is $50Hz$, at which only the measurement data of δi_a^* is still able to maintain sinusoidal form and could be transformed into the last star dot shown in Bode Plot (Fig 69 to Fig 72). δn_E^*, as shown in Fig 73, could no longer be treated as a regular sinusoidal signal under $50Hz$ therefore it is impossible to acquire corresponding star dots

in Bode Plot. As for δF_T^*, the situation is even worse: Fig 67 and 68 shows that only the experimental data dot of $0.01Hz$, $0.1Hz$, $0.5Hz$ and $1.0Hz$ has a good agreement with the simulation result. The phase of experimental data (δF_T^*) under $2.5Hz$ and $5Hz$ has a significant difference with the predicted data, which could be explained by Fig 74 and Fig 75: at $2.5Hz$ and $5Hz$, although the curve of δF_T^* may still look similar to sinusoidal curve, yet the amplitude is not stable anymore. And when the frequency increases to $10Hz$, the waveform of δF_T^* has become totally irregular and is unable to be analyzed (please be aware that the wave shown in Fig 76 may look similar to a sinusoidal wave, its frequency is almost 7 times lower than $10Hz$, the frequency which is expected).

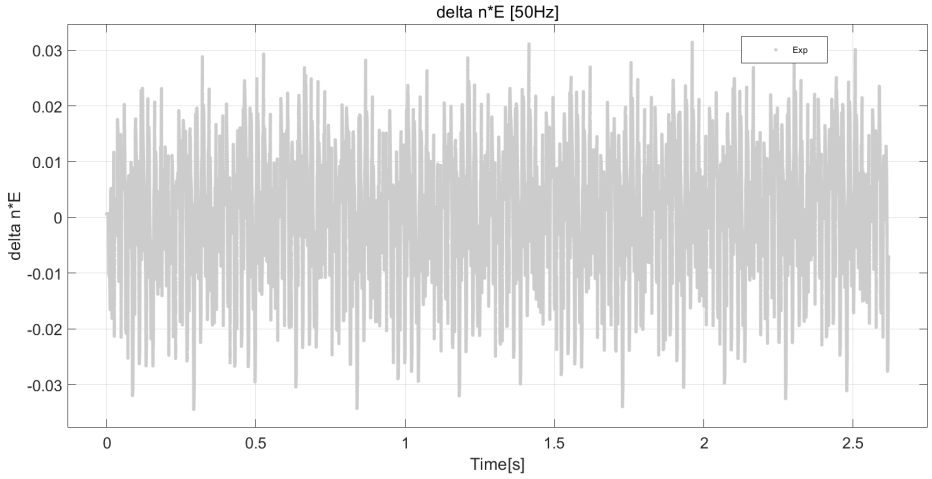

FIGURE 73: Exp data of δn_E^* at $50Hz$

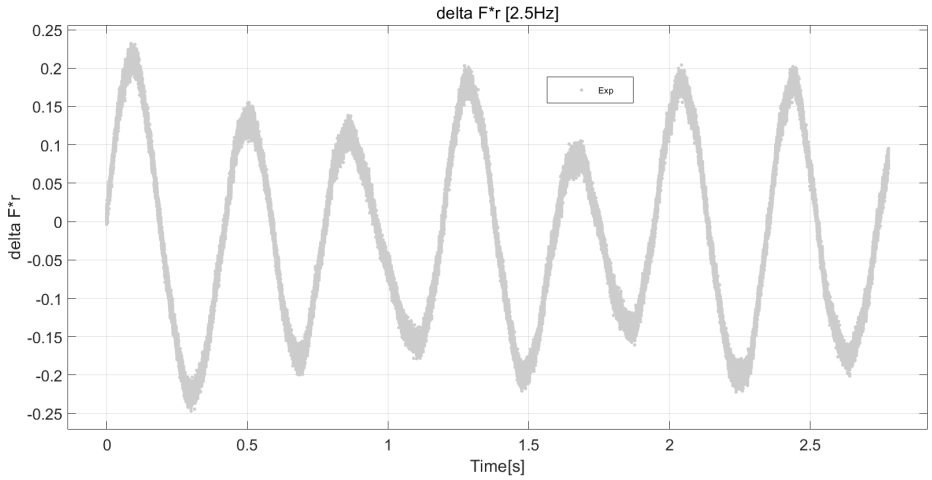

FIGURE 74: Exp data of δF_T^* at $2.5Hz$

Based on the setup, procedure and principle of the test, the author gives two possible explanations about the missing experimental data dots under high frequency of δn_E^* and δF_T^*. The first explanation is: due to the limitation of RPM sensor's and load cell's

sensitivity, the actual behavior of angular frequency n_E and thrust force F_T under high frequency failed to be reflected by the recorded measurement result. Fig 73 and 75 indicate that the measured data is very noisy while the amplitude is extremely small. Besides, other defect of the test-setup worsen the situation: after checking the recorded video of experiment, at $2.5Hz$, $5Hz$ and $10Hz$, there was an obvious pitching movement of Tito Neri, which could be explained by the information given in section 4.1. Since the extension line of load cell fails to go through the LCB, if high frequency voltage signal is supplied, there is a great possibility that the model boat can no longer prevent the unwanted movements in vertical and lateral direction, which will result in an imprecise result of force measurement.

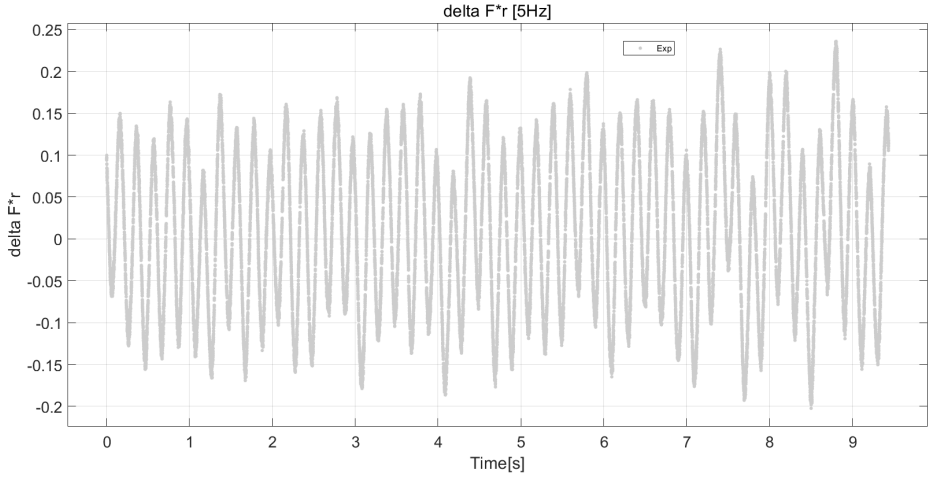

FIGURE 75: Exp data of δF_T^* at $5Hz$

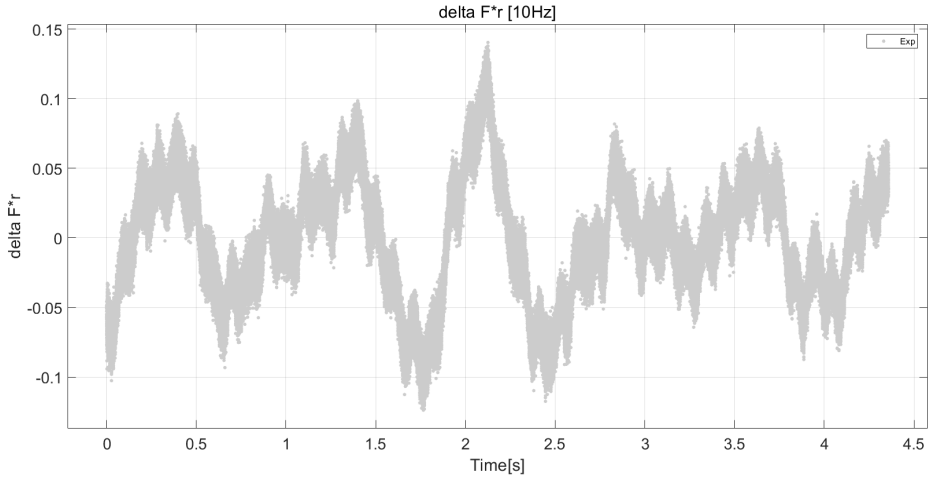

FIGURE 76: Exp data of δF_T^* at $10Hz$

The second explanation is: the mechanical system of Tito Neri's shaft line is not sensitive enough to respond to high frequency input signal whose amplitude is very small. This

could only be verified after all the defects elaborated in the first explanation have been modified: by applying a more advanced measurement system which is able to provide convincing experimental data, and if the result is still similar to the current one, then it is highly recommended by the author to conduct a detailed research about the system behavior under high frequency.

Based on previous discussion, so far, the conclusion drawn by the author is: around the steady state at which $v_a = 6.5V$, the linearized model is valid enough to be applied in predicting the behavior of Tito Neri's propulsion system within a limited region of frequency domain. Until now, the applicable frequency region of $\frac{\delta n_E^*}{\delta v_a^*}$ is lower than $50Hz$, and as for $\frac{\delta F_T^*}{\delta v_a^*}$, the region shrinks to $2.5Hz$. $\frac{\delta i_a^*}{\delta v_a^*}$ has the widest applicable region whose boundary needs to be determined in future research. Therefore, the upper bound of applicable frequency is around $2.5Hz$ (by modifying the test-setup this range should be wider).

The validated linearized model provides a solid basis for applying control technique, for instance voltage control and current control to the propulsion system while operating. Moreover, after determining the open-water propeller diagram, the linearized model under straight-line sailing condition could be built and validated by corresponding experiments, which will make the model more complete.

Chapter 7

Conclusions & Recommendations

As a sub-project of research program "Potential of Hardware-In-the-Loop Simulation in the Towing Tank", this Thesis aims at answering the research questions which are proposed in Chapter 1. Those questions relate with calibration (parameter identification), simulation, validation and linearization of Tito Neri's propulsion system. Due to the construction of shaft-line and limitations of measurement equipment, Question 2 and 4 have not been completely answered yet and more effort are required in the future. Therefore, in this Chapter, the main conclusions and recommendations of this Thesis will be summarized.

7.1 Conclusions

By analyzing the structure of Tito Neri's propulsion system, combined with corresponding physical laws, its mathematical model under bollard-pull and straight-line sailing condition could be determined. By looking through the mathematical model, the required parameters are able to be classified into DC motor related parameters, mechanical parameters and hydrodynamic parameters.The first and the second type of parameters could be identified by result analysis of dry-run tests while the related expressions of the last type must be acquired from hydrodynamic tests.

After being identified, the validity of those parameters (together with the validity of simulation model) was determined by result comparison between simulation and experiment, through which it has been discovered that most values of DC motor related parameters and mechanical parameters shown in Table 3.5 (except the friction torque) together with the simulation model shown in Fig 25 are valid enough for future use. The result of hydrodynamic tests, especially the propeller open-water curve of high J, on the other hand, is not convincing enough and needs to be improved in the future. But according to the discussion in section 5.2, the value of K_T and K_Q derived from the result of bollard-pull test should be reasonable, and this opinion has been approved later by the validation work elaborated in section 5.3.

In order to give a more straightforward view, validity of the identified parameters is summarized in Table 7.1.

Besides parameter identification and corresponding validation, by applying and extending the linearization method proposed by D.Stapersma and A.Vrijdag in Paper [2], the linearized (mathematical) model of Tito Neri's propulsion system under bollard-pull conditions, including Eq 6.45, 6.51 and 6.57, was constructed. After determining the corresponding Laplace Transfer Functions Eq 6.58 to 6.60, the validity of this linearized

model has been examined by experiment and a convincing result is shown by Fig 63 to Fig 72. However, it must be addressed that currently the validity has only been proved within a limited (frequency) region for δi_a^*, δn_E^* and δF_T^* simultaneously (below $2.5Hz$), which requires more exploration in the future.

TABLE 7.1: **Validity of Identified Parameters**

Parameter	**Validity**
$I_{p2}\ (kg \cdot m^2)$	$++$
$I_{p3}\ (kg \cdot m^2)$	$+$
$R_{ele}\ (\Omega)$	$+$
$K_m\ (N \cdot m/A)$	$+$
$L\ (H)$	$+$
$I_{p1}\ (kg \cdot m^2)$	$+$
$M_{BF}\ (N \cdot m)$	$+/-$
$M_{F1} + M_{F2}\ (N \cdot m)$	$+/-$
$R\ (N)$	$-$
K_T	$-$
K_Q	$-$

- *"++" means the determined value of this parameter is almost* 100% *trustable and no more validation is needed in the future*
- *"+" means the determined value is highly trustable, but a more precise measurement during future experiment may provide a more accurate result*
- *"−" means validity of this parameter is very poor (K_T and K_Q) or has not been proved (R), therefore the determined value could not be trusted so far*
- $+/-$ *of friction torque means the determined value is valid enough under high angular frequency, yet under low angular frequency it is another story*

7.2 Recommendations

Recommendations given by the author in this section mainly focus on modifying the result of parameter identification (which includes creating a more detailed friction model and trying to acquire a convincing propeller open-water diagram), improving the quality of bollard-pull experiments which is related with validation of the linearized model, and a few discussion about extending the linearized model to predict system behavior under straight-line sailing condition.

Based on the information given in section 3.4.1 and section 5.3, it is acknowledged that all the friction torques of this propulsion system, which includes M_{BF}, M_{F1} and M_{F2}, their values are assumed to be irrelevant with shaft angular frequency and the operating condition (dry-run or wet-run). This assumption plays a very important role in simplifying the procedure of parameter identification and has been proved to be valid for most cases by the well agreement between experimental data & simulation result, yet Fig 27 and 28 suggest that this assumption also has its limitation, especially when the supplied voltage is relatively low.

According to Eq 2.20 and Eq 2.33, the function of friction model is determined by result analysis of dry-run tests under steady state. Therefore, more stable voltage supplier as well as more reliable current sensors are required when conducting dry-run tests in the future so as to modify the test result. Besides, the author is also keen to find out why under low supplied voltage (or angular frequency), the Coulomb Friction Model is not perfectly suitable. And after examining the shaft-line construction, it was observed that component-3 (shaft bearing) had not been well mounted and may needed to be replaced. This provides a potential explanation for the friction issue.

With a more complete friction model, the application range of the simulation model shown in this Thesis will be wider. For instance, if the friction characteristic of this propulsion system under low shaft angular frequency could be described precisely in the future, the simulation model will then be able to applied as the basis of designing a Dynamic-Positioning system (which usually operates under low voltage) for MT218 Course.

Another parameter which requires to be determined is propeller open-water diagram. In this Thesis, due to the questionable result of propeller "open-water" test, the author failed to give a convincing expression of K_T and K_Q when J is not 0, which made it impossible to build and validate the linearized model under straight-line sailing condition. According to section 5.3, the main reason leading to this failure is unreliability of the load cell, so one way to improve is redoing the "open-water" test with accurate force measurement. However, this cannot eliminate the interaction between hull and propeller, therefore the author suggests to apply 3D scanning technique and tries to determine the open-water diagram through CFD analysis.

Besides parameter identification, the author also discussed linearization of Tito Neri's propulsion system. In Chapter 6, one linearized model under bollard-pull condition is built and validated. As indicated in section 6.4, the validity needs to be explored more, especially for the applicable frequency range of $\frac{\delta F_T^*}{\delta V_a^*}$, which could be done through modifying the test-setup, for instance letting the extension line of load cell to go through

the LCB and preventing the unwanted movements which will result in an imprecise result of force measurement.

In order to reach the ultimate goal of this research program, building and validating the linearized model under straight-line sailing condition is of vital importance. Because this linearized model is the basis of introducing voltage or current control. Except for the convincing propeller open-water diagram, a wireless experimental system must be designed and set up for straight-line sailing test in the future.

Last but not least, during the past 15 months working with Mr.Vrijdag, the author gradually learned the importance and benefits of a proper time management. Except for knowledge, this is the most precious experience the author has acquired from the MSc graduation project.

Appendix A

Datasheet of Allegro ACS712

The brand of current sensor is ACS712ELCTR-05B-T, and its absolute maximum ratings are given below:

Absolute Maximum Ratings

Characteristic	Symbol	Notes	Rating	Units
Supply Voltage	V_{CC}		8	V
Reverse Supply Voltage	V_{RCC}		–0.1	V
Output Voltage	V_{IOUT}		8	V
Reverse Output Voltage	V_{RIOUT}		–0.1	V
Output Current Source	$I_{IOUT(Source)}$		3	mA
Output Current Sink	$I_{IOUT(Sink)}$		10	mA
Overcurrent Transient Tolerance	I_P	1 pulse, 100 ms	100	A
Nominal Operating Ambient Temperature	T_A	Range E	–40 to 85	°C
Maximum Junction Temperature	T_J(max)		165	°C
Storage Temperature	T_{stg}		–65 to 170	°C

FIGURE 77: Absolute Maximum Ratings

To give a clearer view of this current sensor, the Pin-out diagram and terminal list are given below:

Pin-out Diagram

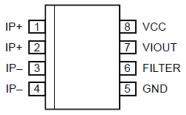

Terminal List Table

Number	Name	Description
1 and 2	IP+	Terminals for current being sampled; fused internally
3 and 4	IP–	Terminals for current being sampled; fused internally
5	GND	Signal ground terminal
6	FILTER	Terminal for external capacitor that sets bandwidth
7	VIOUT	Analog output signal
8	VCC	Device power supply terminal

FIGURE 78: Pin-Out Diagram and Terminal List

And the operating characteristics is:

COMMON OPERATING CHARACTERISTICS[1] over full range of T_A, C_F = 1 nF, and V_{CC} = 5 V, unless otherwise specified

Characteristic	Symbol	Test Conditions	Min.	Typ.	Max.	Units
ELECTRICAL CHARACTERISTICS						
Supply Voltage	V_{CC}		4.5	5.0	5.5	V
Supply Current	I_{CC}	V_{CC} = 5.0 V, output open	–	10	13	mA
Output Capacitance Load	C_{LOAD}	VIOUT to GND	–	–	10	nF
Output Resistive Load	R_{LOAD}	VIOUT to GND	4.7	–	–	kΩ
Primary Conductor Resistance	$R_{PRIMARY}$	T_A = 25°C	–	1.2	–	mΩ
Rise Time	t_r	I_P = I_P(max), T_A = 25°C, C_{OUT} = open	–	3.5	–	µs
Frequency Bandwidth	f	–3 dB, T_A = 25°C; I_P is 10 A peak-to-peak	–	80	–	kHz
Nonlinearity	E_{LIN}	Over full range of I_P	–	1.5	–	%
Symmetry	E_{SYM}	Over full range of I_P	98	100	102	%
Zero Current Output Voltage	$V_{IOUT(Q)}$	Bidirectional; I_P = 0 A, T_A = 25°C	–	V_{CC} × 0.5	–	V
Power-On Time	t_{PO}	Output reaches 90% of steady-state level, T_J = 25°C, 20 A present on leadframe	–	35	–	µs
Magnetic Coupling[2]			–	12	–	G/A
Internal Filter Resistance[3]	$R_{F(INT)}$			1.7		kΩ

[1]Device may be operated at higher primary current levels, I_P, and ambient, T_A, and internal leadframe temperatures, T_A, provided that the Maximum Junction Temperature, T_J(max), is not exceeded.
[2]1G = 0.1 mT.
[3]$R_{F(INT)}$ forms an RC circuit via the FILTER pin.

FIGURE 79: x05B Performance Characteristics

Please be aware that Fig 77 to Fig 79 are all extracted from the datasheet of ACS712ELCTR-05B-T. The original file could be easily found on the internet.

Appendix B

Information about DEWE-43 Board and SIRIUS Board

Fig 80 and 81 show the channels of DEWE-43 board and SIRIUS board individually. Combined with the content of Chapter 3, connection between components of test-setup is clearer. More detailed information could be found through the Technical Reference Manual from www.dewesoft.com/products.

FIGURE 80: Channels of DEWE-43 board

FIGURE 81: Channels of SIRIUS board

Appendix C

Result Comparison of other Two Dry-run Tests

Besides the dry-run test elaborated in Chapter 3, another two dry-run tests were also conducted to validate the parameters as well as the simulation model. The first one is the upward ramp whose result comparison is given below:

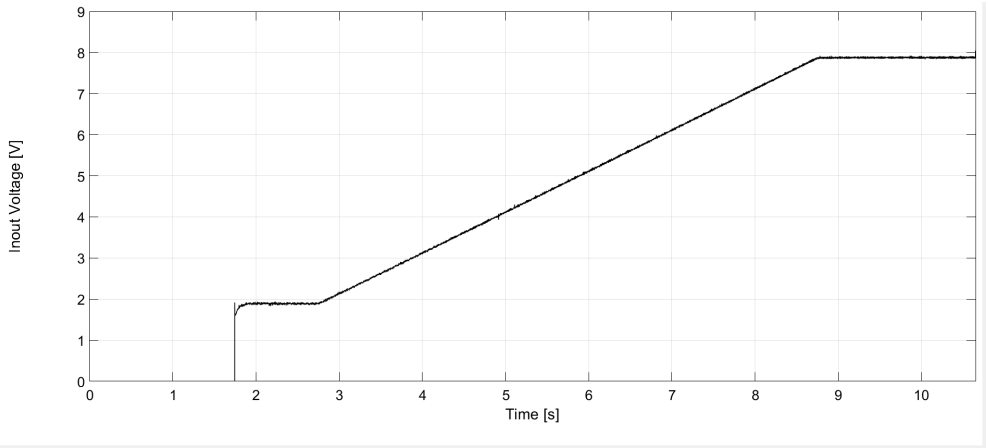

FIGURE 82: Input Voltage Signal (upward ramp)

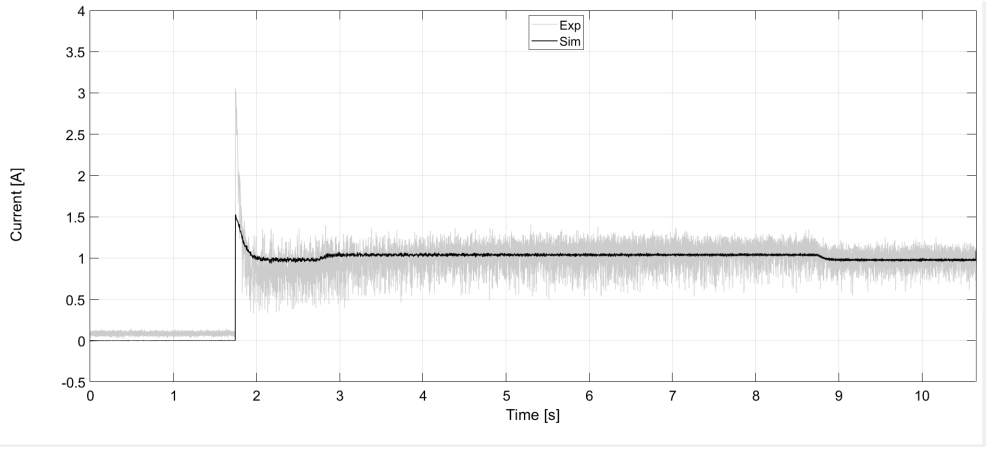

FIGURE 83: Result Comparison of Current

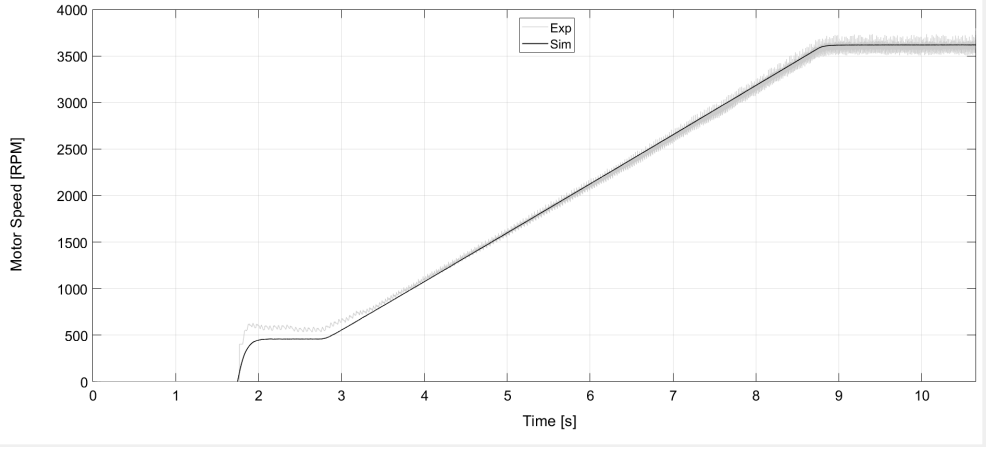

FIGURE 84: Result Comparison of Motor Speed

The second one is the multiple-step dry-run test:

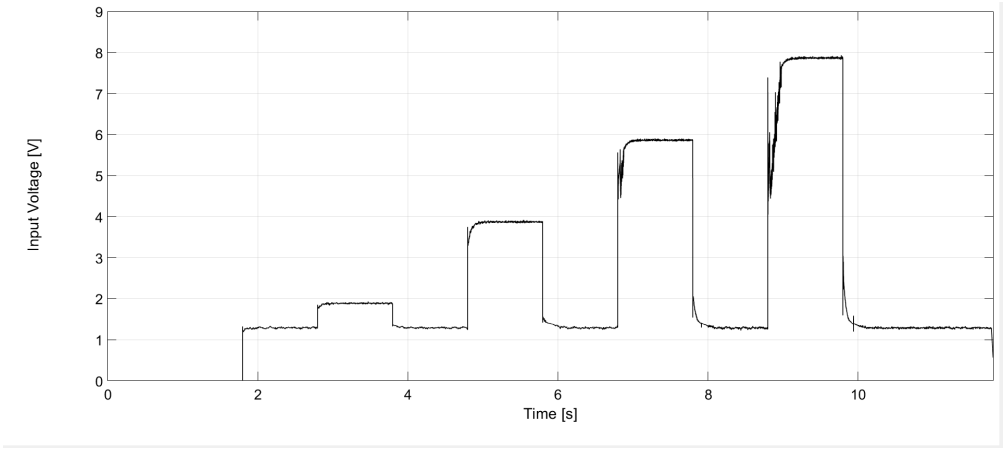

FIGURE 85: Input Voltage Signal (multiple-step)

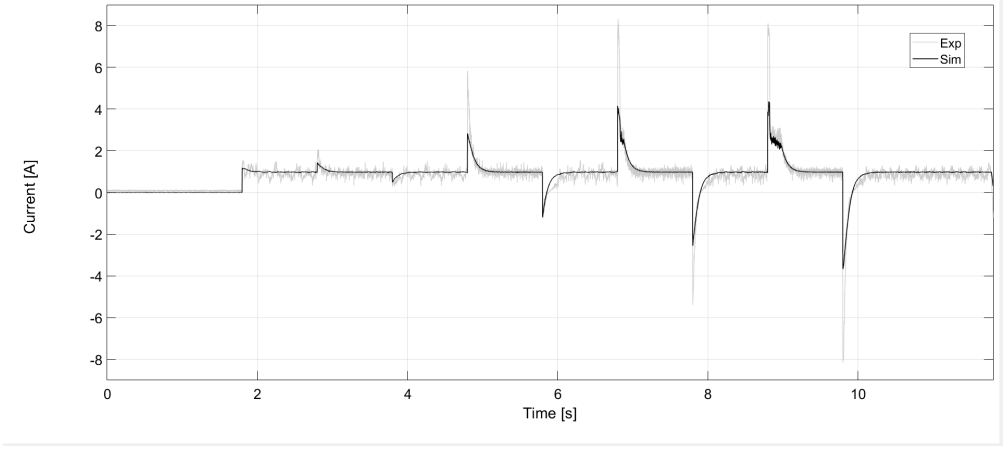

FIGURE 86: Result Comparison of Current

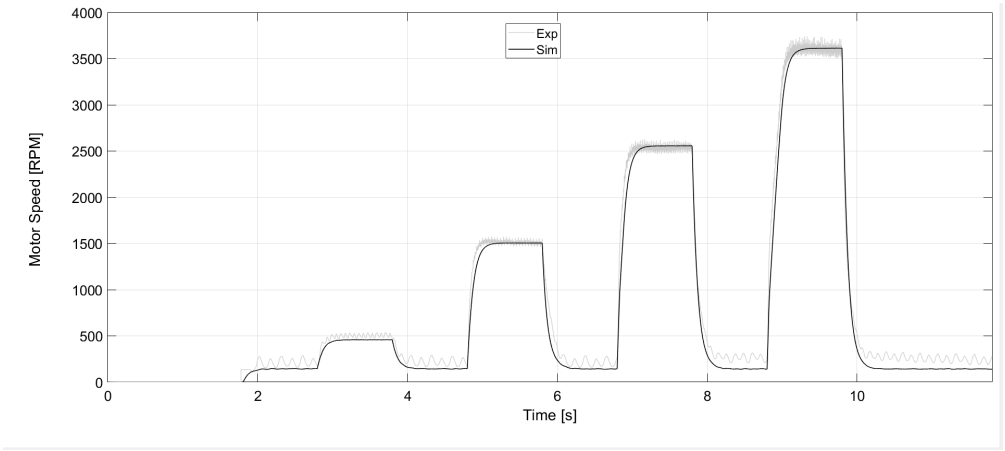

FIGURE 87: Result Comparison of Motor Speed

The result conparison shown above indicates that the test result matches well with simulation result. Furthermore it proves the validity of the simulation model together with the defined parameters.

Appendix D

Result Comparison for Bollard-pull Test When Block Signal is Added

When a block signal with a frequency of $0.1Hz$ is added to the system under bollard-pull condition, the result comparison between experimental data and simulation is given below:

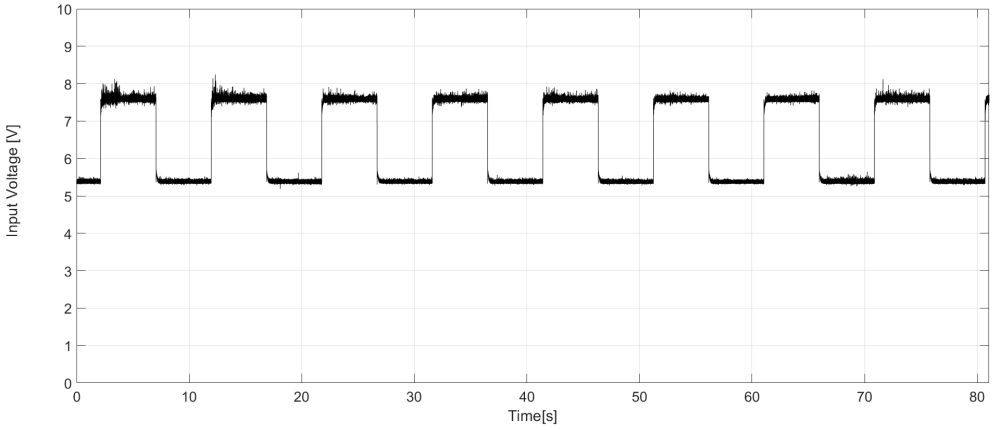

FIGURE 88: Input Voltage Signal $0.1Hz$ under Bollard-pull Condition

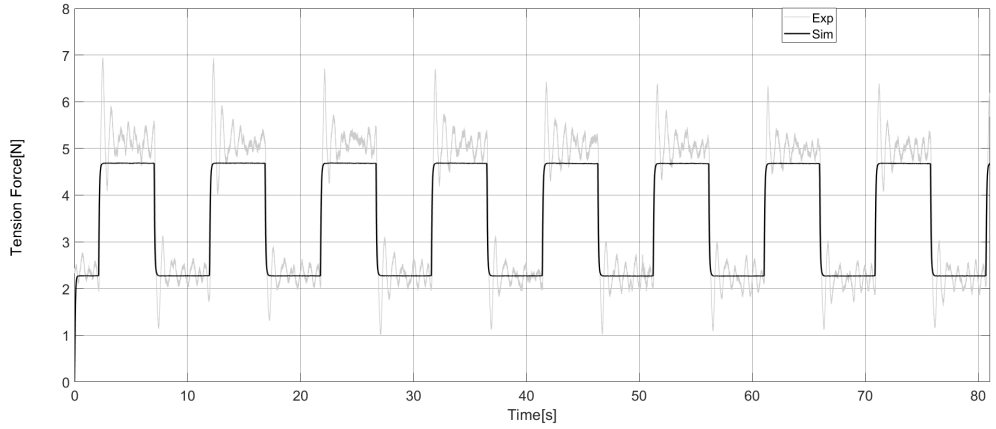

FIGURE 89: Comparison of Tension Force under Bollard-pull Condition

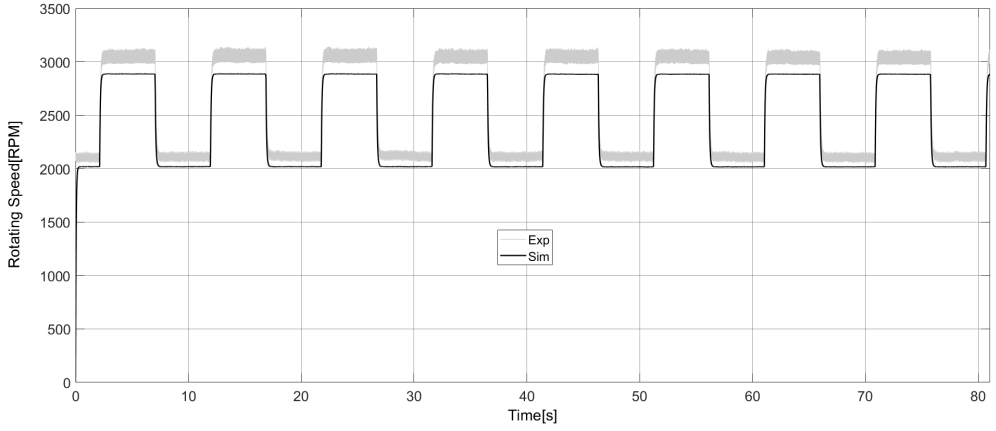

FIGURE 90: Comparison of motor speed PS under Bollard-pull Condition

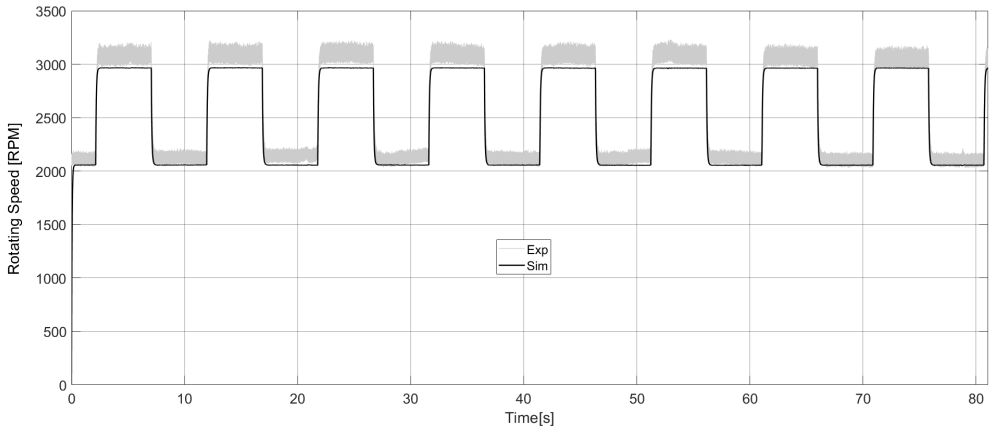

FIGURE 91: Comparison of motor speed STBD under Bollard-pull Condition

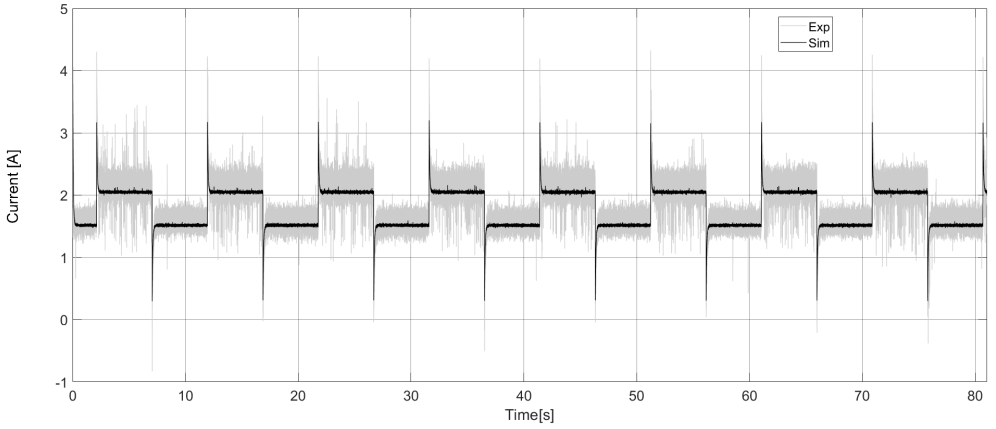

FIGURE 92: Comparison of current PS under Bollard-pull Condition

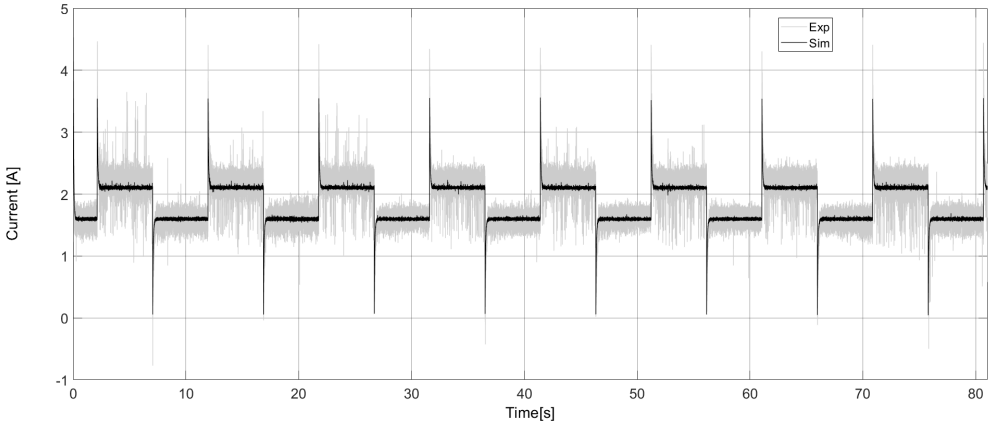

FIGURE 93: Comparison of current STBD under Bollard-pull Condition

Although there is some difference on the peak value of tension force (Fig 89) and shaft angular frequency (Fig 90 and 91), Fig 89 to Fig 93 indicates a well agreement between

experimental data and simulation result, which also proves the validity of the simulation model shown in Fig 49 and 50 when there is a sudden increase or decrease of input voltage.

Appendix E

Example and Relevant Data of Curve Fitting

From section 6.4 it is acknowledged that the normalized variables are:

$$\delta v_a^* = \frac{A \cdot sin(Bt + C)}{v_{a,0} - 2\pi \cdot K_m \cdot n_{E,0}} = A^* \cdot sin(Bt + C)$$

$$\delta n_E^* = \frac{A_1 \cdot sin(Bt + C_1)}{n_{E,0}} = A_1^* \cdot sin(Bt + C_1)$$

$$\delta F_T^* = \frac{A_2 \cdot sin(Bt + C_2)}{F_{T,0}} = A_2^* \cdot sin(Bt + C_2)$$

$$\delta i_a^* = \frac{A_3 \cdot sin(Bt + C_3)}{i_{a,0}} = A_3^* \cdot sin(Bt + C_3)$$

And in order to determine the value of A_i^* and C_i, the experimental data must be analyzed. The way to analyze data is curve fitting and the theory behind is least-square method. The analysis under frequency of $0.01Hz$ is given below as an example:

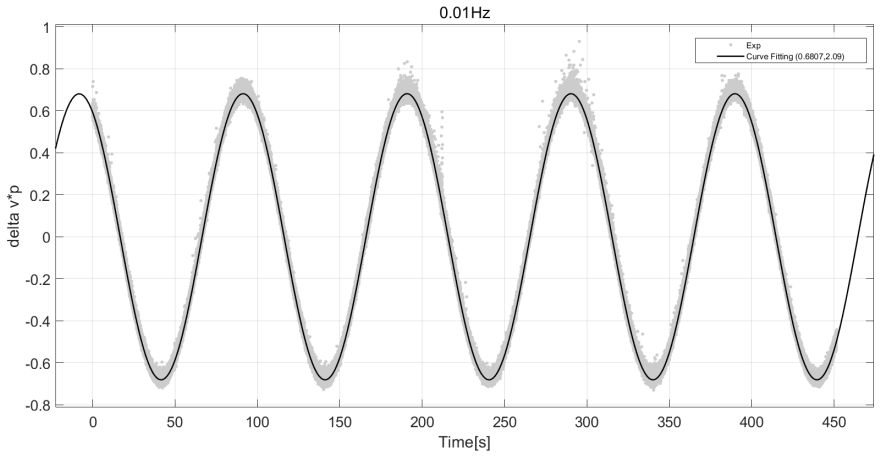

FIGURE 94: Curve Fitting of $\delta v_a^*|_{PS}$ of $0.01Hz$

After importing the experimental data of v_a into MatLab, after normalization, the grey-dot line shown in Fig 94 could be created. And by applying the curve-fitting tool of MatLab, the black solid curve is able to be graphed and the corresponding expression of $A^* \cdot sin(Bt + C)$ could be determined as follows:

$$\delta v_a^* = A^* \cdot sin(Bt + C) = 0.6807 \cdot sin(0.06314t + 2.09)$$

Please be aware that the value of C, which is equal to 2.09, is in radians and it should be transferred to degrees by $2.09 \cdot \frac{180}{\pi} = 376.2^o$.

By using the same way, the curve fitting graph of $\delta n_E^*, \delta F_T^*, \delta i_a^*$ are given below:

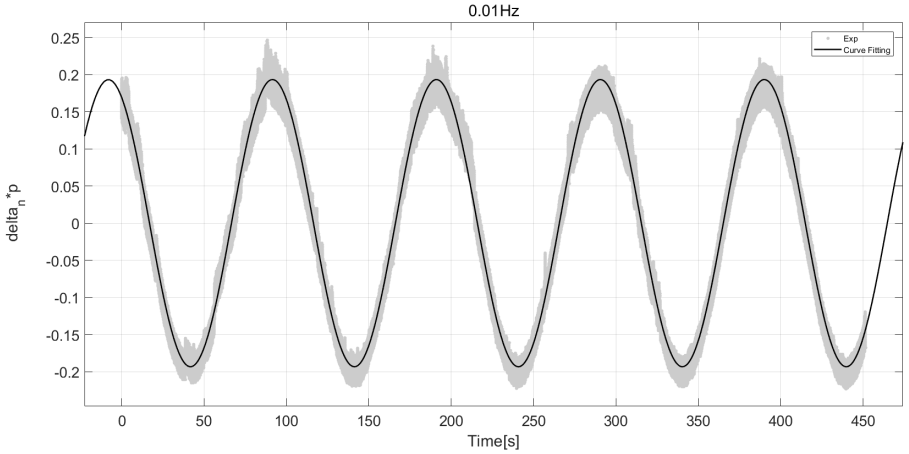

FIGURE 95: Curve Fitting of $\delta n_E^*|_{PS}$ of $0.01Hz$

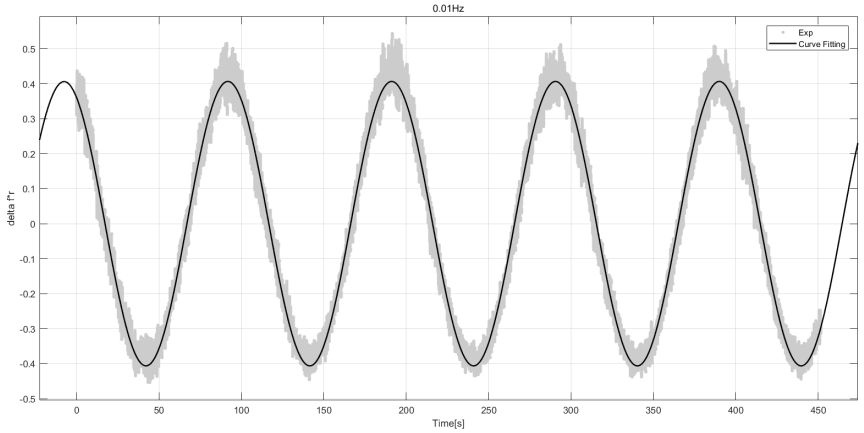

FIGURE 96: Curve Fitting of δF_T^* of $0.01Hz$

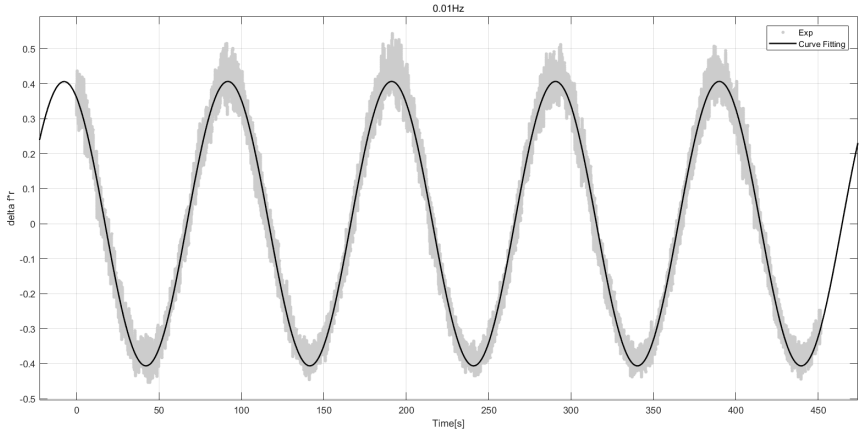

FIGURE 97: Curve Fitting of $\delta i_a^*|_{PS}$ of $0.01Hz$

The coefficients are given in Table E.1:

TABLE E.1: **Value of Coefficients under** $0.01Hz$

	$\boldsymbol{A_i^*}$	$\boldsymbol{C_i}$
$\delta v_a^*\|_{PS}$	0.6807	2.09
$\delta n_E^*\|_{PS}$	0.1934	2.076
$\delta i_a^*\|_{PS}$	0.1515	2.078
$\delta v_a^*\|_{STBD}$	0.712	2.089
$\delta n_E^*\|_{STBD}$	0.1922	2.073
$\delta i_a^*\|_{STBD}$	0.1416	2.105
δF_T^*	0.4063	2.056

And the coefficients under other frequency are given in the coming tables:

TABLE E.2: **Value of Coefficients under** $0.1Hz$

	$\boldsymbol{A_i^*}$	$\boldsymbol{C_i}$
$\delta v_a^*\|_{PS}$	0.09936	2.346
$\delta n_E^*\|_{PS}$	0.03084	2.28
$\delta i_a^*\|_{PS}$	0.02215	2.493
$\delta v_a^*\|_{STBD}$	0.1069	2.349
$\delta n_E^*\|_{STBD}$	0.02966	2.308
$\delta i_a^*\|_{STBD}$	0.02356	2.494
δF_T^*	0.06565	2.372

TABLE E.3: **Value of Coefficients under** $0.5Hz$

	$\boldsymbol{A_i^*}$	$\boldsymbol{C_i}$
$\delta v_a^*\|_{PS}$	0.7151	-1.309
$\delta n_E^*\|_{PS}$	0.1801	-1.529
$\delta i_a^*\|_{PS}$	0.2137	-0.7791
$\delta v_a^*\|_{STBD}$	0.7355	-1.314
$\delta n_E^*\|_{STBD}$	0.1791	-1.48
$\delta i_a^*\|_{STBD}$	0.1963	-0.7571
δF_T^*	0.4738	-1.368

TABLE E.4: **Value of Coefficients under** $1.0Hz$

	$\boldsymbol{A_i^*}$	$\boldsymbol{C_i}$
$\delta v_a^*\|_{PS}$	0.6807	0.6425
$\delta n_E^*\|_{PS}$	0.1647	0.295
$\delta i_a^*\|_{PS}$	0.3056	1.379
$\delta v_a^*\|_{STBD}$	0.7021	0.6465
$\delta n_E^*\|_{STBD}$	0.1647	0.3049
$\delta i_a^*\|_{STBD}$	0.2826	1.363
δF_T^*	0.4289	0.3899

TABLE E.5: **Value of Coefficients under** $2.5Hz$

	A_i^*	C_i
$\delta v_a^*\|_{PS}$	0.6538	1.889
$\delta n_E^*\|_{PS}$	0.1245	1.156
$\delta i_a^*\|_{PS}$	0.5138	2.511
$\delta v_a^*\|_{STBD}$	0.685	1.899
$\delta n_E^*\|_{STBD}$	0.1251	1.152
$\delta i_a^*\|_{STBD}$	0.5211	2.534
δF_T^*	0.1637	-0.1082

TABLE E.6: **Value of Coefficients under** $5.0Hz$

	A_i^*	C_i
$\delta v_a^*\|_{PS}$	0.6201	-0.2166
$\delta n_E^*\|_{PS}$	0.07551	-1.301
$\delta i_a^*\|_{PS}$	0.6201	0.1564
$\delta v_a^*\|_{STBD}$	0.6501	-0.2116
$\delta n_E^*\|_{STBD}$	0.07817	-1.291
$\delta i_a^*\|_{STBD}$	0.5661	0.1633
δF_T^*	0.1242	2.697

TABLE E.7: **Value of Coefficients under** $10Hz$

	A_i^*	C_i
$\delta v_a^*\|_{PS}$	0.6055	0.1483
$\delta n_E^*\|_{PS}$	0.04084	-1.196
$\delta i_a^*\|_{PS}$	0.6359	0.3232
$\delta v_a^*\|_{STBD}$	0.6354	0.1481
$\delta n_E^*\|_{STBD}$	0.03919	-1.205
$\delta i_a^*\|_{STBD}$	0.59	0.3351
δF_T^*	#	#

TABLE E.8: **Value of Coefficients under** $50Hz$

	A_i^*	C_i
$\delta v_a^*\|_{PS}$	0.6049	-2.257
$\delta i_a^*\|_{PS}$	0.6572	-2.363
$\delta v_a^*\|_{STBD}$	0.6583	-2.257
$\delta i_a^*\|_{STBD}$	0.6361	-2.372

Based on the coefficients shown above, the magnitude and phase of Bode Plot could be determined by:

$$\begin{cases} \frac{\delta x^*}{\delta v_a^*}|_{Gain} = 20 \cdot \log(\frac{A_i^*}{A^*}) \\ \frac{\delta x^*}{\delta v_a^*}|_{Phase} = (C_i - C) \cdot \frac{180}{\pi} \end{cases} \tag{E.1}$$

Appendix F

Derivation of the Laplace Transfer Functions

Based on Eq 6.45, 6.51, after applying Laplace Transform, there is:

$$\begin{cases} s \cdot \tau_e \cdot \delta I_a^* = \delta V_a^* - \delta I_a^* - \dfrac{2\pi K_b \cdot n_{E,0}}{v_{a,0} - 2\pi K_b \cdot n_{E,0}} \cdot \delta N_E^* \\ s \cdot \tau_m \cdot \delta N_E^* = \dfrac{K_m \cdot i_{a,0}}{K_m \cdot i_{a,0} - M_F} \cdot \delta I_a^* - 2 \cdot \delta N_E^* \end{cases} \tag{F.1}$$

After elimination by substitution, Eq F.1 could be transformed to:

$$\frac{\delta N_E^*}{\delta V_a^*} = \frac{K_m \cdot R \cdot i_{a,0}^2}{R \cdot i_{a,0} \cdot (2 + s \cdot \tau_m)(1 + s \cdot \tau_e)(K_m \cdot i_{a,0} - M_F) + 2\pi K_m^2 \cdot i_{a,0} \cdot n_{E,0}} \tag{F.2}$$

$$\frac{\delta I_a^*}{\delta V_a^*} = \frac{R \cdot i_{a,0} \cdot (2 + s \cdot \tau_m)(K_m \cdot i_{a,0} - M_F)}{R \cdot i_{a,0} \cdot (2 + s \cdot \tau_m)(1 + s \cdot \tau_e)(K_m \cdot i_{a,0} - M_F) + 2\pi K_m^2 \cdot i_{a,0} \cdot n_{E,0}} \tag{F.3}$$

And according to Eq 6.57, there is:

$$\frac{\delta F_T^*}{\delta V_a^*} = \frac{2K_m \cdot R \cdot i_{a,0}^2}{R \cdot i_{a,0} \cdot (2 + s \cdot \tau_m)(1 + s \cdot \tau_e)(K_m \cdot i_{a,0} - M_F) + 2\pi K_m^2 \cdot i_{a,0} \cdot n_{E,0}} \tag{F.4}$$

If rewrite Eq F.2 to F.4 in standard form, there are:

$$\frac{\delta N_E^*}{\delta V_a^*} = \frac{K_m \cdot R \cdot i_{a,0}^2}{H \cdot \tau_e \cdot \tau_m \cdot s^2 + H \cdot (2\tau_e + \tau_m) \cdot s + 2 \cdot H + 2\pi K_m^2 \cdot i_{a,0} \cdot n_{E,0}} \tag{F.5}$$

$$\frac{\delta I_a^*}{\delta V_a^*} = \frac{2 \cdot H + H \cdot \tau_m \cdot s}{H \cdot \tau_e \cdot \tau_m \cdot s^2 + H \cdot (2\tau_e + \tau_m) \cdot s + 2 \cdot H + 2\pi K_m^2 \cdot i_{a,0} \cdot n_{E,0}} \tag{F.6}$$

$$\frac{\delta F_T^*}{\delta V_a^*} = \frac{2K_m \cdot R \cdot i_{a,0}^2}{H \cdot \tau_e \cdot \tau_m \cdot s^2 + H \cdot (2\tau_e + \tau_m) \cdot s + 2 \cdot H + 2\pi K_m^2 \cdot i_{a,0} \cdot n_{E,0}} \tag{F.7}$$

In which $H = K_m \cdot R \cdot i_{a,0}^2 - M_F \cdot R \cdot i_{a,0}$.

The DC gains are given below:

$$\frac{\delta N_E^*}{\delta V_a^*}|_{DCgain} = \frac{K_m \cdot R \cdot i_{a,0}^2}{2 \cdot (K_m \cdot R \cdot i_{a,0}^2 - M_F \cdot R \cdot i_{a,0}) + 2\pi K_m^2 \cdot i_{a,0} \cdot n_{E,0}}$$

$$\frac{\delta I_a^*}{\delta V_a^*}|_{DCgain} = \frac{2 \cdot (K_m \cdot R \cdot i_{a,0}^2 - M_F \cdot R \cdot i_{a,0})}{2 \cdot (K_m \cdot R \cdot i_{a,0}^2 - M_F \cdot R \cdot i_{a,0}) + 2\pi K_m^2 \cdot i_{a,0} \cdot n_{E,0}}$$

$$\frac{\delta F_T^*}{\delta V_a^*}|_{DCgain} = \frac{2 \cdot K_m \cdot R \cdot i_{a,0}^2}{2 \cdot (K_m \cdot R \cdot i_{a,0}^2 - M_F \cdot R \cdot i_{a,0}) + 2\pi K_m^2 \cdot i_{a,0} \cdot n_{E,0}}$$

Appendix G

Magnitude Diagrams of Bode Plot in ABS

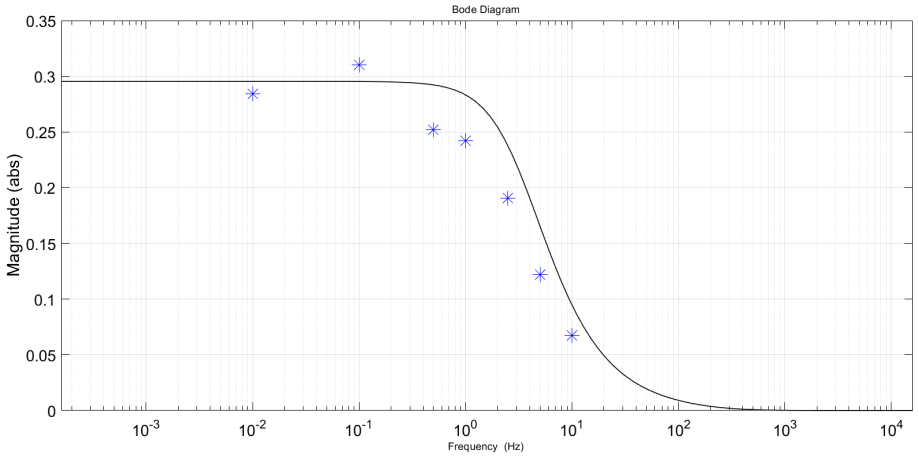

FIGURE 98: Magnitude Diagram of $\frac{\delta n_E^*}{\delta v_a^*}|_{PS}$

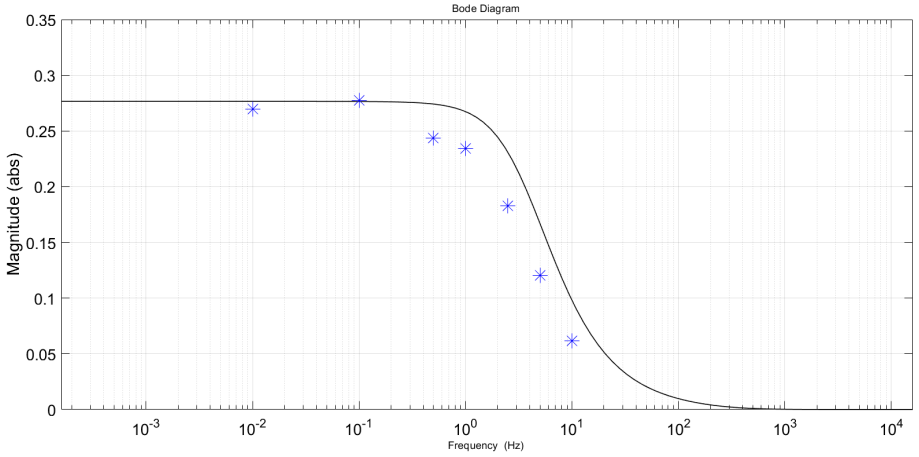

FIGURE 99: Magnitude Diagram of $\frac{\delta n_E^*}{\delta v_a^*}|_{STBD}$

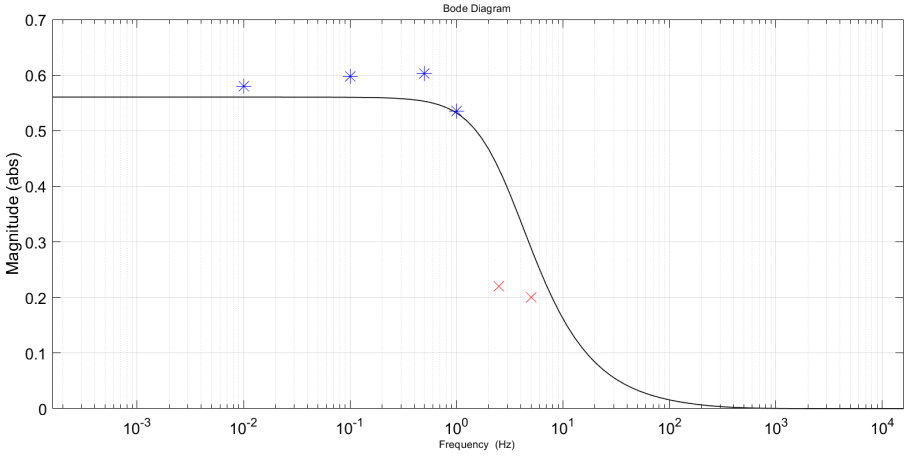

FIGURE 100: Magnitude Diagram of $\frac{\delta F_T^*}{\delta v_a^*}$

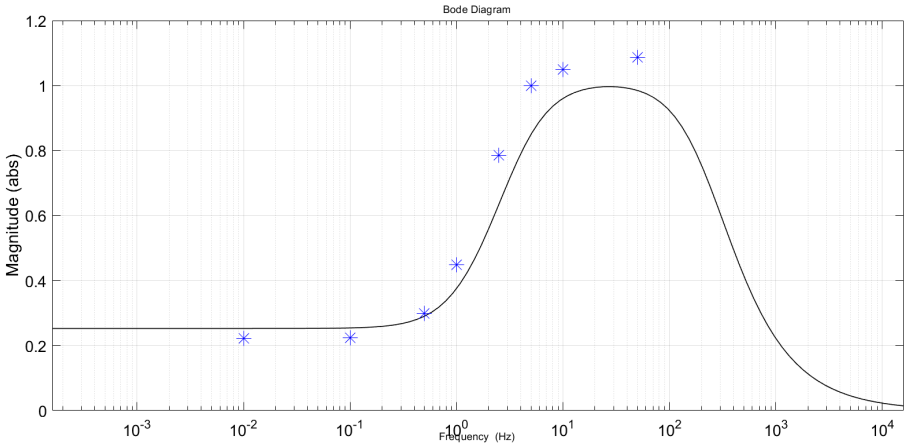

FIGURE 101: Magnitude Diagram of $\frac{\delta i_a^*}{\delta v_a^*}|_{PS}$

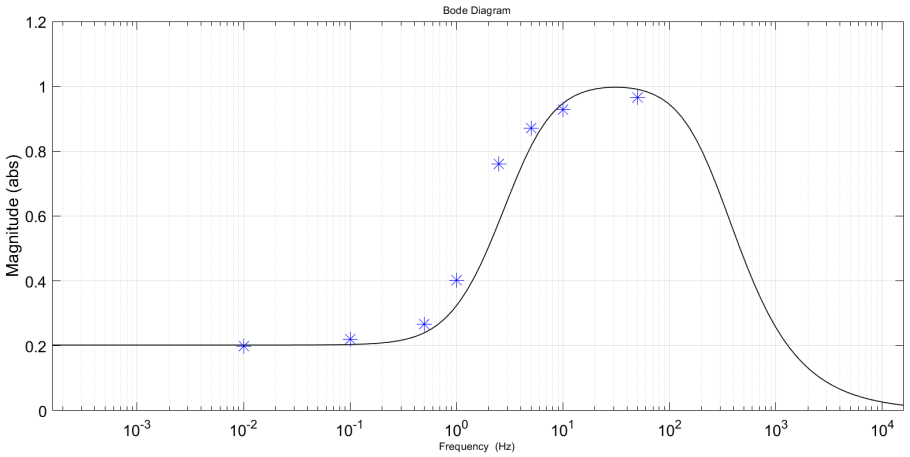

FIGURE 102: Magnitude Diagram of $\frac{\delta i_a^*}{\delta v_a^*}|_{STBD}$

Apparently, compared to the magnitude diagrams in dB, Fig 98 to 102 indicates that the difference in *abs* between simulation and experimental data is more obvious, but the result is still convincing and proves the validity of the linearized model.

Bibliography

[1] Arthur Vrijdag. Potential of hardware-in-the-loop simulation in the towing tank. In *OCEANS 2016 MTS/IEEE Monterey*, pages 1–6. IEEE, 2016.

[2] Douwe Stapersma and Arthur Vrijdag. Linearisation of a ship propulsion system model. *Ocean Engineering*, 142:441–457, 2017.

[3] Tegoeh Tjahjowidodo, Farid Al-Bender, and Hendrik Van Brussel. Friction identification and compensation in a dc motor. *IFAC Proceedings Volumes*, 38(1):554–559, 2005.

[4] H Hanselmann. Hardware-in-the loop simulation as a standard approach for development, customization, and production test of ecu's. Technical report, SAE Technical Paper, 1993.

[5] Rolf Isermann, Jochen Schaffnit, and Stefan Sinsel. Hardware-in-the-loop simulation for the design and testing of engine-control systems. *Control Engineering Practice*, 7(5):643–653, 1999.

[6] M Altosole, A Bagnasco, G Benvenuto, U Campora, M Figari, S D'Arco, M Giuliano, V Giuffra, A Spadoni, S Michetti, et al. Real time simulation of the propulsion plant dynamic behaviour of the aircraft carrier cavour. *Proceedings INEC*, 2008.

[7] M Altosole, G Benvenuto, M Figari, and U Campora. Real-time simulation of a cogag naval ship propulsion system. *Proceedings of the institution of mechanical engineers, part M: journal of engineering for the maritime environment*, 223(1): 47–62, 2009.

[8] Kristin Y Pettersen and Thor I Fossen. Underactuated ship stabilization using integral control: Experimental results with cybership i. In *Proc. 1998 IFAC Symp. Nonlinear Control Systems Design*, pages 127–132, 1998.

[9] Roger Skjetne, Øyvind Smogeli, and Thor I Fossen. Modeling, identification, and adaptive maneuvering of cybership ii: A complete design with experiments. *IFAC Proceedings Volumes*, 37(10):203–208, 2004.

[10] Roger Skjetne, Øyvind N Smogeli, and Thor I Fossen. A nonlinear ship manoeuvering model: Identification and adaptive control with experiments for a model ship. *Modeling, Identification and control*, 25(1):3, 2004.

[11] Nguyen Trong Dong. *Design of hybrid marine control systems for dynamic positioning*. PhD thesis, 2006.

[12] Håkon Nødset Skåtun. Development of a dp system for cs enterprise i with voith schneider thrusters. Master's thesis, Norges teknisk-naturvitenskapelige universitet, Fakultet for ingeniørvitenskap og teknologi, Institutt for marin teknikk, 2011.

[13] Solveig Bjørneset. Modelling and control of thruster assisted position mooring system for a semi-submersible.

[14] Jon Bjørnø. Thruster-assisted position mooring of c/s inocean cat i drillship. Master's thesis, NTNU, 2016.

[15] Stephen D Umans. *Fitzgerald and Kingsley's electric machinery*. McGraw-Hill Higher Education, 2013.

[16] Tolgay Kara and Ilyas Eker. Nonlinear modeling and identification of a dc motor for bidirectional operation with real time experiments. *Energy Conversion and Management*, 45(7-8):1087–1106, 2004.

[17] Mohammed SZ Salah. Parameters identification of a permanent magnet dc motor. *The Islamic University of Gaza*, 94, 2009.

[18] Surajudeen Adewusi. Modeling and parameter identification of a dc motor using constraint optimization technique. *IOSR Journal of Mechanical and Civil Engineering*, 13(6):46–56, 2016.

[19] Mato Fruk, Goran Vujisić, and Tomislav Špoljarić. Parameter identification of transfer functions using matlab. In *Information & Communication Technology Electronics & Microelectronics (MIPRO), 2013 36th International Convention on*, pages 571–576, 2013.

[20] H Klein Woud and D Stapersma. Design of propulsion and electric power generation systems. institute of marine engineering. *Science and Technology. ISBN*, pages 1–902536, 2002.